Inelastic Electron Scattering Spectroscopy: Probing Electromagnetic Surface Mode Resonances of Metallic and Dielectric Interfaces on the Nanoscale

Elliot Karl Beutler

A dissertation
submitted in partial fulfillment of the
requirements for the degree of

Doctor of Philosophy

University of Washington

2022

Reading Committee:

David Masiello, Chair

Brandi Cossairt

Bruce Robinson

Program Authorized to Offer Degree:
Chemistry

University of Washington

Abstract

Inelastic Electron Scattering Spectroscopy: Probing Electromagnetic Surface Mode Resonances of Metallic and Dielectric Interfaces on the Nanoscale

Elliot Karl Beutler

Chair of the Supervisory Committee:
David Masiello
Department of Chemistry

Reliable modeling and tailoring of the optical responses of fabricated dielectric nanostructures is critical to the design and implementation of next generation nano-optical devices, in addition to understanding the mechanisms of charge and energy transfer at atomic scales. Perhaps, no two instruments have been as indispensable in the spectroscopic characterization of atomic scale systems as the laser, and the scanning transmission electron microscope (STEM). Concerning the later, recent advances in electron beam monochromation and aberration correction have allowed for accurately probing target responses from thermal to X-ray energies with high spectral and spatial resolution. The majority of this disseration will focus specifically on electron energy loss (EEL) and gain (EEG) spectroscopies, where spectroscopic measurements are generated by a near-field mediated inelastic scattering process between a series of fast moving electrons and the induced field response of an interrogated target.

In this dissertation, I will restrict the discussion of target excitation to the spectral window of optical-IR energies, as it is at these relatively low energies that electromagnetic surface mode phenomena such as surface plasmon and surface phonon mode resonances occur. At higher energies, stretching from the ultraviolet to x-ray, the inelastic scattering signal is capable of characterizing electronic interband transitions, core electron excitations, and ionization energies.

Intrinsic to this discussion is the role that hybridization plays between ensembles of dielectric particles, and how dielectric nanostructures can couple with a resonant background environment via their induced electromagnetic fields. I then explore how these complex coupling effects are reflected in the EELS/EEGS signals, generated via the inelastic scattering of fast electrons. I attempt to accomplish this by first orienting the reader with classical dielectric theory, and an intuitive characterization of the electromagnetic surface modes intrinsic to dielectric interfaces. I then construct physical models of the spectroscopic observables generated under light excitation and via near-field ion probes. Crucial to all of this, is a robust procedure for mapping the electromagnetic surface modes onto harmonic oscillator coordinates, along with an analysis of the system eigenmodes, and a derivation of their effective masses. This is accomplished by way of the method of Green's functions. This proves to be a powerful and versatile technique for describing the physical and optical properties of the dielectric interfaces which I study herein. My hope is that this intuitive approach to modeling the response of dielectric nanostructures in the presences of light and applied electromagnetic fields, will aid the reader of this dissertation in interpreting spectroscopic measurements in a laboratory setting.

TABLE OF CONTENTS

Page

List of Figures ii

List of Figures iii

Glossary v

Chapter 1: A Short Historical Perspective 2

Chapter 2: Theoretical Foundations 5

- 2.1 Modeling the Dielectric Properties of Matter 5
- 2.2 Classical Models of the Dielectric Function 9
- 2.3 The Electromagnetic Surface Modes of Spherical Particles and Planar Interfaces 15
- 2.4 Deriving Generalized Coordinates and Equations of Motion for Electromagnetic Surface Mode Responses 21

Chapter 3: Modeling the Observables of Far-Field Light and Ion-Scattering Spectroscopies 27

- 3.1 The Aborption, Scattering and Extinction Cross Sections of a Dipolar Surface Mode 27
- 3.2 The Field of a Relativistic Ion, and its Utility as a Spectroscopic Probe . . . 31
- 3.3 A Classical Approach to Modeling Inelastic Ion Scattering 35
- 3.4 A Quantum Approach to Modeling Inelastic Ion Scattering (Energy Loss and Gain) 44

Chapter 4: Coupling between electromagnetic surface modes 56

- 4.1 The Absorption, Scattering and Extinction Cross Sections of Two Electromagnetically Coupled Dipolar Surface Modes 56
- 4.2 The Inelastic Scattering Probability for Two Electromagnetically Coupled Dipoles 63
- 4.3 Coupling Between the Surface Modes of a Slab and a Dipole Mode on a Sphere 71
- 4.4 Nanometer-Scale Spatial and Spectral Mapping of Exciton Polaritons in Structured Plasmonic Cavities 79

Bibliography 86

Appendix A: The Harmonic Oscillator Green's Function 95

Appendix B: The Harmonic Oscillator's Creation and Annihilation Operators 99

Appendix C: Mie Scattering 102

LIST OF FIGURES

Figure Number Page

2.1 A one-dimensional chain of two different types of atoms 9

2.2 (a)Dispersion diagram for a two atom unit cell 11

2.3 (a) A sphere of radius a and (b) a slab of depth d 15

2.4 Schematic representation of the harmonic oscillator degrees of freedom for the surface modes of the sphere and the semi-infinite dielectric slab 21

2.5 Time Domain representation of the surface response functions of a Ag sphere, and an MgO semi-infinite slab 23

3.1 The absorption (red), scattering (blue) and extinction (black) cross sections of a radiating dipole, modeled as a harmonic oscillator. The dipole's natural frequency is $\omega_0 = 1$ eV, its damping rate is $\gamma = 0.2$ eV, and the effective mass is $m = 6 \times 10^{-18}$ gm 27

3.2 (a) Various representations of the electric field of the traveling electron 32

3.3 Schematic of an ion with charge e traveling along direction $\hat{\mathbf{z}}$ external to an Ag-sphere with 10 keV of kinetic energy 36

3.4 Panels (a) and (b) demonstrate the inelastic scattering probability of an Ag-slab with varying depth (i.e. $d = 10 - 50$ nm), and varying kinetic energies (i.e. KE $= 10 - 40$ keV) of the fast ion probe 42

3.5 (a) The thermally assisted scattered loss probability, and (b) the thermally assisted scattered gain probability 52

4.1 Surface plots exploring the evolution of the absorption and scattering cross sections 57

4.2 Examination of the coupling term $g = e^2 \hat{\mathbf{u}}_1 \cdot \boldsymbol{\Lambda}(\mathbf{r}) \cdot \hat{\mathbf{u}}_2$ as a function of unitless kr 59

4.3 Inelastic scattering spectra, and spectrum images of the total loss probability Γ_{EEL} (blue) and and the radiative contribution Γ_{CL} (red) for a pair of Ag spheres 63

4.4 Schematic of the composite sphere-slab dielectric system in the presence of a uniformly moving electron 72

4.5 Comparison of (a) Eq. (4.73) to (b) simulation for the monomers (free space sphere and slab), and the dimer (composite sphere-slab system) 73

4.6 Evolution of Im $\widetilde{\alpha}_y(\omega)$ for an $a = 20$ nm sphere 75
4.7 (a) Analytic LEEG probability spectra and dispersion diagram for a Ag NP array 80
4.8 Spatially and spectrally resolving variations in LPP-EPs using STEM LEEG spectroscopy 84

A.1 Plot of the poles of the spectral representation of the harmonic oscillator Green's function 96

GLOSSARY

HO: Harmonic Oscillator

NP: Nanoparticle

LSP: Localized Surface Plasmon

LSPH: Localized Surface Phonon

SPH: Surface Phonon

EELS: Electron Energy Loss Spectroscopy

EEGS: Electron Energy Gain Spectroscopy

LEEGS: Lattice Electron Energy Gain Spectroscopy

STEM: Scanning Transmission Electron Microscopy

LPP: Lattice Plasmon Polariton

EP: Exciton-Polariton

ACKNOWLEDGMENTS

I'd like to begin by thanking my advisor Professor David Masiello for his support and guidance during my time as a graduate student. Over the course of the last several years as I have encountered a variety of both engrossing and challenging research topics, David has been present both a fantastic guide and teacher, but also as an inspiration. It has been an invaluable experience developing my scientific and mathematical acumen under his tutelage.

To the other members of my committee, Bruce, Brandi, and Gerry, I want to thank you all for your time, patience and interest in my research, along with the invaluable feedback you have provided.

To my family, I'd like to thank you all for your support and words of encouragement over the years. Dad, thank you for your interest and enthusiasm in my work, and for probing me with innumerable questions, both physics and chemistry related. Your own insatiable curiosity about the physical world around us was always inspiring to me, and helped me to think differently. Mom, thank you for always cheering me on and reminding me that I had what it takes to be a scientist.

To Julie, thank you for staying patiently by my side throughout this challenging and exciting time in our lives, as we both followed our dreams. I know it hasn't always been easy being a partner to a graduate student. I look forward to the many happy years together that we have ahead of us and all the adventures and challenges that they have in store.

Additionally, I'd like to thank and acknowledge the current and former members of our research group, many of whom I know consider close friends. You have all been an inspiration to me. I'd specifically like to thank Charles Cherqui, Steve Quillin, Jacob Busche, Kevin Smith and Harrison Goldwyn for their mentorship and patience. The majority of my accomplishments throughout graduate school I owe to all of you and your guidance in probing challenging scientific questions as a lowly chemist trying to find his footing in the field of nano optics and condensed matter physics. I'd also like to thank Claire West, who began her graduate career at the same time as me. It was a wonderful experience coming of age as a researcher along side of you.

To the junior members of our research group, it has been wonderful getting to know you all, and I wish you all great success in your graduate research and beyond, and happiness and fulfillment in your lives with whatever lies ahead of you.

DEDICATION

To all of my family, to Julie, and to our furry companion Juneau

LIST OF PUBLICATIONS

- Bourgeois, Marc R., Elliot K. Beutler, Siamak Khorasani, Nicole Panek, and David J. Masiello. ”Nanometer-Scale Spatial and Spectral Mapping of Exciton Polaritons in Structured Plasmonic Cavities.” *Physical Review Letters* 128, no. 19 (2022): 197401. [1]

- Beutler, Elliot K., Maureen J. Lagos, and David J. Masiello. ”Infrared surface phonon nanospectroscopy of an interacting dielectric-particle–dielectric-substrate dimer using fast electrons.” *Physical Review B* 103, no. 16 (2021): 165418. [2]

- Liu, C., Wu, Y., Hu, Z., Busche, J.A., Elliot K. Beutler, Montoni, N.P., Moore, T.M., Magel, G.A., Camden, J.P., David J. Masiello, and Duscher, G. Continuous wave resonant photon stimulated electron energy-gain and electron energy-loss spectroscopy of individual plasmonic nanoparticles. *ACS Photonics*, 6(10) (2019), pp.2499-2508. [3]

- Bhattacharjee, U., West, C.A., Hosseini Jebeli, S.A., Goldwyn, H.J., Kong, X.T., Hu, Z., Elliot K. Beutler, Chang, W.S., Willets, K.A., Link, S. and David J. Masiello. ”Active far-field control of the thermal near-field via plasmon hybridization.” *ACS Nano*, 13(8) (2019), pp.9655-9663. [4]

In Preparation

- Lee, Ka Yin, Elliot K. Beutler, David Masiello, and Maureen Joel Lagos. ”Substrate Effects on the Phonon Response of Individual Dielectric Nanostructures.” *In preparation* (2022).

- Marc R. Bourgeois, Austin Nixon, Matthieu Chalifour, Elliot K. Beutler, David J. Masiello. “Polarization-resolved electron energy gain nanospectroscopy with vortex beams” *In preparation* (2022).

Chapter 1

A SHORT HISTORICAL PERSPECTIVE

In tandem with Lorentz's force law, Maxwell's equations provide the mathematical foundation for classical electrodynamics, a branch of the physical sciences describing the interaction of electric charges and currents, and the corresponding fields which they source. Upon formulating this system of coupled partial differential equations, James Clerk Maxwell was the first to demonstrate that light itself was in fact an electromagnetic wave [5]. This quickly led to a formal description of light-matter interactions as an extension of classical Newtonian mechanics. Accompanying Newton's theory of gravitation, Maxwell had introduced an additional classical field theory to the arena of contemporary physics, detailing what would later be acknowledged as one of the four fundamental forces which governs all electromagnetic interactions between charge carriers in our observable universe [6].

Prior to the quantum revolution of the early 20th century, Maxwell had supplied an elegant description of electromagnetic phenomena at sufficiently large length scales and field strengths. However, as the sensitivity of instrumentation improved, allowing experimenters to probe electromagnetic phenomena on increasingly small length scales and at very low field intensities, it became apparent that a quantum theory describing the interaction between light and matter was necessary. Pioneering work by Paul Dirac [7], Enrico Fermi [8], Hans Bethe [9], and later Shin'ichirō Tomonaga [10], Julian Schwinger [11, 12], Richard Feynman [13, 14, 15], Freeman Dyson [16, 17] and countless others, led to the the formulation of quantum electrodynamics (QED), the first relativistic quantum field theory.

Broadly speaking, the study of light-matter interactions is categorized under the branch of physical science known as 'optics'. More specifically, when considering interactions over a spacial range comparable to that of the wavelength of an impinging light source we commonly refer to the sub-discipline of 'nano-optics'. It is at this scale where innumerable and interesting features arise when electromagnetic fields interact with nanometer sized objects with varying dielectric properties, tailored to specific applications. Understanding, modelling, fabricating and applying these nanoscopic light-matter interfaces is the focus of the modern and burgeoning field of nano-optics and nano-photonics. The physicists, material scientists, chemists, and engineers working at the forefront of this scientific endeavor must borrow from a diverse array of scientific disciplines and theoretical toolkits to accomplish these tasks.

Fundamental to this venture is the combined effort of theory and experiment, whereby spectroscopic measurements and high resolution spacial imaging techniques verify the predictions of proposed physical models of nanoscale light-matter interactions and aids in determining their relative accuracy. Historically, experimentation has also served to inform theoreticians about the emergence of previously unrecognized physical phenomena [18].

Some of the earliest attempts at spectroscopic measurement date back to Newton [19], who's experiments with crystal prisms demonstrated that a source of white light could be separated into an array of distinct colors. Newton's corpuscular theory gave way to the wave interpretation of light pioneered by Huygens, Young and Fresnel [20], and soon verified by the discoveries of Maxwell. In the interim, experimentalists such as Fraunhofer [21], Balmer [22] and countless others [23, 24, 25] developed increasingly sophisticated methods for separating the emission spectra of light sources, such as the radiant light of the sun, and the incandescent light of heated elements. They observed the presence of bands or spectral lines, which served as a spectral fingerprint for a given material's emissive properties. These finding gave way to theoretical developments by Rydberg [26], Lyman [27] and Paschen [28], and their respective formulas for the observed spectral emission series of the elements. In short order, Bohr's had developed his quantum mechanical model of the atom, relating the emission lines of hydrogen to transitions of the element's lone electron between quantized energy states.

As a theoretical description of light-matter interactions matured throughout the 20th century, spectroscopic techniques followed suit as instrumentalists and engineers developed and refined increasingly sensitive methods of perturbing and measuring the response of matter in the presence of an applied electric or magnetic field. Today, spectroscopists utilize a diverse array of probes, including but not limited to nuclear magnetic resonance spectroscopy, laser spectroscopy, and near-field electron energy loss spectroscopy, to discern atomic structure, probe the density of states of a quantum or classical system, and to study the variety of processes leading to radiative absorption and emission of light by matter. The next several sections of this dissertation will aim to orient the reader with an introduction to modeling the dielectric properties of matter, and how certain spectroscopic observable are modeled, specifically the cases of laser based spectroscopy and inelastic electron scattering (EELS/EEGS).

Chapter 2

THEORETICAL FOUNDATIONS

In this chapter we introduce the reader to the fundamental concepts necessary for understanding the dielectric properties of matter, and how this dielectric description is used to model light-matter interactions at both bulk and microscopic scales. We begin with a classical derivation of the dielectric function with two distinct approaches. Next, using the method of scalar Green's functions, we demonstrate how to solve for the induced scalar fields of dielectric objects in the presences of external charge distributions. Finally we prescribe a method for mapping the induced moments of the dielectric objects onto harmonic oscillator equations of motion, a technique which proves to be exceedingly useful in modeling spectroscopic observables.

2.1 Modeling the Dielectric Properties of Matter

As is customary, we begin with Maxwell's equations, the governing laws of classical electrodynamics

$$\nabla \cdot \mathbf{E} = 4\pi\rho \tag{2.1}$$

$$\nabla \cdot \mathbf{B} = 0 \tag{2.2}$$

$$\nabla \times \mathbf{E} = -\frac{1}{c}\dot{\mathbf{B}}(\mathbf{x}, t) \tag{2.3}$$

$$\nabla \times \mathbf{B} = \frac{1}{c}\dot{\mathbf{E}} + \frac{4\pi}{c}\mathbf{J} \tag{2.4}$$

where ρ and $\mathbf{J}$ are the respective charge and current densities which source the electric and magnetic fields. The fields may be sourced by both free charges (f) due to a source of ions, and bound charges (b) resulting from the polarization of a material in the presence of an external field.

$$\rho = \rho_f + \rho_b \tag{2.5}$$

$$\mathbf{J} = \mathbf{J}_f + \mathbf{J}_b \tag{2.6}$$

The free charge and current density may always be expressed in terms of a sum of point charges as

$$\rho_f = \sum_j q_j \delta(\mathbf{x} - \mathbf{x}_j) \tag{2.7}$$

$$\mathbf{J}_f = \rho_f \mathbf{v}_{\mathrm{d}} \tag{2.8}$$

Where $\mathbf{v}_{\mathrm{d}}$ represents the average drift velocity of the free charges. We then introduce the polarization density $\mathbf{P}$ as a vector field sourced by a system's bound charges as

$$-\nabla \cdot \mathbf{P} = \rho_b. \tag{2.9}$$

Appealing to the continuity equation to relate the current density of the bound charges to the polarization density field

$$\begin{aligned} \nabla \cdot \mathbf{J}_b &= -\frac{\partial \rho_b}{\partial t} \\ &= \nabla \cdot \frac{\partial \mathbf{P}}{\partial t} \end{aligned} \tag{2.10}$$

Therefore, when a material's magnetic polarization is negligible, we write

$$\mathbf{J}_b = \frac{\partial \mathbf{P}}{\partial t} \tag{2.11}$$

Because $\mathbf{J} = \mathbf{J}_f + \mathbf{J}_b$, using Eqn. (2.11), we find Ampere's law may be expressed as

$$\nabla \times \mathbf{B} = \frac{1}{c}\dot{\mathbf{D}} + \frac{4\pi}{c}\mathbf{J}_f, \tag{2.12}$$

and for Gauss's law (2.1)

$$\nabla \cdot \mathbf{D} = 4\pi\rho_f. \tag{2.13}$$

We have derived the *macroscopic* Maxwell Equations in the presence of polarizable material, to which we will now label

$$\nabla \cdot \mathbf{D} = 4\pi\rho_f \quad \text{(Gauss's law)} \tag{2.14}$$

$$\nabla \cdot \mathbf{B} = 0 \quad \text{(No magnetic monopole law)} \tag{2.15}$$

$$\nabla \times \mathbf{E} = -\frac{1}{c}\dot{\mathbf{B}}(\mathbf{x}, t) \quad \text{(Faraday's law of induction)} \tag{2.16}$$

$$\nabla \times \mathbf{B} = \frac{1}{c}\dot{\mathbf{D}} + \frac{4\pi}{c}\mathbf{J}_f \quad \text{(Ampère's law)} \tag{2.17}$$

Above, the displacement field has been introduced, and it is defined in terms of the electric and polarization field as

$$\mathbf{D} = \mathbf{E} + 4\pi\mathbf{P}. \tag{2.18}$$

Eqn (2.18) is referred to as the constitutive relation of the electric field. We relate the polarization field to the electric field strength by way of the electric susceptibility χ, as $\mathbf{P} = \chi\mathbf{E}$. For fields which may vary both in time and space, we define this relationship between the vector fields in terms of a spatiotemporal convolution integral, where the susceptibility inherits the role of a causal response function. When the magnitude of the field is sufficiently weak, the causal response may be approximated as linear. Therefore

$$\mathbf{P}(\mathbf{x},t) = \int d\mathbf{x}'dt'\chi(\mathbf{x}-\mathbf{x}';t-t')\mathbf{E}(\mathbf{x}',t'), \tag{2.19}$$

Where the coordinates $\mathbf{x}'$ and t', represent the location of an impulse introduced by the electric field in space and time. Considering the Fourier transform of the polarization field

$$\begin{aligned}\mathbf{P}(\mathbf{k},\omega) &= \int d\mathbf{x}dt\ \mathbf{P}(\mathbf{x},t)e^{-i(\mathbf{k}\cdot\mathbf{x}-\omega t)} \\ &= \int d\mathbf{x}dt\left[\int d\mathbf{x}'dt'\chi(\mathbf{x}-\mathbf{x}';t-t')\mathbf{E}(\mathbf{x}',t')\right]e^{-i(\mathbf{k}\cdot\mathbf{x}-\omega t)} \\ &= \chi(\mathbf{k},\omega)\mathbf{E}(\mathbf{k},\omega)\end{aligned} \tag{2.20}$$

In the final line of Eqn. (2.20), we have applied the convolution theorem to evaluate the integrals. Therefore, the Fourier transform of the displacement field evaluates to

$$\begin{aligned}\mathbf{D}(\mathbf{k},\omega) &= (1+4\pi\chi(\mathbf{k},\omega))\mathbf{E}(\mathbf{k},\omega) \\ &= \varepsilon(\mathbf{k},\omega)\mathbf{E}(\mathbf{k},\omega).\end{aligned} \tag{2.21}$$

In Eqn. (2.21), we have defined a non-local, dispersive dielectric function ε, which encodes the dynamic response of a bulk material's bound charges to an applied electric field. In a 'local' approximation of the dielectric function or in the long wavelength limit (i.e. $k = 0$), the response of the dielectric material is spatially independent, and we may easily transform back into direct space, relating the electric and displacement fields via a frequency dependent dielectric function as

$$\mathbf{D}(\mathbf{x},\omega) = \varepsilon(\omega)\mathbf{E}(\mathbf{x},\omega), \tag{2.22}$$

where now, the dispersive properties of the material are only dependent on the frequency of the applied electric field.

2.2 *Classical Models of the Dielectric Function*

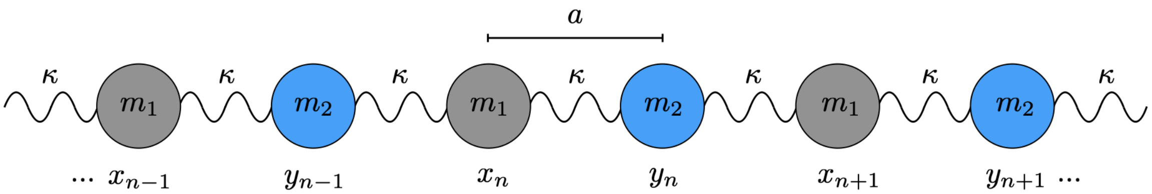

Figure 2.1: A one-dimensional chain of two different types of atoms, with masses m_1 and m_2, which alternate along the length of the chain. The atoms are bound by a force constant κ, and each atom pair occupies a unit cell of length a. The relative position of each atom x_N, y_N is indicated by its subscript.

A simple model [29, 30] which aids in developing intuition about the optical properties of a solid is that of the one-dimensional two-atom chain. We assume the chain extends far enough in each direction that its length can be safely modeled as infinite, avoiding the introduction of boundary conditions. Considering only nearest neighbor interactions, and ignoring interactions between electrons and dissipation effects, we may immediately write down the equations of motion for two neighboring atoms which comprise a single unit cell, at positions x_n and y_n

$$m_1\ddot{x}_n = -\kappa(x_n - y_{n-1}) - \kappa(x_n - y_n) \tag{2.23}$$

$$m_2\ddot{y}_n = -\kappa(y_n - x_{n+1}) - \kappa(y_n - x_n). \tag{2.24}$$

The solutions are taken to be waves of the form

$$x_n(t) = x_k e^{i(kna-\omega t)} \tag{2.25}$$

$$y_n(t) = y_k e^{i(kna-\omega t)} \tag{2.26}$$

Where k is the oscillation wavenumber. Substituted into (2.24), we may recast the coupled equations of motion into matrix form as

$$\begin{pmatrix} 2\kappa - m_1\omega^2 & -\kappa[1+e^{-ika}] \\ -\kappa[1+e^{ika}] & 2\kappa - m_2\omega^2 \end{pmatrix} \begin{pmatrix} x_k \\ y_k \end{pmatrix} = \begin{pmatrix} 0 \\ 0 \end{pmatrix} \tag{2.27}$$

The nontrivial solutions for matrix equations of the type $\bar{\mathbf{A}}\mathbf{x} = \mathbf{0}$, are found by setting the determinant of the matrix equal to zero, as $\det|\bar{\mathbf{A}}| = 0$. Solving for ω, we find a set of four solutions, two of which are negative and discarded. The two remaining positive valued eigenfrequencies are

$$\omega_{\pm}(k) = \left[\frac{\kappa}{\mu}\left(1 \pm \left[1 - \frac{2\mu}{m_1+m_2}(1-\cos ka)\right]\right)^{\frac{1}{2}}\right]^{\frac{1}{2}}, \tag{2.28}$$

where $\mu = m_1 m_2/(m_1+m_2)$ is the reduced mass of the unit cell. Plotting the eigenfrequencies as a function of wavenumber k, we observe the emergence of two branches in the resulting dispersion plot which repeat over the first Brillouin zone. The upper branch is commonly referred to as the optical branch, and the frequencies $\omega_+(k)$ correspond to eigenfrequencies of the optically active normal modes, as we will demonstrate in this section. The eigenfrequencies of the lower branch $\omega_-(k)$ are referred to as the acoustic modes. In the long wavelength limit, the wavenumber $k = 0$, and the resulting normal mode frequencies are $\omega_+(0) = \sqrt{2\kappa/\mu}$ and $\omega_-(0) = 0$. Substituted into (2.27), we solve for the long wavelength

Fourier amplitudes of the oscillators

$$x_0 = -\frac{m_2}{m_1} y_0 \ ; \quad \text{if} \quad \omega_+(0) = \omega \tag{2.29}$$

$$x_0 = y_0 \ ; \quad \text{if} \quad \omega_-(0) = \omega \tag{2.30}$$

And we observe that the oscillation amplitudes of x_0 and y_0 within the unit cell are of opposite in sign, and scaled with respect to the ratio of the their masses, indicating that they oscillate out-of-phase with one another. As for the acoustic branch, the amplitudes of oscillation are exactly equal in magnitude, indicating an in-phase oscillation of the atoms. We now introduce an external driving force in the form of a time oscillating electric field acting uniformly on the oscillators in the long wavelength limit. The time dependent force of the

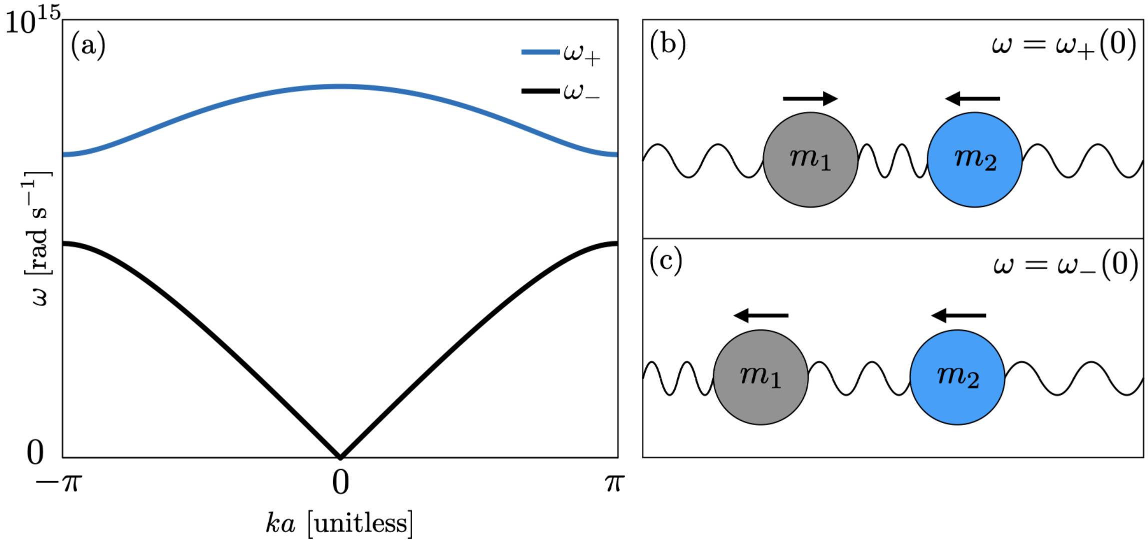

Figure 2.2: (a)Dispersion diagram for a two atom unit cell with mass ratio $m_1/m_2 = 2$ over the first Brillouin zone, where ω_+ represent the optical modes, and ω_- the acoustic modes. (b) Out-of-phase oscillation of the optical mode, and (c) in-phase oscillation of the acoustic modes in the long wavelength limit ($k = 0$).

external field at the unit cell position is $F(t) = eE(t)$. Under a steady-state approximation

$$x_n(t) = x_0(\omega)e^{-i\omega t} \tag{2.31}$$

$$y_n(t) = y_0(\omega)e^{-i\omega t} \tag{2.32}$$

$$E(t) = E(\omega)e^{-i\omega t} \tag{2.33}$$

Solving for x_0 and y_0 in the long wavelength limit, we find

$$x_0(\omega) = \frac{e}{m_1}\frac{E_0(\omega)}{\omega_0^2 - \omega^2} \tag{2.34}$$

$$y_0(\omega) = -\frac{e}{m_2}\frac{E(\omega)}{\omega_0^2 - \omega^2} \tag{2.35}$$

Where above, where have relabeled the long wavelength optical mode frequency $\omega_+(0) = \omega_0$. Perturbing the oscillating atoms from their equilibrium positions results in an induced charge distribution, which can be well approximate as dipolar in character. The resulting dipole is proportional to the net amplitude of displacement between the two atoms, and is defined as $p = -e(x_0 - y_0)$. By observation, we notice that only the optical mode amplitudes for the oscillators produce a non-zero dipole moment, demonstrating that the acoustic modes do not directly couple to an applied electric field. Working in the frequency domain, the polarization field [31] is defined as

$$\begin{aligned} P(\omega) &= Np(\omega) \\ &= \frac{Ne^2}{\mu}\frac{E(\omega)}{\omega_0^2 - \omega^2} \qquad (2.36) \\ &= \chi(\omega)E(\omega), \end{aligned}$$

Where N is the dipole number per unit volume. Now, by observation, the electric susceptibility is

$$\chi(\omega) = \frac{Ne^2}{\mu}\frac{1}{\omega_0^2 - \omega^2}. \tag{2.37}$$

Recalling the constitutive relation (2.18), we may immediately write down the dielectric function of the one dimensional, diatomic crystal, and defining the material's plasma frequency as $\omega_p = \sqrt{4\pi Ne^2/\mu}$

$$\varepsilon_L(\omega) = 1 + \frac{\omega_p^2}{\omega_0^2 - \omega^2} \tag{2.38}$$

Eqn (2.38) is commonly referred to as the Lorentz oscillator model of the dielectric function, which can be broadly applied to model the optical response of a material's charge carriers bound by a central potential. Such optically active responses may include phonons, excitons, and a variety of electronic excitations of a material's bound core and valence electrons, all of which are effectively modeled using a Lorentz oscillator response function. An alternative derivation of the Lorentz oscillator model may begin with considering a unit cell consisting of a single atom, and a harmonically bound electron. As before, we may write down an equation of motion for the electron under the influence of a time oscillating electric field. We ignore the motion of the much heavier nuclei to which the electron is bound, and coupling to the field of all other surrounding electrons, we arrive at

$$\ddot{\mathbf{x}}_{\mathrm{el}} + \gamma\dot{\mathbf{x}}_{\mathrm{el}} + \omega_0^2\mathbf{x}_{\mathrm{el}} = \frac{e}{m}\mathbf{E}(t) \tag{2.39}$$

In Eqn (2.39), $\mathbf{x}_{\mathrm{el}}$ represents the displacement of the electron from its equilibrium position, ω_0 is the natural oscillation frequency, $m\gamma\dot{\mathbf{x}}_{\mathrm{el}}$ represents an unspecified force due to dissipation preventing the oscillations from continuing indefinitely, and $m \approx m_{\mathrm{el}}$ is the reduced mass of the electron-nucleus system. Again, assuming steady-state solutions of the form $\mathbf{x}_{\mathrm{el}}(t) = \mathbf{x}_{\mathrm{el}}(\omega)e^{-i\omega t}$, $\mathbf{E}(t) = \mathbf{E}(\omega)e^{-i\omega t}$, we immediately produce a solution for the Fourier amplitude of the electron's oscillation.

$$\mathbf{x}_{\mathrm{el}}(\omega) = \frac{e}{m}\frac{\mathbf{E}(\omega)}{\omega_0^2 - \omega^2 - i\gamma\omega} \tag{2.40}$$

The resulting dipole moment is defined as $\mathbf{p}(\omega) = e\mathbf{x}_{\text{el}}(\omega)$, and as before, we recall the constitutive relations to derive the dielectric function, now including the effects of dissipation

$$\varepsilon_L(\omega) = 1 + \frac{\omega_p^2}{\omega_0^2 - \omega^2 - i\gamma\omega}. \tag{2.41}$$

In general a particular material may host an ensemble of optically active excitations, due to a variety of electrons which experience a unique binding potential to the nuclei. Therefore, in general we may write

$$\varepsilon_L(\omega) = 1 + \omega_p^2 \sum_i \frac{f_i}{\omega_i^2 - \omega^2 - i\gamma_i\omega}, \tag{2.42}$$

Where f_i is a unitless parameter, representing the oscillator strength of a particular resonance in a material. Formally, we define the oscillator strength as $f_i = N_i/N_{\text{tot}}$, where N_i is the charge carrier number density, and N_{tot} is the total charge carrier number density. Then, we define $\omega_p^2 = 4\pi N_{\text{tot}} e^2/m$. There are classes of materials which at ambient temperatures possess an ensemble of electrons which are unbound to a particular nucleus. Considering these electrons 'free' (i.e. $\omega_0 = 0$, as they experience no restoring force or binding potential), the corresponding equation of motion under the influence of an external, time dependent field is

$$\ddot{\mathbf{x}}_{\text{el}} + \gamma\dot{\mathbf{x}}_{\text{el}} = \frac{e}{m}\mathbf{E}(t). \tag{2.43}$$

In a procedure identical to that of the bound charge carriers, we quickly arrive at the following expression for the so call 'Drude' dielectric model, which encodes the material's optical response due to the presence of a free electron gas. We write

$$\varepsilon_D(\omega) = 1 - \frac{\omega_p^2}{\omega^2 + i\gamma\omega}. \tag{2.44}$$

The Drude dielectric function is typically used to model the optical responses of metals and other special classes of materials which possess conductive properties in the presence of an applied electric field or voltage potential, at ambient temperatures. In sum, the contribution of both a free electron gas and a collection of harmonically bound charges can contribute to the optical properties of a material, and that material's dielectric function can be effectively modeled by a composite 'Drude-Lorentz' dielectric model

$$\begin{aligned}\varepsilon(\omega) &= \varepsilon_D(\omega) + \varepsilon_L(\omega) \\ &= \varepsilon_\infty - \frac{\omega_p^2}{\omega^2 + i\gamma\omega} + \omega_p^2 \sum_i \frac{f_i}{\omega_i^2 - \omega^2 - i\gamma_i\omega}\end{aligned} \tag{2.45}$$

Where ε_∞ is included to model the contribution of a static, real valued response of a material, which is greater than or equal to unity.

2.3 The Electromagnetic Surface Modes of Spherical Particles and Planar Interfaces

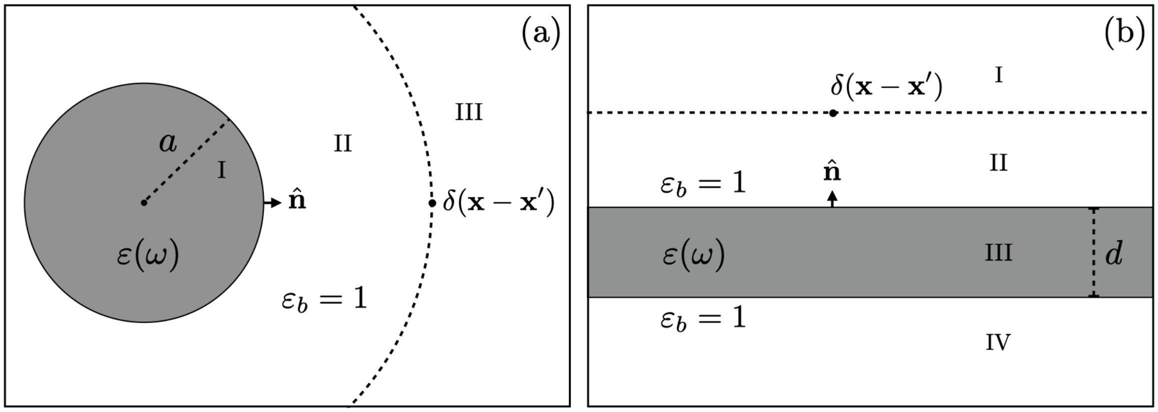

Figure 2.3: (a) A sphere of radius a and (b) a slab of depth d which extends infinitely along its lateral directions, perpendicular to the unit vector $\hat{\mathbf{n}}$. Both objects are described by a dielectric function $\varepsilon(\omega)$, in the presence of an external source, represented by a delta function.

Considering Eqn (2.22), and writing down the electric field in terms of the electric scalar potential Φ and the magnetic vector potential $\mathbf{A}$

$$\mathbf{E}(\mathbf{x},\omega) = -\nabla\Phi(\mathbf{x},\omega) - \frac{1}{c}\frac{\partial \mathbf{A}(\mathbf{x},\omega)}{\partial t} \tag{2.46}$$

Where the potential fields are defined up to a gauge degree of freedom, represented by the function $\mathcal{G}$, as

$$\Phi \rightarrow \Phi - \frac{1}{c}\frac{\partial \mathcal{G}}{\partial t} \tag{2.47}$$

$$\mathbf{A} \rightarrow \mathbf{A} + \nabla \mathcal{G}. \tag{2.48}$$

The presence of $\mathcal{G}$ leaves the fields and Maxwell's equations unchanged. In this section we will work under a 'quasistatic' approximation, where we consider the speed of light to be infinite. In this regime our expression for the displacement field simplifies to

$$\mathbf{D}(\mathbf{x}, \omega) = -\varepsilon(\omega)\nabla\Phi(\mathbf{x}, \omega) \tag{2.49}$$

To solve for the potential Φ in Eqn. (2.49), we employ the method of Green's functions [31, 32, 33]. In the regions of space where there is free charge, we replace the charge density in Gauss's law with an infinitesimal impulse in the form of a delta function. In the presence of a source, and under a quasistatic approximation, Gauss's law assumes the form of Poisson's equation, the inhomogeneous form of Laplace's equation. In general, Laplace's equation may be solved analytically in any curvlinear coordinate system where the equation is fully separable. The choice of what coordinate system to work in is typically dictated by the geometry of the object which harbors the system's bound charges. This drastically simplifies solving the resulting boundary value problem. Here, we will restrict ourselves to finding a solution for the particular case of first a sphere, and then a slab of varying depth and infinite lateral extent. Starting with the sphere in the presence of a source external to the dielectric material, we introduce a Green's function as a solution to the following equations

$$\begin{aligned} r > a: &\quad -\nabla^2 G(\mathbf{x}, \mathbf{x}'; \omega) = 4\pi\delta(\mathbf{x} - \mathbf{x}') \\ r < a: &\quad -\varepsilon(\omega)\nabla^2 G(\mathbf{x}, \mathbf{x}'; \omega) = 0, \end{aligned} \tag{2.50}$$

where $\mathbf{x}$ and $\mathbf{x}'$ represent an arbitrary observation point and the position of the source, respectively. Defining three spatial regions indicated by labels I, II, III, where due to the absence of free charge, the potential will satisfy Laplace's equation.

$$-\nabla^2\Phi(\mathbf{x},\omega) = 0 \tag{2.51}$$

A general solution to (2.51) in spherical coordinates is well known in term of the solid harmonic functions as

$$\Phi(\mathbf{x},\omega) = \sum_{\ell m}\left(A_{\ell m}(\omega)r^{\ell} + B_{\ell m}(\omega)r^{-(\ell+1)}\right)Y_{\ell m}(\theta,\phi). \tag{2.52}$$

Above, $Y_{\ell m}(\theta,\phi)$ are the spherical harmonic functions, while $A_{\ell m}$ and $B_{\ell m}$ are to-be-determined expansion coefficients, and r is the radial coordinate. For regions I,II, and III, using (2.52), we then enforce the physical constraints that the potential must trend towards zero at infinite distances, and must remain finite at the center of the sphere. Therefore, we infer the form of the Green's function in regions I-III as

$$\begin{aligned} G_{\mathrm{I}}(\mathbf{x},\mathbf{x}';\omega) &= \sum_{\ell m} A_{\ell m}(\mathbf{x},\omega)r^{\ell}Y_{\ell m}(\theta,\phi) \\ G_{\mathrm{II}}(\mathbf{x},\mathbf{x}';\omega) &= \sum_{\ell m}\left(B_{\ell m}(\mathbf{x},\omega)r^{\ell} + C_{\ell m}(\mathbf{x},\omega)r^{-(\ell+1)}\right)Y_{\ell m}(\theta,\phi) \\ G_{\mathrm{III}}(\mathbf{x},\mathbf{x}';\omega) &= \sum_{\ell m} D_{\ell m}(\mathbf{x},\omega)r^{-(\ell+1)}Y_{\ell m}(\theta,\phi). \end{aligned} \tag{2.53}$$

Next, recalling the completeness relation of the spherical harmonic functions

$$\frac{1}{\sin\theta}\delta(\theta-\theta')\delta(\phi-\phi') = \sum_{\ell m} Y_{\ell m}(\theta,\phi)Y^{*}_{\ell m}(\theta',\phi'), \tag{2.54}$$

we enforce the boundary conditions, that in the absence of free charge

$$\hat{\mathbf{n}} \cdot (\mathbf{D}_{\mathrm{I}} - \mathbf{D}_{\mathrm{II}}) = 0, \tag{2.55}$$

and in the presence of free charge

$$\hat{\mathbf{n}} \cdot (\mathbf{D}_{\mathrm{II}} - \mathbf{D}_{\mathrm{III}}) = 4\pi\sigma, \tag{2.56}$$

and that everywhere, G is a continuous and well behaved function. In spherical coordinates, the surface density due to a spatially infinitesimal impulse is $\sigma = (r^2 \sin\theta)^{-1}\delta(\theta-\theta')\delta(\phi-\phi')$. Finally, we solve for the scalar Green's function both within and external to the sphere

$$\begin{aligned}
r > a : \quad & G_{\mathrm{II,III}}(\mathbf{x}, \mathbf{x}'; \omega) = \frac{1}{|\mathbf{x} - \mathbf{x}'|} - \sum_{\ell m} \frac{4\pi}{2\ell+1} \frac{a^{2\ell+1}}{r^{\ell+1} r'^{\ell+1}} Y_{\ell m}(\theta, \phi) Y^*_{\ell m}(\theta', \phi') \beta_{\ell m}(\omega) \\
r < a : \quad & G_{\mathrm{I}}(\mathbf{x}, \mathbf{x}'; \omega) = 4\pi \sum_{\ell m} \frac{r^\ell}{r'^{\ell+1}} Y_{\ell m}(\theta, \phi) Y^*_{\ell m}(\theta', \phi') \eta_{\ell m}(\omega)
\end{aligned} \tag{2.57}$$

In the region $r > a$ which includes contributions to the net potential from both the free source and bound charge response, we recover both the Green's function solution to Poisson's equation, and the 'induced' Green's function. The unitless response functions β_ℓ and η_ℓ depend on the sphere's dielectric function as

$$\beta_{\ell m}(\omega) = \frac{\ell(\varepsilon(\omega) - 1)}{\ell(\varepsilon(\omega) + 1) + 1} \tag{2.58}$$

$$\eta_{\ell m}(\omega) = \frac{1}{\ell(\varepsilon(\omega) + 1) + 1}. \tag{2.59}$$

In the case of the dielectric slab with an external source, it is easiest to work in a cylindrical coordinate system to solve the associated boundary value problem. As is indicated in figure (2.3) there are four spacial regions to consider. For simplicity, we define the upper surface of the slab to live at $z = 0$. The potential will again satisfy Laplace's equation (2.51) in these four spatial regions. A general solution to Laplace's equation in cylindrical coordinates is

$$\Phi(\mathbf{x}, \omega) = \sum_{n=-\infty}^{\infty} e^{in\phi} \int_0^\infty dk J_n(k\varrho) e^{\pm kz}, \tag{2.60}$$

when the unit vector normal to the slab's surface is directed along coordinate z. The terms $J_n(k\varrho)$ are the cylindrical Bessel function of the first kind. We define the radial coordinate as $\varrho = \sqrt{x^2 + y^2}$, and k is a continuously indexing wavenumber. Again, imposing physical constraints on the values of the potential at $z = 0, d$ and $z = \pm\infty$, the Green's function in regions I-IV are

$$\begin{aligned}
G_{\mathrm{I}}(\mathbf{x}, \mathbf{x}'; \omega) &= \sum_{n=-\infty}^{\infty} e^{in\phi} \int_0^\infty dk J_n(k\varrho) A_{kn}(\mathbf{x},' \omega) e^{-kz} \\
G_{\mathrm{II}}(\mathbf{x}, \mathbf{x}'; \omega) &= \sum_{n=-\infty}^{\infty} e^{in\phi} \int_0^\infty dk J_n(k\varrho) \left(B_{kn}(\mathbf{x}', \omega) e^{kz} + C_{kn}(\mathbf{x}', \omega) e^{-kz} \right) \\
G_{\mathrm{III}}(\mathbf{x}, \mathbf{x}'; \omega) &= \sum_{n=-\infty}^{\infty} e^{in\phi} \int_0^\infty dk J_n(k\varrho) \left(D_{kn}(\mathbf{x}', \omega) e^{kz} + E_{kn}(\mathbf{x}', \omega) e^{-kz} \right) \\
G_{\mathrm{IV}}(\mathbf{x}, \mathbf{x}'; \omega) &= \sum_{n=-\infty}^{\infty} e^{in\phi} \int_0^\infty dk J_n(k\varrho) F_{kn}(\mathbf{x}', \omega) e^{kz}
\end{aligned} \tag{2.61}$$

Applying the boundary conditions (2.55),(2.56), defining the surface density $\sigma = \varrho^{-1}\delta(\varrho - \varrho')\delta(\phi - \phi')$, and recalling the completeness relation of the cylindrical functions

$$\frac{1}{\varrho}\delta(\varrho - \varrho')\delta(\phi - \phi') = \frac{1}{2\pi} \sum_{n=-\infty}^{\infty} e^{in(\phi-\phi')} \int_0^\infty dk\; k J_n(k\varrho) J_n(k\varrho'), \tag{2.62}$$

we solve for the Green's function in the region of the source (I,II) [2, 34]

$$G_{\mathrm{I,II}}(\mathbf{x}, \mathbf{x}'; \omega) = \frac{1}{|\mathbf{x} - \mathbf{x}'|} - \sum_{n=-\infty}^{\infty} e^{in(\phi-\phi')} \int_0^\infty dk J_n(k\varrho) J_n(k\varrho') e^{-k(z+z')} \zeta_{\mathrm{I,II}}(k, \omega) \tag{2.63}$$

Within the slab (III)

$$G_{\mathrm{III}}(\mathbf{x},\mathbf{x}';\omega) = 2\sum_{n=-\infty}^{\infty} e^{in(\phi-\phi')}\int_0^\infty dk J_n(k\varrho)J_n(k\varrho')e^{-k(z+z')}\zeta_{\mathrm{III}}(k,\omega) \tag{2.64}$$

And below the slab (IV)

$$G_{\mathrm{III}}(\mathbf{x},\mathbf{x}';\omega) = 4\sum_{n=-\infty}^{\infty} e^{in(\phi-\phi')}\int_0^\infty dk J_n(k\varrho)J_n(k\varrho')e^{-k(z+z')}\zeta_{\mathrm{IV}}(k,\omega). \tag{2.65}$$

Again, in the region $z > 0$, we recover the Green's function solution for Poisson's equation, and the 'induced' Green's function due to the response of the bound charges on the slab. The response functions are

$$\zeta_{\mathrm{I,II}}(k,\omega) = \frac{(\varepsilon(\omega)-1)(1-e^{-2kd})}{(\varepsilon(\omega)+1)^2-(\varepsilon(\omega)-1)^2e^{-2kd}} \tag{2.66}$$

$$\zeta_{\mathrm{III}}(k,\omega) = \frac{(\varepsilon(\omega)-1)e^{-2kd}+(\varepsilon(\omega)+1)}{(\varepsilon(\omega)+1)^2-(\varepsilon(\omega)-1)^2e^{-2kd}} \tag{2.67}$$

$$\zeta_{\mathrm{IV}}(k,\omega) = \frac{\varepsilon(\omega)}{(\varepsilon(\omega)+1)^2-(\varepsilon(\omega)-1)^2e^{-2kd}} \tag{2.68}$$

For both the sphere and slab, we observe that the surface resonance conditions are determined by the pole structure of Eqns. (2.58) and (2.66). It is then apparent that the sphere hosts an infinite number of discreet surface resonances, indexed by integer value ℓ, while the slab simultaneously hosts a pair of surface resonances that evolve continuously with the product of the slab depth and the wavenumber kd. In the particular case where the depth of the slab $d \to \infty$, the response function in each region of space surrenders its dependence on the indexing wavenumber k. Particularly in region I, the response function simplifies to $\zeta_{\mathrm{I,II}}(\omega) = -(\varepsilon(\omega)-1)/(\varepsilon(\omega)+1)$, and we recover the well known response function for the 'semi-infinite' half-space. Having derived the Green's function for the sphere and the slab, determining the electric potential is now a matter of integrating the Green's function against an arbitrary source or charge distribution. To understand this general property of the Green's function, we consider the trivial solution to the potential

$$4\pi\rho(\mathbf{x},\omega) = 4\pi \int d\mathbf{x}' \; \rho(\mathbf{x}',\omega)\delta(\mathbf{x}-\mathbf{x}'). \tag{2.69}$$

Using Eqn. (2.50), we find

$$4\pi\rho(\mathbf{x},\omega) = \nabla^2 \int d\mathbf{x}' \; \rho(\mathbf{x}',\omega) \; G(\mathbf{x}-\mathbf{x}'). \tag{2.70}$$

Finally by observation, we solve for the potential in terms of its associated Green's function

$$\Phi(\mathbf{x},\omega) = \int d\mathbf{x}' G(\mathbf{x},\mathbf{x}';\omega)\rho(\mathbf{x}',\omega). \tag{2.71}$$

Here, we see that the potential is the convolution of the charge density against the causal Green's function, which encodes the material's dynamic response.

2.4 Deriving Generalized Coordinates and Equations of Motion for Electromagnetic Surface Mode Responses

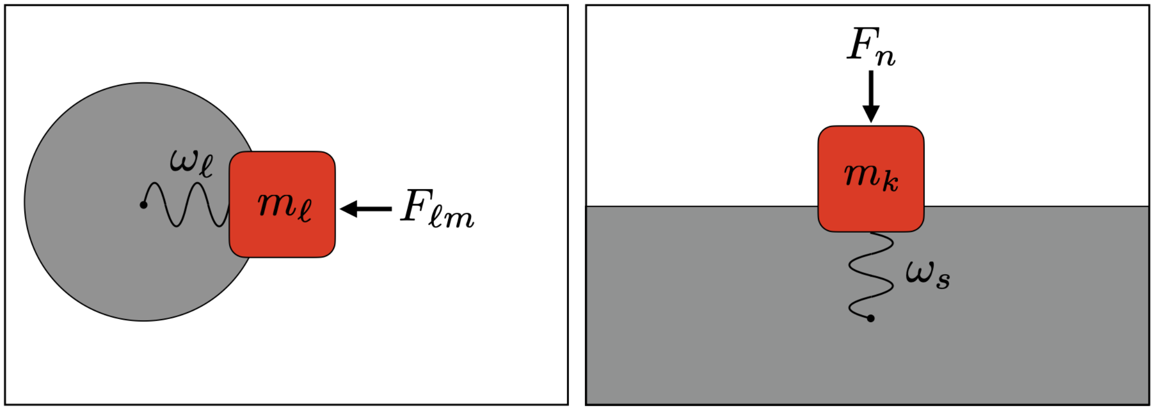

Figure 2.4: Schematic representation of the harmonic oscillator degrees of freedom for the surface modes of the sphere and the semi-infinite dielectric slab. Each ℓ-dependent surface mode of the sphere possess a unique effective mass m_ℓ and natural frequency ω_ℓ, and a wavenumber dependent effective mass m_k and natural frequency ω_s for the semi-infinite slab. These parameters define the dynamics of a generalized coordinate of the surface modes for the sphere and slab, which are acted on by external forces $F_{\ell m}$ and F_n, defined by the form of the external charge distribution, and system's mode functions, $f_{\ell m}$ and Λ_n.

Considering the time domain representation of the surface response functions permits a definition for the dynamic induced potentials of the sphere Φ_{sph} and the slab Φ_{slab}, as a product of a time-dependent amplitude and space-dependent mode function decomposition [35]. We consider the induced Green's function in the regions $r > a$, and $z > 0$ for the sphere and slab, respectively, and define

$$\begin{aligned}\Phi_{\text{sph}}(\mathbf{x},t) &= \int d\mathbf{x}'dt'G_{\text{sph}}(\mathbf{x},\mathbf{x}';t-t')\rho(\mathbf{x}',t') \\ &= \sum_{\ell m} f_{\ell m}(\mathbf{x})u_{\ell m}(t)\end{aligned} \tag{2.72}$$

$$\begin{aligned}\Phi_{\text{slab}}(\mathbf{x},t) &= \int d\mathbf{x}'dt'G_{\text{slab}}(\mathbf{x},\mathbf{x}';t-t')\rho(\mathbf{x}',t') \\ &= \sum_{n=-\infty}^{\infty}\int_0^\infty dk\Lambda_n(k,\mathbf{x})Q_n(k,t)\end{aligned} \tag{2.73}$$

We define the mode functions as

$$f_{\ell m}(\mathbf{x}) = -e\sqrt{\frac{4\pi}{2\ell+1}}\frac{a^{\ell-1}}{r^{\ell+1}}Y_{\ell m}(\theta,\phi) \tag{2.74}$$

$$\Lambda_n(k,\mathbf{x}) = -ek^2e^{in\phi}J_n(k\varrho)e^{-kz} \tag{2.75}$$

And the time dependent coordinates as

$$u_{\ell m}(t) = -\frac{a^3}{e^2}\int d\mathbf{x}'dt'f^*_{\ell m}(\mathbf{x}')\rho(\mathbf{x}',t')\beta_{\ell m}(t-t') \tag{2.76}$$

$$Q_n(k,t) = -\frac{1}{(ek^2)^2}\int d\mathbf{x}'dt'\Lambda^*_n(k,\mathbf{x}')\rho(\mathbf{x}',t')\zeta(k,t-t') \tag{2.77}$$

Where $\zeta = \zeta_{\text{I,II}}$. The mode functions describe the spatial profile of the induced potential of the ℓm and kn modes of the sphere and the substrate, respectively, and $u_{\ell m}(t)$ and $Q_n(k,t)$

represent the time dependent amplitudes of their surface mode oscillations. The causal response functions $\beta_{\ell m}(t-t')$ and $\zeta(k,t-t')$ are defined in the time domain by the inverse Fourier transform of their frequency dependent representations. In the $d \to \infty$ limit for the slab $\zeta(k,t-t') \to \zeta(t-t')$. Then, by employing a Lorentz oscillator dielectric function (2.41), transformation of the response functions into the time domain may be performed analytically

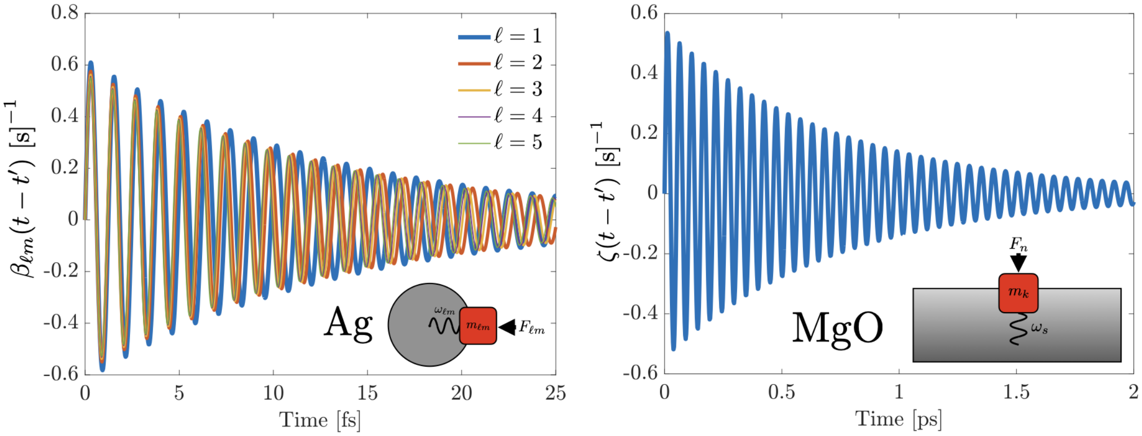

Figure 2.5: Time Domain representation of the surface response functions of a Ag sphere, and an MgO semi-infinite slab. In both cases, the impulse time is initiated at $t' = 0$, and the temporal response is reported in femto and pico second range, respectively. The period of oscillation is determined by the real part of the complex eigenfrequencies, $\Omega_{\ell m}$ and Ω_s. The decay envelope, and lifetime of the oscillation is dictated by the dissipation frequency γ.

$$\begin{aligned} \beta_{\ell m}(t-t') &= \frac{1}{2\pi}\int_{-\infty}^{\infty} d\omega\ \beta_{\ell m}(\omega)e^{-i\omega(t-t')} \\ &= \frac{\tilde{\omega}_{\ell m}^2}{\Omega_{\ell m}} e^{\gamma(t-t')/2}\sin\Omega_{\ell m}(t-t') \end{aligned} \tag{2.78}$$

$$\begin{aligned}\zeta(t-t') &= \frac{1}{2\pi}\int_{-\infty}^{\infty} d\omega\ \zeta(\omega)e^{-i\omega(t-t')} \\ &= \frac{\tilde{\omega}_s^2}{\Omega_s}e^{\gamma(t-t')/2}\sin\Omega_s(t-t').\end{aligned} \tag{2.79}$$

The terms $\Omega_{\ell m} = \sqrt{\omega_{\ell m}^2 - \gamma^2/4}$ and $\Omega_s = \sqrt{\omega_s^2 - \gamma^2/4}$ are the real valued eigenfrequencies of the sphere and substrate surface modes, and $\omega_{\ell m}^2 = \omega_0^2 + \ell\omega_p^2/[\ell(\varepsilon_\infty + 1) + 1]$, $\omega_s^2 = \omega_0^2 + \omega_p^2/(\varepsilon_\infty + 1)$ are their natural oscillation frequencies. In both cases, these are proportional to the natural frequency of the bulk dielectric function, and dressed by an additional frequency term due to a restoring force introduced by the presence of an interface. Finally, the terms $\tilde{\omega}_{\ell m}^2 = \ell\omega_p^2(2\ell+1)/[\ell(\varepsilon_\infty+1)+1]^2$ and $\tilde{\omega}_s^2 = 2\omega_p^2/(\varepsilon_\infty+1)^2$ encode the extent of polarization of the sphere and slab surface modes, as both are proportional to the material's plasma frequency, and therefore the charge carrier density. Comparing Eqns. (2.78) and (2.79) to the particular solution of a damped driven harmonic oscillator $x(t) = \int_{-\infty}^{t} g_{\mathrm{HO}}(t-t')F(t')/m$ (i.e. $g_{\mathrm{HO}}(t-t') = \Omega^{-1}e^{-\gamma(t-t')/2}\sin\Omega(t-t')$) allows for extracting expressions for the generalized forces which act on coordinates $u_{\ell m}$ and Q_n along with the effective mass of the surface modes. In each case, we observe that the forces involve an integral of the spatial mode function against the charge distribution

$$F_{\ell m}(t) = -\int d\mathbf{x}' f_{\ell m}^*(\mathbf{x}')\rho(\mathbf{x}', t) \tag{2.80}$$

$$F_n(k,t) = -\int d\mathbf{x}' \Lambda_n^*(k, \mathbf{x}')\rho(\mathbf{x}', t) \tag{2.81}$$

$$m_{\ell m} = \frac{e^2}{a^3\tilde{\omega}_{\ell m}^2} \tag{2.82}$$

$$m_k = \frac{(ek^2)^2}{\tilde{\omega}_s^2} \tag{2.83}$$

Together, these terms permit the construction of the following equations of motion for the surface responses.

$$m_{\ell m}\ddot{u}_{\ell m}(t) + m_{\ell m}\gamma\dot{u}_{\ell m}(t) + m_{\ell m}\omega_{\ell m}^2 u_{\ell m}(t) = F_{\ell m}(t) \tag{2.84}$$

$$m_k\ddot{Q}_n(k,t) + m_k\gamma\dot{Q}_n(k,t) + m_k\omega_s^2 Q_n(k,t) = F_n(k,t) \tag{2.85}$$

This is a significant result. We have explicitly demonstrated that the electromagnetic surface modes of the sphere and the slab obey harmonic oscillator dynamics when the material's bound charges are perturbed from equilibrium in the presence of external charge distributions. Considering all surface modes indexed by ℓ, m, n, the continuous indexing wavenumber states, and in the limit of no damping, Eqns. (3.26) and (2.85) can be derived from the following Hamiltonians

$$\begin{aligned} H_{\text{sph}} &= \sum_{\ell m}\left[\frac{\mathbf{p}_{\ell m}\cdot\mathbf{p}_{\ell m}^*}{2m_{\ell m}} + \frac{1}{2}m_{\ell m}\omega_{\ell m}^2\mathbf{u}_{\ell m}\cdot\mathbf{u}_{\ell m}^* + \frac{1}{2}\left(\mathbf{F}_{\ell m}\cdot\mathbf{u}_{\ell m}^* + \mathbf{F}_{\ell m}^*\cdot\mathbf{u}_{\ell m}\right)\right] \\ &= H_{\text{sph}}^0 + \sum_{\ell m} V_{\ell m} \end{aligned} \tag{2.86}$$

$$\begin{aligned} H_{\text{slab}} &= \sum_{n=-\infty}^{\infty}\int_0^{\infty} dk\left[\frac{\mathbf{P}_n\cdot\mathbf{P}_n^*}{2m_k} + \frac{1}{2}m_k\omega_s^2\mathbf{Q}_n\cdot\mathbf{Q}_n^* + \frac{1}{2}\left(\mathbf{F}_n\cdot\mathbf{Q}_n^* + \mathbf{F}_n^*\cdot\mathbf{Q}_n\right)\right] \\ &= H_{\text{slab}}^0 + \sum_{n=-\infty}^{\infty}\int_0^{\infty} dk\ V_{kn} \end{aligned} \tag{2.87}$$

Above, we have separated our Hamiltonians into two parts, and unperturbed Hamiltonian, H_i^0, accounting for the internal system energies, and the second part, V_i, representing a perturbation due to external charges. Employing the canonical commutation relation $[u_{\ell m}, p_{\ell' m'}] = i\hbar\delta_{\ell\ell'}\delta_{mm'}$ and $[Q_{nk}, P_{n'k'}] = i\hbar\delta_{nn'}\delta_{kk'}$, we quantize our unperturbed Hamiltonians and introduce standard bosonic raising and lowering operators as

$$H^0_{\mathrm{sph}} = \sum_{\ell m} \hbar\omega_{\ell m} \left[a^\dagger_{\ell m} a_{\ell m} + \frac{1}{2}\right] \tag{2.88}$$

$$H^0_{\mathrm{slab}} = \sum_{n} \int_0^\infty dk\ \hbar\omega_s \left[b^\dagger_{kn} b_{kn} + \frac{1}{2}\right] \tag{2.89}$$

and we define the position and momentum operators as

$$u_{\ell m} = \sqrt{\frac{\hbar}{2m_{\ell m}\omega_{\ell m}}} \left(a^\dagger_{\ell m} + a_{\ell m}\right) \tag{2.90}$$

$$p_{\ell m} = i\sqrt{\frac{\hbar m_{\ell m}\omega_{\ell m}}{2}} \left(a^\dagger_{\ell m} - a_{\ell m}\right) \tag{2.91}$$

$$Q_n = \sqrt{\frac{\hbar}{2m_k\omega_s}} \left(b^\dagger_{kn} + b_{kn}\right) \tag{2.92}$$

$$P_n = i\sqrt{\frac{\hbar m_k\omega_s}{2}} \left(b^\dagger_{kn} - b_{kn}\right). \tag{2.93}$$

We will find these definitions useful in a quantum mechanical treatment of inelastic ion scattering processes addressed in the following section.

Chapter 3

MODELING THE OBSERVABLES OF FAR-FIELD LIGHT AND ION-SCATTERING SPECTROSCOPIES

In this chapter we will demonstrate the utility of mapping the surface mode dynamics of spherical and planar objects onto a harmonic oscillator model. As we shall see, the oscillator serves both as a powerful tool for developing intuition about basic oscillatory systems, as well as a useful and versatile method for modeling spectroscopic measurements, despite the model's relative simplicity.

3.1 The Aborption, Scattering and Extinction Cross Sections of a Dipolar Surface Mode

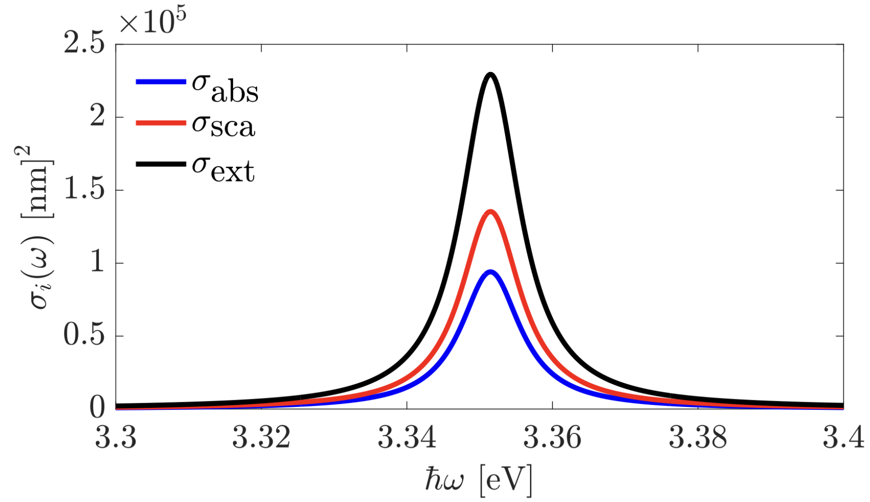

Figure 3.1: The absorption (red), scattering (blue) and extinction (black) cross sections of a radiating dipole, modeled as a harmonic oscillator. The dipole's natural frequency is $\omega_0 = 1$ eV, its damping rate is $\gamma = 0.2$ eV, and the effective mass is $m = 6 \times 10^{-18}$ gm

We begin with a simple example of an oscillating dipole coupled to far-field radiation. Considering the equation of motion for the surface modes of the sphere in the first line of Eqn. (3.26), we consider the lowest order mode ($\ell = 1$), corresponding to a dipolar surface charge density accumulated at the sphere-vacuum interface, induced by an external field. Including a driving force exerted by the field of a time oscillating planewave, $F(t) = eE_0 e^{-i\omega t}$, we write the corresponding equation of motion as

$$m\ddot{\mathbf{u}}(t) + m\gamma\dot{\mathbf{u}}(t) + m\omega_0^2\mathbf{u}(t) = e\mathbf{E}_0 e^{-i\omega t} \tag{3.1}$$

The general solution for this inhomogenous differential equation is

$$\begin{aligned} \mathbf{u}(t) &= e^{-\frac{\gamma}{2}t}\left[\mathbf{u}_0\cos(\omega_0 t) + \frac{\mathbf{v}_0}{\omega_0}\sin(\omega_0 t)\right] + \frac{e}{m}\frac{\mathbf{E}_0 e^{-i\omega t}}{\omega_0^2 - \omega^2 - i\gamma\omega} \\ &= \mathbf{u}_{\mathrm{h}}(t) + \mathbf{u}_{\mathrm{p}}(t) \end{aligned} \tag{3.2}$$

The first term in Eqn. (3.2) (the 'homogeneous solution' $\mathbf{u}_{\mathrm{h}}(t)$) decays exponentially at a rate determined by the dissipation frequency γ as time progresses. The terms $\mathbf{u}_0 = \mathbf{u}(t=0)$, $\mathbf{v}_0 = \dot{\mathbf{u}}(t=0)$ are the initial displacement from equilibrium, and the initial velocity of the oscillator. Eventually the second term (the 'particular solution' $\mathbf{u}_{\mathrm{p}}(t)$) which oscillates continuously at amplitude E_0, dominates the response as information about the oscillatory system's initial conditions decays away. Hence, at the 'steady-state' limit, when initial conditions no longer contribute to $x(t)$ under the influence of a continuous, time-oscillating external force, we find

$$\begin{aligned} \lim_{t\to\infty}\mathbf{u}(t) &= \frac{e}{m}\frac{\mathbf{E}_0 e^{-i\omega t}}{\omega_0^2 - \omega^2 - i\gamma\omega} \\ &= \frac{e}{m}\frac{\mathbf{E}_0 e^{-i(\omega t - \varphi)}}{\sqrt{(\omega_0^2 - \omega^2)^2 + (\gamma\omega)^2}}. \end{aligned} \tag{3.3}$$

The relative phase of the oscillator with respect to the driving field is $\varphi = \tan^{-1}\left(\gamma\omega/[\omega_0^2 - \omega^2]\right)$. When the oscillator is driven at the natural frequency (i.e. $\omega = \omega_0$), the oscillator is $\varphi = \pi/2$ out-of-phase relative to the driving field. We calculate the average power extinguished by integrating the scalar product of the dissipative force, $\mathbf{F}_{\mathrm{damp}}(t) = m\gamma\dot{\mathbf{u}}(t)$, and the time rate of change of the oscillator, $\dot{\mathbf{u}}(t)$ at steady-state. However care must be taken to only integrate the real part of the complex force and coordinate

$$\begin{aligned}
\langle P\rangle_{\text{ext}} &= \frac{1}{\tau}\int_0^\tau dt\ P_{\text{ext}} \\
&= \frac{1}{\tau}\int_0^\tau dt\ \operatorname{Re}\left\{\mathbf{F}_{\text{damp}}(t)\right\}\cdot\operatorname{Re}\left\{\dot{\mathbf{u}}(t)\right\} \\
&= \frac{e^2E_0^2}{2m}\frac{\gamma\omega^2}{(\omega_0^2-\omega^2)^2+(\gamma\omega)^2} \\
&= \frac{1}{2}m\gamma\omega^2|\mathbf{u}(t)|^2,
\end{aligned} \tag{3.4}$$

where the oscillation period $\tau = 2\pi/\omega$. We see that the time averaged dissipated power is proportional to the damping rate. We consider two distinct mechanisms which contribute to the total dissipation of the oscillator's energy: non-radiative absorption, whereby oscillations of the system's bound charges decay to produce heat via internal loss, and radiative losses, whereby energy is carried away via radiation into the electromagnetic far-field. Therefore $\mathbf{F}_{\text{damp}} = \mathbf{F}_{\text{abs}} + \mathbf{F}_{\text{rad}}$. We can derive $\mathbf{F}_{\text{rad}}$ by considering the Larmor power radiated from an accelerated point charge [36]

$$P_{\text{rad}} = \frac{2e^2}{3c^3}\ddot{\mathbf{u}}^2. \tag{3.5}$$

Therefore, time averaged power radiated away from the charge is

$$\begin{aligned}
\langle P\rangle_{\text{scat}} &= \frac{1}{\tau}\frac{2e^2}{3c^3}\int_0^\tau dt\ \ddot{\mathbf{u}}\cdot\ddot{\mathbf{u}} \\
&= \frac{1}{\tau}\frac{2e^2}{3c^3}\left[\dot{\mathbf{u}}(t)\cdot\ddot{\mathbf{u}}(t)\Big|_0^\tau - \int_0^\tau dt\,\dddot{\mathbf{u}}(t)\cdot\dot{\mathbf{u}}(t)\right] \\
&= -\frac{1}{\tau}\int_0^\tau dt\ \mathbf{F}_{\text{rad}}(t)\cdot\dot{\mathbf{u}}(t).
\end{aligned} \tag{3.6}$$

Using Eqn. (3.3) we can demonstrate that the surface term evaluates to zero over an optical cycle, and we arrive at the result that $\mathbf{F}_{\text{rad}} = -2e^2/3c^3\,\dddot{\mathbf{u}} = 2e^2\omega^2/3c^3\dot{\mathbf{u}}$. Naturally, we introduce a radiative and non-radiative damping rate as

$$\mathbf{F}_{\text{damp}} = m(\gamma_{\text{abs}} + \gamma_{\text{rad}})\dot{\mathbf{u}}, \tag{3.7}$$

where γ_{abs} is the rate of energy dissipation to heat, and $\gamma_{\text{rad}} = 2e^2\omega^2/3mc^3$ is the rate of energy dissipation to radiative losses. It should be noted that unlike γ_{abs}, which we model as frequency independent, γ_{rad} has a quadratic dependence on the driving frequency. Now, we differentiate between the absorbed and scattered power, yielding

$$\begin{aligned} \langle P\rangle_{\text{abs}} &= \frac{e^2E_0^2}{2m}\frac{\gamma_{\text{abs}}\omega^2}{(\omega_0^2-\omega^2)^2+(\gamma\omega)^2} \\ &= \frac{1}{2}m\gamma_{\text{abs}}\omega^2|\mathbf{u}(t)|^2 \end{aligned} \tag{3.8}$$

$$\begin{aligned} \langle P\rangle_{\text{scat}} &= \frac{e^2E_0^2}{2m}\frac{\gamma_{\text{rad}}\omega^2}{(\omega_0^2-\omega^2)^2+(\gamma\omega)^2} \\ &= \frac{1}{2}m\gamma_{\text{rad}}\omega^2|\mathbf{u}(t)|^2. \end{aligned} \tag{3.9}$$

Defining the dipole polarizability $\alpha(\omega) = e^2(\omega_0^2 - \omega^2 - i\gamma\omega)^{-1}/m$, and the magnitude of the time averaged Poynting vector of the incident field as $|\langle\mathbf{S}\rangle| = cE_0^2/8\pi$, we arrive at the absorption, scattering, and extinction cross sections, generally defined by $\sigma_i = \langle P\rangle_i/|\langle\mathbf{S}\rangle|$

$$\sigma_{\text{abs}}(\omega) = \frac{4\pi\omega^2}{c}(m/e^2)\gamma_{\text{abs}}|\alpha(\omega)|^2 \tag{3.10}$$

$$\begin{aligned} \sigma_{\text{scat}}(\omega) &= \frac{4\pi\omega^2}{c}(m/e^2)\gamma_{\text{rad}}|\alpha(\omega)|^2 \\ &= \frac{8\pi}{3}k^4|\alpha(\omega)|^2 \end{aligned} \tag{3.11}$$

$$\sigma_{\mathrm{ext}}(\omega) = \frac{4\pi\omega^2}{c}(m/e^2)\gamma|\alpha(\omega)|^2$$

$$= 4\pi k \mathrm{Im}\{\alpha(\omega)\} \tag{3.12}$$

$$= \sigma_{\mathrm{abs}}(\omega) + \sigma_{\mathrm{sca}}(\omega),$$

where above, $k = \omega/c$. The result that the total extinction is the sum of absorption and scattering should be expected due to the conservation of total system energy. From our definition of γ_{rad}, it is straightforward to define the radiation corrected polarizability in terms of a non-radiative (nr) polarizability as

$$\alpha(\omega) = \frac{\alpha_{\mathrm{nr}}(\omega)}{1 - i\frac{2}{3}k^3\alpha_{\mathrm{nr}}(\omega)}, \tag{3.13}$$

where for a point dipole, the non-radiative polarizability can be expressed in terms of the Clausius-Mossotti relation, $\alpha_{\mathrm{nr}}(\omega) = a^3(\varepsilon(\omega) - 1)/(\varepsilon(\omega) + 2)$.

3.2 The Field of a Relativistic Ion, and its Utility as a Spectroscopic Probe

In this section we derive the field of a fast moving ion relative to a fixed reference frame. Considering the resulting spectral representation of the field, we evaluate it's utility as a spectroscopic probe. Beginning with Maxwell's equations for mascroscopic media (2.17). Taking the curl of Faraday's law

$$\nabla \times \nabla \times \mathbf{E} = -\frac{1}{c}\nabla \times \dot{\mathbf{B}} \tag{3.14}$$

For the right hand side we write

$$\nabla \times \nabla \times \mathbf{E} = \nabla(\nabla \cdot \mathbf{E}) - \nabla^2\mathbf{E}$$

$$= \frac{4\pi\nabla\rho_f}{\varepsilon} - \nabla^2\mathbf{E} \tag{3.15}$$

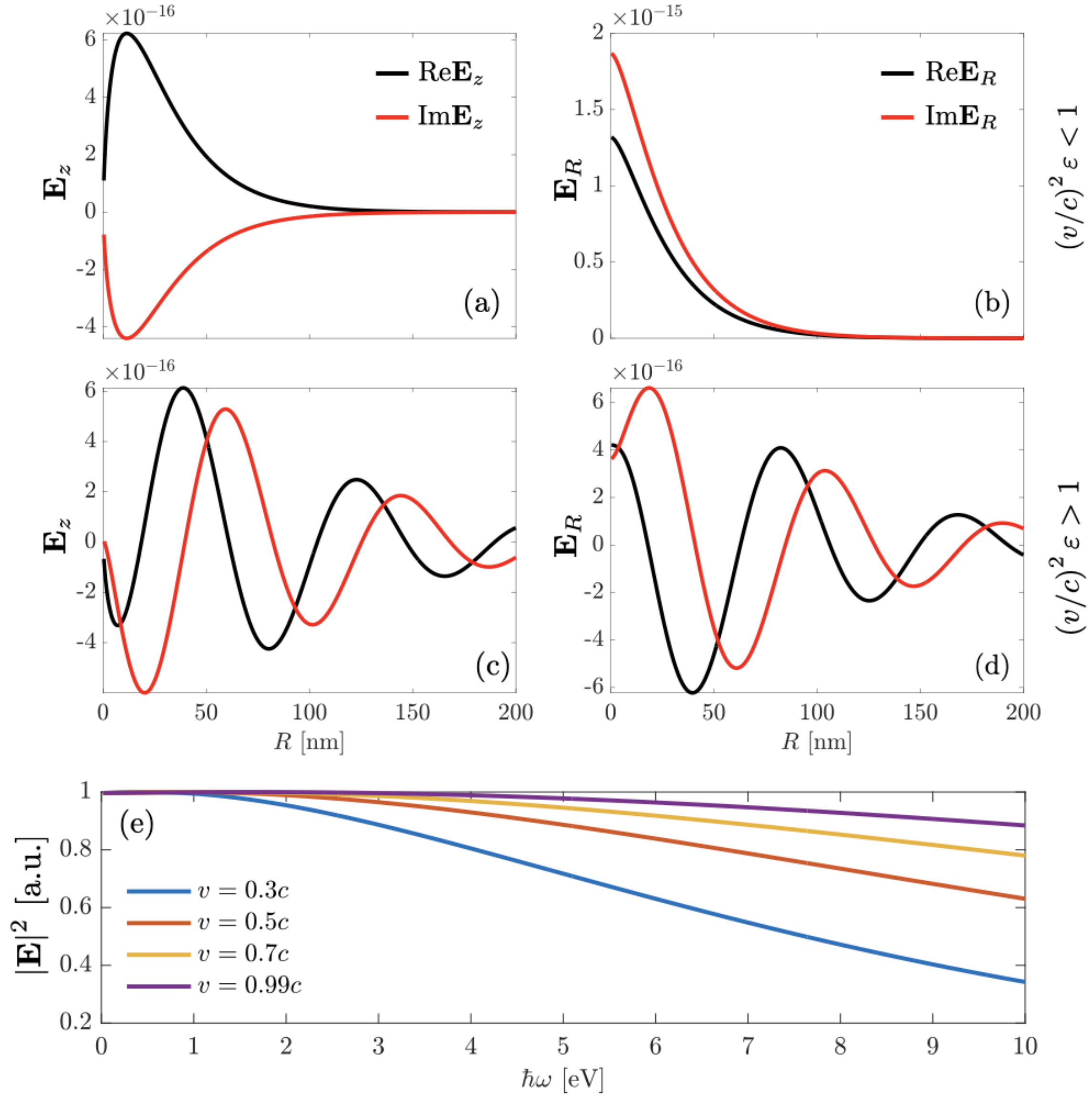

Figure 3.2: (a) Various representations of the electric field of the traveling electron. In panels (a) and (b) demonstrate the evanescent character of the field along coordinates z and R, as the ion travels through the vacuum, and the Lorentz contraction factor γ_L is real valued. In panels (c) and (d), as the ion travels faster than the speed of light in a dispersive, lossy material, where γ_L is complex valued (i.e. $\mathrm{Re}\ \varepsilon = 4, \mathrm{Im}\ \varepsilon = 1$). The oscillatory character of the electric field indicates the onset of radiation, a feature known as the 'Cherenkov effect'. Panels (a)-(d) are all calculated at $\hbar\omega = 10$ eV, and the fields are evaluated over the range $R = 0 - 200$ nm, and at $z = 100$ nm, for an electron traveling at velocity $v = 0.7c$. Panel (e) demonstrates the evolution of $|\mathbf{E}|^2$ across a broad energy spectrum as a function of the ion velocity. As its velocity approaches the speed of light, the spectral distribution of the ion begins to resemble that of a white-light source.

while for the left hand side, we substitute in Ampère's law

$$-\frac{1}{c}\nabla\times\dot{\mathbf{B}} = -\frac{1}{c^2}\left[\ddot{\mathbf{D}} + 4\pi\dot{\mathbf{J}}_f\right]. \tag{3.16}$$

Equating these two results, we construct the wave equation of the electric field in the presence of macroscopic media, sourced by free charges. The current density for an ion moving at velocity $\mathbf{v}$ is $\mathbf{J}_f = \mathbf{v}\rho_f$. Therefore, our wave equation may be written as

$$\nabla^2\mathbf{E} - \frac{1}{c^2}\ddot{\mathbf{D}} = 4\pi\left[\frac{\nabla\rho_f}{\varepsilon} + \frac{\mathbf{v}}{c^2}\rho_f\right]. \tag{3.17}$$

Assuming a local dielectric function description will suffice, we'll consider $\mathbf{D}$, $\mathbf{E}$, and ρ in terms of a Fourier decomposition

$$\begin{aligned}
\mathbf{D}(\mathbf{x},t) &= \frac{1}{(2\pi)^4}\int d\mathbf{k}d\omega\ \mathbf{D}(\mathbf{k},\omega)e^{i(\mathbf{k}\cdot\mathbf{x}-\omega t)} \\
&= \frac{1}{(2\pi)^4}\int d\mathbf{k}d\omega\ \varepsilon(\omega)\mathbf{E}(\mathbf{k},\omega)e^{i(\mathbf{k}\cdot\mathbf{x}-\omega t)} \\
\mathbf{E}(\mathbf{x},t) &= \frac{1}{(2\pi)^4}\int d\mathbf{k}d\omega\ \mathbf{E}(\mathbf{k},\omega)e^{i(\mathbf{k}\cdot\mathbf{x}-\omega t)} \\
\rho_f(\mathbf{x},t) &= \frac{1}{(2\pi)^4}\int d\mathbf{k}d\omega\ \rho_f(\mathbf{k},\omega)e^{i(\mathbf{k}\cdot\mathbf{x}-\omega,t)},
\end{aligned} \tag{3.18}$$

which permits a trivial evaluation of the electric field's Fourier amplitude

$$\mathbf{E}(\mathbf{k},\omega) = -i4\pi\frac{\frac{\mathbf{k}}{\varepsilon(\omega)} - \frac{\omega}{c^2}\mathbf{v}}{k^2 - \frac{\omega^2}{c^2}\varepsilon(\omega)}\rho_f(\mathbf{k},\omega). \tag{3.19}$$

If we define the free charge to be a single traveling point particle, defined spatially by a delta function as $\rho_f(\mathbf{x},t) = e\delta(\mathbf{x} - [\mathbf{r}_0 - \mathbf{v}t])$, where e is a unit of charge, then the charge density in Fourier space is

$$\rho(\mathbf{k},\omega) = e\int d\mathbf{x}dt\ \delta(\mathbf{x}-[\mathbf{r}_0-\mathbf{v}t])e^{-i(\mathbf{k}\cdot\mathbf{x}-\omega t)}$$

$$(3.20)$$

$$= 2\pi e\delta(\mathbf{k}\cdot\mathbf{v}-\omega)e^{i\mathbf{k}\cdot\mathbf{r}_0}$$

The vector $\mathbf{r}_0$ is an arbitrary point of observation. Considering an ion traveling along direction $\hat{\mathbf{z}}$, the ion velocity $\mathbf{v} = v\hat{\mathbf{z}}$, the delta function is $v^{-1}\delta(k_z - \omega/v)$, and we write the electric field in direct space as

$$\mathbf{E}(\mathbf{x},\omega) = -\frac{ie}{\pi v\varepsilon(\omega)}e^{i\frac{\omega}{v}z}\int d\mathbf{k}_\perp e^{i\mathbf{k}_\perp\cdot\mathbf{R}}\frac{k_\perp\hat{\mathbf{R}}+\frac{\omega}{v\gamma_{\mathrm{L}}^2}\hat{\mathbf{z}}}{k_\perp^2+\left(\frac{\omega}{v\gamma_{\mathrm{L}}}\right)^2} \tag{3.21}$$

where the Lorentz contraction factor $\gamma_{\mathrm{L}} = [1-(v/c)^2\varepsilon(\omega)]^{-1/2}$. From the integral definition of the modified Bessel function

$$2\pi K_0(\lambda R) = \int d\mathbf{k}_\perp\frac{e^{i\mathbf{k}_\perp\cdot\mathbf{R}}}{k_\perp^2+\lambda^2} \tag{3.22}$$

and the recursive property $\partial_R K_0(\lambda R) = -\lambda K_1(\lambda R)$, we find for the electric field in frequency space [37, 38]

$$\mathbf{E}(\mathbf{x},\omega) = -\frac{2e\omega}{v^2\gamma_{\mathrm{L}}^2\varepsilon(\omega)}\left[iK_0\left(\frac{\omega R}{v\gamma_{\mathrm{L}}}\right)\hat{\mathbf{z}}-\gamma_{\mathrm{L}}K_1\left(\frac{\omega R}{v\gamma_{\mathrm{L}}}\right)\hat{\mathbf{R}}\right]e^{i\frac{\omega}{v}z}. \tag{3.23}$$

In Fig. (3.2), we explore the spatial and spectral properties of the traveling ion's electric field. Embedded within the Bessel functions of Eqn. (3.23) is the Lorentz contraction factor. Beneath the Cherenkov threshold (i.e ($v\sqrt{\varepsilon} < c$) the field of the swift ion decays evanescently as demonstrated in panels (a)-(b). However, the argument of the Bessel functions assume an imaginary value for a real valued dielectric constant under the condition $v\sqrt{\varepsilon} > c$. For dielectrics which possess an imaginary component, the radiated fields are oscillatory and decay exponentially as they propagate within the material. This oscillatory property of the fields signals the onset of Cherenkov radiation (c)-(d). In (a)-(d) we examine these features of the field at a single energy of 10 eV, at a fixed value of $z = 100$ nm, while the radial component varies over a range of $R = 0 - 200$ nm. In panel (e), we examine the spectral distribution of the swift-ion field over a range of velocities. We see that the spectral profile of the modulus-square of the field becomes more evenly distributed across all energies when ion's velocity approaches the speed of light. In this velocity regime, both the evanescent and radiating fields act as a broad spectrum white light source. This demonstrates the utility of a relativistic free charge carrier as a spectroscopic probe. In the vicinity of a system of either free or bound charges, an exchange of energy mediated by the field interactions of the probing ion with an interrogated system leads to an experimentally measurable energy lost or gained by the probe. These inelastic scattering events occur across a very wide range of energies depending on the type of excitations native to the target material. For decades now, ion scattering instruments have excelled in measuring optical band excitations due to bulk and surface plasmon resonances inherent to Drude-type materials, and interband transitions characteristic in the ultra-violet regime, and even ionization energies and core electron excitations at which tend to reside in the x-ray band. More modern ion scattering instruments are capable of high fidelity measurements deep into the infrared spectrum, probing bulk and surface phonon resonances hosted by typical insulating dielectric materials. In the next few sections, we will discuss in depth as to how we model this process under both a classical and quantum mechanical framework.

3.3 A Classical Approach to Modeling Inelastic Ion Scattering

Considering an ion moving along a straight line trajectory external to the dielectric objects, the average energy exchanged with its environment is characterized by the set of equations [39]

$$\begin{aligned}\langle \Delta E\rangle &= \int_{-\infty}^{\infty} dt\ P(t) \\ &= \int_{0}^{\infty} d(\hbar\omega)\ \hbar\omega\ \Gamma(\omega).\end{aligned} \tag{3.24}$$

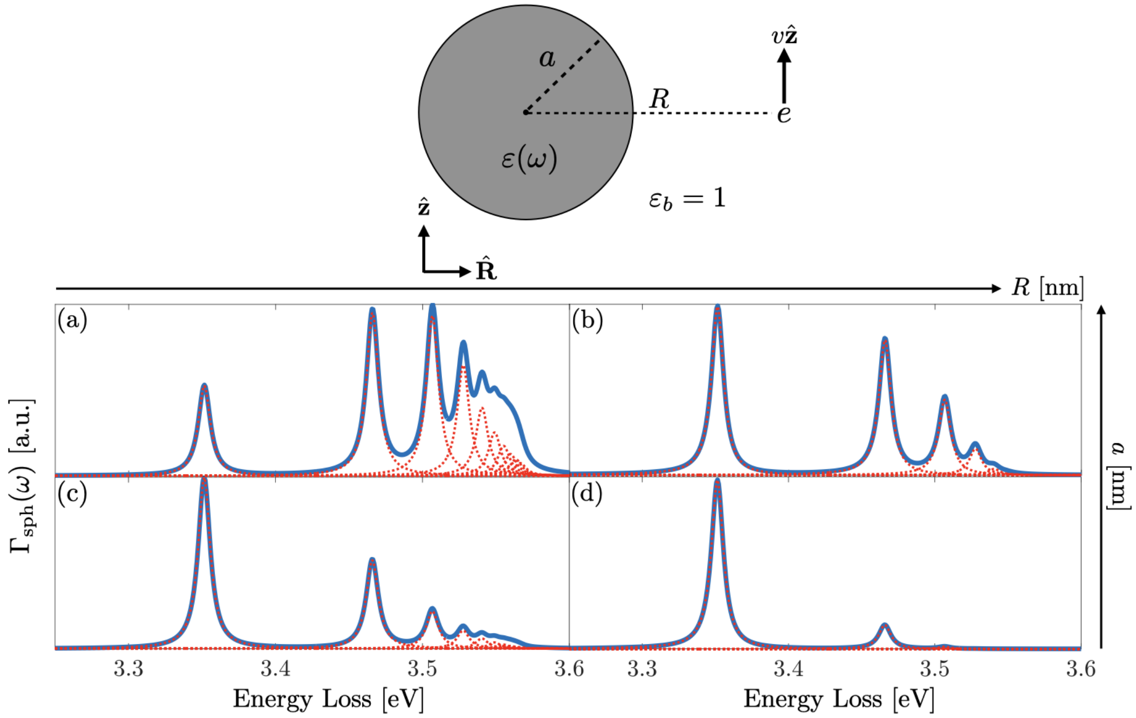

Figure 3.3: Schematic of an ion with charge e traveling along direction $\hat{\mathbf{z}}$ external to an Ag-sphere with 10 keV of kinetic energy. Panels (a) and (b) demonstrate the scattering probability for a radius $a = 25$ nm. In panel (d), the ion travels only 1 nm from the sphere surface (i.e. $R = a + 1$ nm), and in panel (b), 100 nm from the sphere surface (i.e. $R = a + 100$ nm). Panels (c) and (d) consider the same impact factors, R, but for a sphere with a radius $a = 5$ nm. For the smaller impact factors, when the ion is nearly touching the sphere surface, we see the contribution of many higher order multipole response, some of which provide a greater contribution to $\Gamma(\omega)$ than the dipole response in the case of the larger sphere. As the impact factor R is dramatically increases (i.e. $R \gg a$), the contribution of the higher order modes decreases, and the dipole mode begins to dominate the spectral response of the spherical particle. A Drude dielectric function has been implemented to model the response of the free electron gas, with parameters $\varepsilon_\infty = 5.7$, $\gamma = 0.01$ eV, and $\omega_p = 9.3$ eV

We have considered a convenient scenario where the electron, traveling from the infinite past, interacts with the with a target sample, and travels on into the infinite future, hence the bounds on the time integral $t = \pm\infty$. $\Gamma(\omega)$ is the experimentally observed probability distribution density function for an ion scattered inelastically at energy $\hbar\omega$. The power exchanged between the field and a current is defined as

$$P(t) = \int d\mathbf{x}\ \mathbf{E}(\mathbf{x},t) \cdot \mathbf{J}(\mathbf{x},t). \tag{3.25}$$

There is some freedom here in how we define the electric field and the current density, as long as the total energy of interaction is conserved. For example, we may define the electric field $\mathbf{E}$ as the field induced by the probe ion, and $\mathbf{J}$ by the current of the fast ion. Conversely, utilizing the generalized coordinates describing the time dependent amplitudes of oscillation for the surface modes and the generalized forces acting on them, we may rewrite $P_{\text{sph}}(t) = \sum_{\ell m} \mathbf{F}_{\ell m}(t) \cdot \dot{\mathbf{u}}_{\ell m}(t)$ to characterize the energy of interaction between the probe and the sphere, or $P_{\text{slab}}(t) = \sum_n \int dk\ \mathbf{F}_n(k,t) \cdot \dot{\mathbf{Q}}_n(k,t)$ for the slab. In this approach, the collective bound charges inherit the role of the current, and the external probe supplies the force. Considering the latter case, we then attempt to solve for the scattering probability $\Gamma(\omega)$.

3.3.1 Ion Scattering off of a Spherical Target

First for the sphere, we consider Eqn. (2.84). A Fourier transform supplies the steady state solution

$$\begin{aligned} \mathbf{u}_{\ell m}(\omega) &= \frac{\mathbf{F}_{\ell m}(\omega)}{m_{\ell m}} \frac{1}{\omega_{\ell m}^2 - \omega^2 - i\gamma\omega} \\ &= \frac{\alpha_{\ell m}(\omega)}{e^2} \mathbf{F}_{\ell m}(\omega). \end{aligned} \tag{3.26}$$

Above, we have defined a polarizability $\alpha_{\ell m}(\omega) = e^2(\omega_{\ell m}^2 - \omega^2 - i\gamma\omega)^{-1}/m_{\ell m}$, the pole structure of which defines the eigenfrequencies of the multipole responses on the dielectric sphere. Therefore, the expression for the average energy in terms of the power may be written in terms of the Fourier transforms of the generalized coordinates and forces as

$$\begin{aligned}\langle \Delta E\rangle &= \frac{1}{2}\sum_{\ell m}\int_{-\infty}^{\infty} dt\,[\mathbf{F}_{\ell m}(t)\cdot\dot{\mathbf{u}}^*_{\ell m}(t)+\mathbf{F}^*_{\ell m}(t)\cdot\dot{\mathbf{u}}_{\ell m}(t)]\\ &= \frac{1}{2}\sum_{\ell m}\frac{i}{2\pi}\left[\int_{-\infty}^{\infty} d\omega\;\mathbf{F}_{\ell m}(\omega)\cdot\int_{-\infty}^{\infty} d\omega'\;\omega'\;\mathbf{u}^*_{\ell m}(\omega')-\text{c.c.}\right]\delta(\omega-\omega') \qquad (3.27)\\ &= \frac{1}{\pi}\sum_{\ell m}\int_{0}^{\infty} d\omega\;\omega\;\mathrm{Im}\left\{\mathbf{F}^*_{\ell m}(\omega)\cdot\mathbf{u}_{\ell m}(\omega)\right\}.\end{aligned}$$

In the final line of (3.27) we have equated the domains of integration over ω, and now we can immediately evaluate $\Gamma(\omega)$ from Eqn. (3.24), yielding

$$\Gamma_{\text{sph}}(\omega) = \frac{1}{\pi\hbar^2}\sum_{\ell m}\mathrm{Im}\left\{\mathbf{F}^*_{\ell m}(\omega)\cdot\mathbf{u}_{\ell m}(\omega)\right\} \qquad (3.28)$$

An identical approach for the slab reveals

$$\Gamma_{\text{slab}}(\omega) = \frac{1}{\pi\hbar^2}\sum_{n}\int_{0}^{\infty} dk\;\mathrm{Im}\left\{\mathbf{F}_n(k,\omega)^*\cdot\mathbf{Q}_n(k,\omega)\right\}, \qquad (3.29)$$

When the scattered ion is travelling parallel, and external to the dielectric material. This compact and straightforward derivation of the inelastic ion scattering probability highlights the utility of the harmonic oscillator model derived in the previous section. For completeness, we will now derive an expression for $\Gamma(\omega)$ considering the field of the dielectric objects induced by the current distribution of the swift ion, under a quasistatic approximation. The induced field is $\mathbf{E}_{\text{ind}} = -\nabla\Phi_{\text{ind}}$, and therefore, the power is $P(t) = -\int d\mathbf{x}\;\nabla\Phi_{\text{ind}}(\mathbf{x},t)\cdot\mathbf{J}(\mathbf{x},t)$. Recalling the continuity equation $\nabla\cdot\mathbf{J} = \dot{\rho}$, and integrating by parts, we find

$$P(t) = \int d\mathbf{x}\;\Phi_{\text{ind}}(\mathbf{x},t)\dot{\rho}(\mathbf{x},t). \qquad (3.30)$$

We calculate the time averaged energy as

$$\begin{aligned}\langle \Delta E \rangle &= \int d\mathbf{x}dt\ \Phi_{\text{ind}}(\mathbf{x},t)\dot{\rho}(\mathbf{x},t) \\ &= \frac{1}{\pi}\int d\mathbf{x}\int_0^{\infty} d\omega\ \omega\ \text{Im}\left\{\rho^*(\mathbf{x},\omega)\Phi_{\text{ind}}(\mathbf{x},\omega)\right\}.\end{aligned} \tag{3.31}$$

As in the case of the generalized forces and coordinates, we have used a method of Fourier decomposition to express ρ and Φ_{ind} in a spectral representation. Again, equating the domain of integration over ω with that of the integral of the scattering probability distribution, we identify $\Gamma(\omega)$ as

$$\begin{aligned}\Gamma(\omega) &= \frac{1}{\pi\hbar^2}\int d\mathbf{x}\ \text{Im}\left\{\rho^*(\mathbf{x},\omega)\Phi_{\text{ind}}(\mathbf{x},\omega)\right\} \\ &= \frac{1}{\pi\hbar^2}\int d\mathbf{x}d\mathbf{x}'\ \text{Im}\left\{\rho^*(\mathbf{x},\omega)G_{\text{ind}}(\mathbf{x},\mathbf{x}';\omega)\rho(\mathbf{x}',\omega)\right\},\end{aligned} \tag{3.32}$$

where we've utilized the result of Eqn. (2.71) to relate the scattering probability to the induced Green's function. For a single ion moving external to the dielectric object along direction $\hat{\mathbf{z}}$, we define the charge distribution $\rho(\mathbf{x},t) = e\delta(\mathbf{R}-\mathbf{R}_0)\delta(z-vt)$, where $\mathbf{R}_0 = x_0\hat{\mathbf{x}} + y_0\hat{\mathbf{y}}$ is the radial cylindrical coordinate of the ion. The spectral representation of the charge density is then trivial to compute

$$\rho(\mathbf{x},\omega) = \frac{e}{v}\delta(\mathbf{R}-\mathbf{R}_0)e^{i\frac{\omega}{v}z} \tag{3.33}$$

In this case, our expression for $\Gamma(\omega)$ evaluates to

$$\Gamma(\omega) = \left(\frac{e}{\hbar v}\right)^2\frac{1}{\pi}\int dzdz'\ \text{Im}\left\{G_{\text{ind}}(\mathbf{R}_0,z,\mathbf{R}_0,z')e^{-i\frac{\omega}{v}(z-z')}\right\}. \tag{3.34}$$

Now, solving for the scattering probability is a matter of evaluating the integral over the induced Green's function. In the case of the sphere, recalling the relationship between the spherical harmonic functions and the associated Legendre polynomials, where $\cos\theta = z/r$

$$Y_{\ell m}(\theta,\phi) = \sqrt{\frac{2\ell+1}{4\pi}\frac{(\ell-m)!}{(\ell+m)!}}P_{\ell m}(\cos\theta)e^{im\phi}, \tag{3.35}$$

and the non-trivial integral identity [34, 40]

$$\int_{-\infty}^{\infty} dz\ r^{-(\ell+1)}P_{\ell m}\left(\frac{z}{r}\right)e^{ikz} = 2\left(\frac{ik}{|k|}\right)^{\ell-m}\frac{k^{\ell}}{(\ell-m)!}K_m(|k|R), \tag{3.36}$$

where $K_m(x)$ is the modified Bessel function of the second kind, we produce the scattering probability for the sphere, yielding

$$\Gamma_{\text{sph}}(\omega) = \frac{4a}{\pi}\left(\frac{e}{\hbar v}\right)^2\sum_{\ell m}\left(\frac{\omega a}{v}\right)^{2\ell}\frac{K_m^2\left(\frac{\omega R_0}{v}\right)}{(\ell-m)!(\ell+m)!}\text{Im}\left\{\beta_{\ell m}(\omega)\right\}, \tag{3.37}$$

in the case of an ion beam traveling completely external to the sphere. When the radial coordinate R is large, so that the traveling ion is very far away from the sphere, the ratio of the higher order Bessel functions to the growing factorial terms in the denominator decreases rapidly for large values of ℓm. This fall-off of higher order mode contributions occurs even more rapidly for smaller values of the sphere radius a. Therefore when $R \gg a$, only the $\ell = 1$ term significantly contributes to the scattering probability, and we can safely approximate a purely dipolar scatting probability as

$$R \gg a: \quad \Gamma_{\text{sph}}(\omega) \approx \frac{|\mathbf{E}(\mathbf{x},\omega)|^2}{\pi\hbar^2}\text{Im}\left\{\alpha_{\text{nr}}(\omega)\right\}, \tag{3.38}$$

where $\alpha_{\text{nr}}(\omega) = a^3(\varepsilon(\omega)-1)/(\varepsilon(\omega)+2)$ is the well known Clausius-Mossotti polarizability for a non-radiating point dipole. $\mathbf{E}(\mathbf{x},\omega)$ is the spectral representation of the fast ion's field from Eqn. (3.23) evaluated in the quasistatic limit, where $\gamma_{\text{L}} = 1$. Here, we may conveniently introduce a first-order radiative correction using our result from Eqn. (3.13), where the total contribution to the inelastic scattering by the dipole may be separated into radiative and non-radiative contributions. The radiative contribution simplifies to

$$\begin{aligned}\Gamma_{\text{sph}}^{\text{rad}}(\omega) &= \frac{|\mathbf{E}(\mathbf{x},\omega)|^2}{\pi\hbar^2}\frac{2}{3}k^3|\alpha(\omega)|^2 \\ &= \frac{2e^2}{3\pi\hbar^2}k^3|\mathbf{u}(\omega)|^2.\end{aligned} \tag{3.39}$$

Commonly, this radiative contribution to inelastic ion scattering is referred to as *cathodoluminescence*, and it is proportional to the photon emission probability from a material in the presence of a fast moving ion. It can be thought of as the inverse process of the photoelectric effect, whereby electrons are emitted in the presence of electromagnetic radiation with sufficient energy to overcome a material's work function [29].

3.3.2 Ion Scattering off of a Planar Surface

Moving on now to considering an ion moving external and parallel to a slab's surface, we utilize Eqns. (2.63) and (3.34). First defining a charge distribution in its spectral form as $\rho(\mathbf{x},\omega) = e\delta(z-z_0)e^{i\omega R/v}$, and then using the addition theorem [31] for the Bessel functions $J_0(kR) = J_0(kvt)J_0(kvt') + 2\sum_{n=1}^{\infty} J_n(kvt)J_n(kvt')\cos k\phi$, where the coordinate $R = \sqrt{(vt)^2 + (vt')^2 - 2(vt)(vt')\cos k\phi}$, and $\phi = 0$ is the angle between vt and vt'. Therefore $R = v(t-t') = v\tau$, and we evaluate the scattering probability as

$$\Gamma_{\text{slab}}(\omega) = \frac{1}{\pi}\left(\frac{e}{\hbar}\right)^2 \int dt \int_0^\infty dk\ e^{-2kb}\ \text{Im}\left\{\zeta(k,\omega)\int_{-\infty}^{\infty} d\tau\ J_0(kv\tau)e^{i\omega\tau}\right\}. \tag{3.40}$$

The Fourier transform of the Bessel functions are well known, and for the integral on τ we find

$$\int_{-\infty}^{\infty} d\tau\ J_0(kv\tau)e^{i\omega\tau} = \frac{2}{v}\frac{\Theta\left(1-\left[\frac{\omega}{kv}\right]^2\right)}{\sqrt{k^2-\left(\frac{\omega}{v}\right)^2}}, \tag{3.41}$$

and the scattering probability rate reduces to [41, 34]

$$\frac{\partial\Gamma_{\text{slab}}(\omega)}{\partial t} = \frac{2}{\pi v}\left(\frac{e}{\hbar}\right)^2 \int_{\frac{\omega}{v}}^{\infty} dk \frac{e^{-2kb}}{\sqrt{k^2-\left(\frac{\omega}{v}\right)^2}}\text{Im}\left\{\zeta(k,\omega)\right\}. \tag{3.42}$$

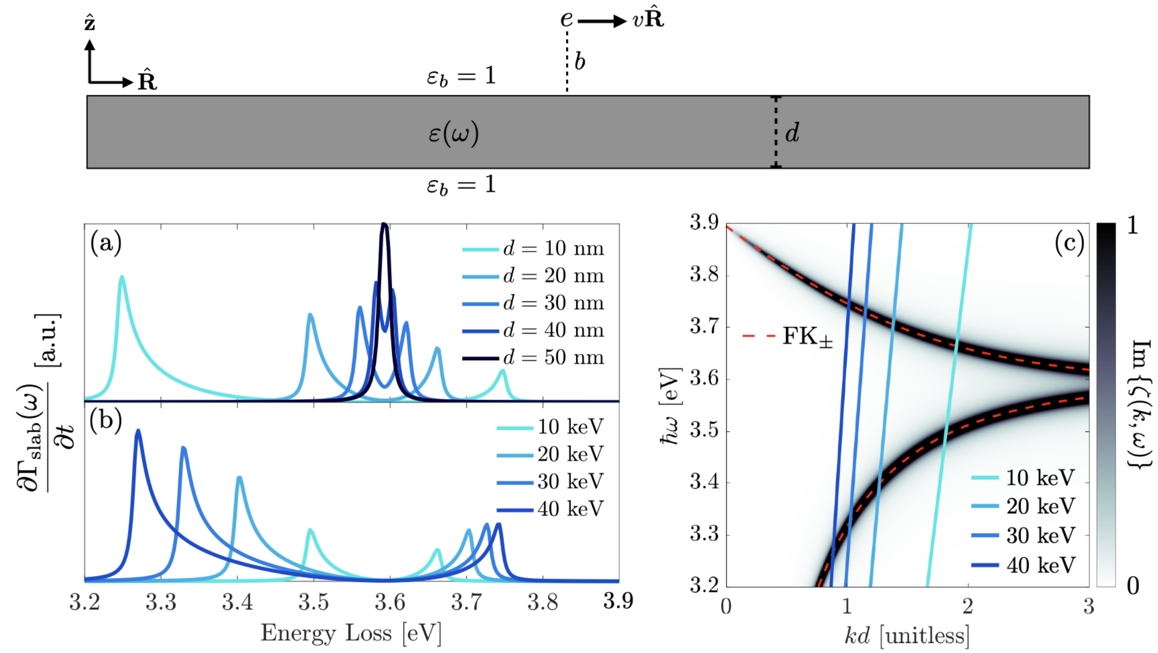

Figure 3.4: Panels (a) and (b) demonstrate the inelastic scattering probability of an Ag-slab with varying depth (i.e. $d = 10{-}50$ nm), and varying kinetic energies (i.e. KE $= 10{-}40$ keV) of the fast ion probe, which travels parallel and external to the slab's surface. As the slab depth d is increased, a decrease in peak splitting between the transverse (+) and longitudinal (-) Fuchs-Kliewer (FK$_\pm$) modes of the slab occurs, eventually converging to the single resonance associated with the semi-infinite half space $(\varepsilon(\omega)-1)/(\varepsilon(\omega)+1)$. Additionally, as the kinetic energy of the ion increases, we observe peak splitting due to the evolving points of intersection between the electron and slab dispersion curves (c). As expected the FK$_\pm$ modes encoded in the pole structure of the slab's surface response function $\zeta(k,\omega)$ coincide with the peaks in the surface plot of Im$\{\zeta(k,\omega)\}$. We've used the same Drude dielectric function parameters that were used in the example for the sphere in Figure 3.3.

In the limit that the slab depth $d \to \infty$, the response function $\lim_{d\to\infty} \zeta(k,\omega) = (\varepsilon(\omega) - 1)/(\varepsilon(\omega)+1)$ surrenders its dependence on the indexing wavenumber k and the remaining integral evaluates to the zeroth order modified Bessel function of the second kind, as

$$K_0\left(\frac{2\omega b}{v}\right) = \int_{\frac{\omega}{v}}^{\infty} dk \frac{e^{-2kb}}{\sqrt{k^2 - \left(\frac{\omega}{v}\right)^2}}, \tag{3.43}$$

and the scattering probability rate simplifies to

$$\lim_{d\to\infty} \frac{\partial \Gamma_{\text{slab}}(\omega)}{\partial t} = \frac{2}{\pi v}\left(\frac{e}{\hbar}\right)^2 K_0\left(\frac{2\omega b}{v}\right) \operatorname{Im}\left\{\frac{\varepsilon(\omega)-1}{\varepsilon(\omega)+1}\right\}. \tag{3.44}$$

In the case of the slab of finite depth, we observe that the resulting resonance structure in $\Gamma_{\text{slab}}(\omega)$ is inherently dependent upon both the slab depth and the probing ion's velocity, as depicted in Fig 3.4. The slab's dispersion diagram demonstrates a profile of allowed momentum transfer to the system's bound charges across across a range of frequencies. The peaks in the dispersion curve coincide with the real valued eigenmodes of the slab extracted from the poles of (2.63). These are commonly referred to as the transverse and longitudinal Fuchs-Kliewer modes. The resulting momentum conservation is reflected in the scattering spectrum at the energies where the scattering probability is maximal. In addition, varying the slab depth alters the pole structure of the response function $\zeta(k,\omega)$, also leading to increased peak splitting in the scattering spectrum.

3.3.3 Ion Scattering in Bulk Material

From Eqn. (3.25), if we define the current $\mathbf{J}(\mathbf{x},t) = e\mathbf{v}\delta(\mathbf{x} - \mathbf{r}_{\text{e}}(t))$, where $\mathbf{r}_{\text{el}}(t)$ is the time dependent location of the traveling ion, the power exchanged between the probe and the near field is defined by $e\mathbf{v}\cdot\mathbf{E}(\mathbf{r}_{\text{e}}(t),t)$. Then from Eqn. (3.24), we solve for scattering probability, yielding

$$\Gamma(\omega) = \frac{e\mathbf{v}}{\pi\hbar^2\omega} \cdot \int_{-\infty}^{\infty} dt \ \text{Re}\{\mathbf{E}(\mathbf{r}_{\text{e}}(t),\omega)e^{-i\omega t}\}. \tag{3.45}$$

Using Eqn. (3.2), we then solve immediately for the bulk inelastic scattering probability, expressing it as a time dependent rate

$$\frac{\partial\Gamma(\omega)}{\partial t} = \frac{1}{v}\left(\frac{e}{\pi\hbar}\right)^2 \mathrm{Im}\left\{-\frac{1}{\gamma_{\mathrm{L}}^2\varepsilon(\omega)}\int d\mathbf{k}_\perp \frac{1}{k_\perp^2+\left(\frac{\omega}{\gamma_{\mathrm{L}} v}\right)^2}\right\} \tag{3.46}$$

$$= \frac{1}{\pi v}\left(\frac{e}{\hbar}\right)^2 \mathrm{Im}\left\{-\frac{1}{\gamma_{\mathrm{L}}^2\varepsilon(\omega)}\ln\left(\gamma_{\mathrm{L}}^2+1\right)\right\}.$$

To arrive at the final line of Eqn. (3.46), we have evaluated the integral in cylindrical coordinates (i.e. $\int d\mathbf{k}_\perp = 2\pi\int_0^{\omega/v} k_\perp dk_\perp$), and an upper bound ω/v has been imposed on the wavenumber perpendicular to the trajectory of the traveling ion.

3.4 A Quantum Approach to Modeling Inelastic Ion Scattering (Energy Loss and Gain)

To apply a quantum mechanical treatment to modeling inelastic ion scattering, we utilize time dependent perturbation theory [42, 43]. If we consider a quantum state $|\psi_{t_0}\rangle$ at some initial time $t = t_0$, and its evolution to $|\psi_t\rangle$ at some future time t, the time evolution is determined by unperturbed Hamiltonian H_0, according to the time dependent Schrödinger equation

$$i\hbar\frac{\partial}{\partial t}|\psi_t\rangle = H_0|\psi_t\rangle. \tag{3.47}$$

The time evolved eigenstates of H_0 are related by a phase factor $|\psi_t\rangle = e^{-iE_0(t-t_0)/\hbar}|\psi_{t_0}\rangle$. Substituted into Eqn. (3.47), we arrive at the time independent Schrödinger equation

$$H_0|\psi_{t_0}\rangle = E_0|\psi_{t_0}\rangle, \tag{3.48}$$

indicating that these state vectors are *stationary states* which when projected into direct space (i.e. $\langle\mathbf{x}|\psi\rangle$) rotate through the complex plane of their Hilbert space at frequency $E_0/\hbar$. Consider now that our quantum state is perturbed due to an external potential V.

The time dependent Schrödinger equation becomes

$$i\hbar\frac{\partial}{\partial t}\left|\psi_t\right\rangle = \left[H_0 + V\right]\left|\psi_t\right\rangle . \tag{3.49}$$

To examine how this perturbation will affect our quantum state, it is convenient to work in the interaction picture, where our state vectors are defined in terms of their Schrödinger picture counterparts via a unitary operator, as $\left|\tilde{\psi}(t)\right\rangle = e^{iH_0t/\hbar}\left|\psi_t\right\rangle$, where the 'tilde' indicates that we are transformed into the interaction picture. Additionally, we define the perturbative operator in the interaction picture as $\tilde{V}(t) = e^{iH_0t/\hbar}Ve^{-iH_0t/\hbar}$. Substituting our transformed state vector and operator $\tilde{V}$ into (3.47), we find

$$\frac{\partial}{\partial t}\left|\tilde{\psi}(t)\right\rangle = \frac{1}{i\hbar}\tilde{V}(t)\left|\tilde{\psi}(t)\right\rangle . \tag{3.50}$$

We observe that in a perturbation, the time derivative of the state vector in the interaction picture is zero, and the state does not evolve in time. Now, a straightforward integration step yields

$$\left|\tilde{\psi}(t)\right\rangle = \left|\tilde{\psi}(t_0)\right\rangle + \frac{1}{i\hbar}\int_{t_0}^{t} dt'\ \tilde{V}(t')\left|\tilde{\psi}(t')\right\rangle , \tag{3.51}$$

where we have arrived at an iterative equation defining the state vector at some arbitrary time t, after it has evolved from its initial state at time t_0 due to the influence of the perturbation V. Writing the first few terms in the iterative series, we find

$$\begin{aligned}
\left|\tilde{\psi}(t)\right\rangle &= \left|\tilde{\psi}(t_0)\right\rangle + \frac{1}{i\hbar}\int_{t_0}^{t} dt'\ \tilde{V}(t')\left\{\left|\tilde{\psi}(t_0)\right\rangle + \frac{1}{i\hbar}\int_{t_0}^{t'} dt''\ \tilde{V}(t'')\left|\tilde{\psi}(t'')\right\rangle\right\} + \ldots \\
&= \left|\tilde{\psi}(t_0)\right\rangle + \frac{1}{i\hbar}\int_{t_0}^{t} dt'\ V\tilde{(t')}\left|\tilde{\psi}(t_0)\right\rangle + \frac{1}{(i\hbar)^2}\int_{t_0}^{t} dt'\ \tilde{V}(t')\int_{t_0}^{t'} dt''\ \tilde{V}(t'')\left|\tilde{\psi}(t_0)\right\rangle + \ldots \\
&= \left[1 + \frac{1}{i\hbar}\int_{t_0}^{t} dt'\ \tilde{V}(t') + \frac{1}{(i\hbar)^2}\int_{t_0}^{t} dt'\ \tilde{V}(t')\int_{t_0}^{t'} dt''\ \tilde{V}(t'') + \ldots\right]\left|\tilde{\psi}(t_0)\right\rangle \\
&= U(t,t_0)\left|\tilde{\psi}(t_0)\right\rangle,
\end{aligned} \tag{3.52}$$

where we have formed a formal perturbative or ‘Dyson’ series [17, 44], and defined the unitary time evolution operator $U(t, t_0)$. Projecting the time evolved state onto an arbitrary eigenstate $|f\rangle$ of the unperturbed Hamiltonian we find

$$\begin{aligned}
\left\langle f\middle|\tilde{\psi}(t)\right\rangle &= \langle f|\, U(t,t_0)\left|\tilde{\psi}(t_0)\right\rangle \\
&= \sum_j c_j(t),
\end{aligned} \tag{3.53}$$

where each contributing term of the Dyson series is represented by the projection coefficient $c_j(t)$. For weak perturbations, the first order term provides a good approximation for the time evolved state. Considering the sphere's Hamiltonian from Eqn. (2.86), the perturbative contribution to the system Hamiltonian from each mode ℓm is $V_{\ell m} = \left(\mathbf{F}_{\ell m}\cdot\mathbf{u}^*_{\ell m} + \mathbf{F}^*_{\ell m}\cdot\mathbf{u}_{\ell m}\right)/2$. Additionally, we may also express the perturbation via the induced potential (2.72) in terms of the sphere's mode function (2.74) and generalized coordinate (2.90) as $V_{\ell m} = e f_{\ell m}(\mathbf{x}) u_{\ell m}$, where e is a unit of charge. Preparing the initial state in the infinite past (i.e. $t_0 \to -\infty$, and $V \to 0$), before the onset of the perturbation, we define $\left|\tilde{\psi}(t_0)\right\rangle = |n_{\ell_0 m_0}\ k\rangle$, where $|n_{\ell m}\rangle$ is an initial multipole moment state of the sphere and $|k\rangle$ is the initial state of the probing electron. We denote the final state as $\left|n'_{\ell_1 m_1}\ k'\right\rangle$. The initial and final states are eigenstates of the unperturbed Hamiltonian, where $H_0\,|n_{\ell m}\ k\rangle = E_{\ell m k}\,|n_{\ell m}\ k\rangle$. Under a first order approximation, the scattering probability amplitude of finding our system in a final excited multipole state is simply

$$c_1(t) = \left\langle n'_{\ell_1 m_1}\ k' \middle| n_{\ell_0 m_0}\ k\right\rangle + \frac{1}{i\hbar}\int_{-\infty}^{t} dt'\ \left\langle n'_{\ell_1 m_1}\ k'\right| \tilde{V}_{\ell m}(t')\left|n_{\ell_0 m_0}\ k\right\rangle. \tag{3.54}$$

For a complete set of orthonormal states, the first term $\left\langle n'_{\ell_1 m_1}\ k' \middle| n_{\ell_0 m_0}\ k\right\rangle = \delta_{n_{\ell_0 m_0} n'_{\ell_1 m_1}}\delta_{kk'}$, and therefore goes to zero if we find our system in a final eigenstate which differs from the initial eigenstate, as we would expect in an inelastic scattering process. Then, acting the unitary operators $U, U^{\dagger}$ on the intial and final eigenstates, we find

$$\begin{aligned} c_1(t) &= \frac{1}{i\hbar}\int_{-\infty}^{t} dt'\,\left\langle n'_{\ell_1 m_1}\ k'\right| e^{\frac{i}{\hbar}H_0 t'} V_{\ell m} e^{-\frac{i}{\hbar}H_0 t'}\left|n_{\ell_0 m_0}\ k\right\rangle \\ &= \frac{1}{i\hbar}\left\langle n'_{\ell_1 m_1}\ k'\right| V_{\ell m}\left|n_{\ell_0 m_0}\ k\right\rangle \int_{-\infty}^{t} dt'\ e^{i(\omega_{\ell m}+q_z v)t'} \\ &= \frac{1}{i\hbar}\left\langle n'_{\ell_1 m_1}\ k'\right| V_{\ell m}\left|n_{\ell_0 m_0}\ k\right\rangle \frac{e^{i(\omega_{\ell m}+q_z v)t}}{i(\omega_{\ell m}+q_z v)} \\ &= \frac{1}{i\hbar}\bar{T}_{fi}\frac{e^{i(\omega_{\ell m}+q_z v)t}}{i(\omega_{\ell m}+q_z v)}. \end{aligned} \tag{3.55}$$

Above, we haved introduced the transition frequency $\omega_{\ell m} = (E'_{\ell_1 m_1} - E_{\ell_0 m_0})/\hbar$, and have assumed a 'non-recoil' approximation for the inelastically scattered ion (i.e. $q_z v \approx (k'_z - k_z)v$, where v is the ion velocity). The term $\bar{T}_{fi}$ represents the remaining time-independent matrix element. For an ion traversing a focused path along direction z both prior to and after the scattering event, we introduce the following ansatz for the ion wavefunction

$$\begin{aligned}\Psi(\mathbf{x}) &= \langle \mathbf{x}|k\rangle \\ &= \frac{1}{\sqrt{L}}\psi(\mathbf{R})e^{ik_z z}.\end{aligned} \tag{3.56}$$

L represents the quantized box length, introduced for the purposes of normalization. For a tightly focused beam of ions, reminiscent of STEM electrons with beam widths of 1Å [45, 46], we may approximate that the radial part of the ion wavefunction satisfies the condition $|\psi(\mathbf{R})|^2 \approx \delta(\mathbf{R}-\mathbf{R}_0)$, where $\mathbf{R}_0$ is the traveling ion's radial coordinate. Evaluating the remaining matrix element by inserting the resolution of identity $\mathbb{1} = \int d\mathbf{x}\, |\mathbf{x}\rangle \langle \mathbf{x}|$, and find

$$\begin{aligned}\bar{T}_{fi} &= \int d\mathbf{x}d\mathbf{x}' \left\langle n'_{\ell_1 m_1}\ k' \middle| \mathbf{x}\right\rangle \langle \mathbf{x}|\, V_{\ell m}\, |\mathbf{x}\rangle' \, \langle \mathbf{x}|' \, |n_{\ell_0 m_0}\ k\rangle \\ &= \frac{1}{L}\left\langle n'_{\ell_1 m_1}\right| u_{\ell m} \left|n_{\ell_0 m_0}\right\rangle \int dz\ f_{\ell m}(\mathbf{R}_0, z)e^{iq_z z}\end{aligned} \tag{3.57}$$

Now, considering the trajectory of the ion extending to infinite bounds along z, the final integral is easily evaluated with the identity reported in Eqn. (3.36). We find for the projection coefficient

$$c_1(t) = -\frac{2e}{i\hbar L}\left\langle n'_{\ell_1 m_1}\right| u_{\ell m} \left|n_{\ell_0 m_0}\right\rangle a^{\ell-1}\left(i\frac{q_z}{|q_z|}\right)^{\ell-m}\frac{q_z^{\ell}K_m(|q_z|R_0)e^{im\phi}}{\sqrt{(\ell-m)!(\ell+m)!}}\frac{e^{i(\omega_{\ell m}+q_z v)t}}{i(\omega_{\ell m}+q_z v)}. \tag{3.58}$$

Introducing a finite linewidth to the transition frequency under the limit $\omega_{\ell m} = \lim_{\gamma\to 0^+} \omega_{\ell m} + i\gamma$, we may trivially evaluate the transition probability rate as

$$\begin{aligned}\frac{d}{dt}|c_1(t)|^2 &= \left(\frac{2e}{\hbar L}\right)^2 |\left\langle n'_{\ell_1 m_1}\right| u_{\ell m} \left|n_{\ell_0 m_0}\right\rangle|^2 a^{2\ell-2} \frac{q_z^{2\ell} K_m^2(|q_z|R_0)}{(\ell-m)!(\ell+m)!} \frac{2\gamma e^{2\gamma t}}{(\omega_{\ell m} + q_z z)^2 + \gamma^2} \\ &= \frac{1}{\tau_{i\to f}},\end{aligned} \tag{3.59}$$

and then evaluate the transition rate in the limit $\gamma \to 0^+$, resulting in

$$\begin{aligned}\frac{1}{\tau_{i\to f}} &= 2\pi \left(\frac{2e}{\hbar L}\right)^2 |\left\langle n'_{\ell_1 m_1}\right| u_{\ell m} \left|n_{\ell_0 m_0}\right\rangle|^2 a^{2\ell-2} \frac{q_z^{2\ell} K_m^2(|q_z|R_0)}{(\ell-m)!(\ell+m)!} \delta(\omega_{\ell m} + q_z v) \\ &= \frac{2\pi}{\hbar^2} |\left\langle n_{\ell_1 m_1}\ k'\right| V_{\ell m} \left|n_{\ell_0 m_0}\ k\right\rangle|^2 \delta(\Delta E/\hbar).\end{aligned} \tag{3.60}$$

Above, we have arrive at 'Fermi's golden rule' for the ion-sphere scattering process, having utilized the definition for the delta function $2\pi\delta(\Delta E/\hbar) = \lim_{\gamma\to 0^+} 2\gamma/[(\omega_{\ell m} + q_z v)^2 + \gamma^2]$, and defined $\Delta E/\hbar = \omega_{\ell m} + q_z v$. We find the total transition probability by integrating over the entire temporal domain of the ion trajectory, via

$$\begin{aligned}\mathcal{P}_{\ell m} &= \int_0^{L/v} dt \frac{1}{\tau_{i\to f}} \\ &= \frac{L}{v}\frac{1}{\tau_{i\to f}}.\end{aligned} \tag{3.61}$$

Finally, the total inelastic scattering probability per unit energy is calculated by integrating over the final momentum state of the electron, and summing over all multipole states of the target, as

$$\begin{aligned}\Gamma(\omega) &= \frac{L}{2\pi\hbar v^2}\sum_{\ell m}\int dq_z\ P_{\ell m}\ \delta(\frac{\omega}{v}+q_z) \\ &= \frac{4}{\pi}\left(\frac{e}{\hbar v a}\right)^2\sum_{\ell m}\left(\frac{\omega a}{v}\right)^{2\ell}\frac{K_m^2(\frac{|\omega|R_0}{v})}{(\ell-m)!(\ell+m)!}\mathrm{Im}\{\alpha_{\ell m}(\omega)\},\end{aligned} \tag{3.62}$$

where we have defined the multimode polarizability as

$$\alpha_{\ell m}(\omega) = \frac{1}{\hbar}\frac{|\left\langle n'_{\ell_1 m_1}\right| u_{\ell m}\left|n_{\ell_0 m_0}\right\rangle|^2}{\omega_{\ell m}-\omega-i\gamma}. \tag{3.63}$$

Having illustrated that the electromagnetic surface modes of both the sphere and slab obey harmonic oscillator dynamics, we now see that the inelastic scattering probability is inherently dependent on the allowed transitions of the target. The corresponding probability for transitions between states $\left|n_{\ell_0 m_0}\right\rangle \to \left|n'_{\ell_1 m_1}\right\rangle$ is determined by calculating the remaining matrix element defined in the numerator of Eqn. (3.63). To accomplish this, one can utilize the well known solutions to the 3D-isotropic harmonic oscillator wavefunctions in spherical coordinates [47]. We will demonstrate now that the occupation number for a collection of oscillators which obey boson statistics at finite temperature is determined by the Bose-Einstein distribution (i.e. $n = (\exp(\hbar\omega/k_{\mathrm{B}}T)-1)^{-1}$, where k_{B} is the Boltzmann constant). We begin by considering the expectation value for the energy of the oscillator with the unperturbed Hamiltonian

$$\begin{aligned}\langle E\rangle &= \langle n| H |n\rangle \\ &= \langle n| \hbar\omega\left(a^\dagger a+\frac{1}{2}\right)|n\rangle \\ &= \hbar\omega\left(n+\frac{1}{2}\right).\end{aligned} \tag{3.64}$$

It is therefore apparent that the expectation value of the set of creation and annihilation operators $a^\dagger a$, which we name the *number operator*, is simply

$$\begin{aligned}\langle a^\dagger a\rangle &= \langle n|\, a^\dagger a\, |n\rangle \\ &= n,\end{aligned} \tag{3.65}$$

and n is the *occupation number*, representing the measured average energy one would find by probing an ensemble of non-interacting, identical oscillators, or a singular system after many uncorrelated measurements. The average energy can also be calculated by considering the probability for occupation of a state from the Boltzmann factor and the partition function. For a quantum harmonic oscillator, the occupation probability of state m is $P(m) = e^{-\beta E_m}/q(\beta)$, where $E_m = \hbar\omega(m + 1/2)$ is the energy of the m^{th} eigenstate of the oscillator, $\beta = (k_{\mathrm{B}}T)^{-1}$, and $q(\beta) = \sum_{j=0}^{\infty} e^{-\beta E_j}$ is the partition function, which sums over all of the available energetic states of the oscillator. The average energy is then

$$\begin{aligned}\langle E\rangle &= \sum_{m=0}^{\infty} P(m)E_m \\ &= \frac{\sum_m \hbar\omega(m+1/2)e^{-\beta\hbar\omega(m+1/2)}}{\sum_j e^{-\beta\hbar\omega(j+1/2)}} \\ &= \frac{\hbar\omega}{2} - \frac{\frac{\partial}{\partial\beta}\sum_m e^{-\beta\hbar\omega m}}{\sum_j e^{-\beta\hbar\omega j}}\end{aligned} \tag{3.66}$$

Taking the opportunity to rewrite the remaining sums in terms of a geometric series (i.e. $\sum_{k=0}^{\infty} x^k = \frac{1}{1-x};\;\; |x| < 1$), the average energy of the oscillator evaluates to

$$\begin{aligned}\langle E\rangle &= \hbar\omega\left(\frac{1}{e^{\beta\hbar\omega}-1} + \frac{1}{2}\right) \\ &= \hbar\omega\left(n + \frac{1}{2}\right),\end{aligned} \tag{3.67}$$

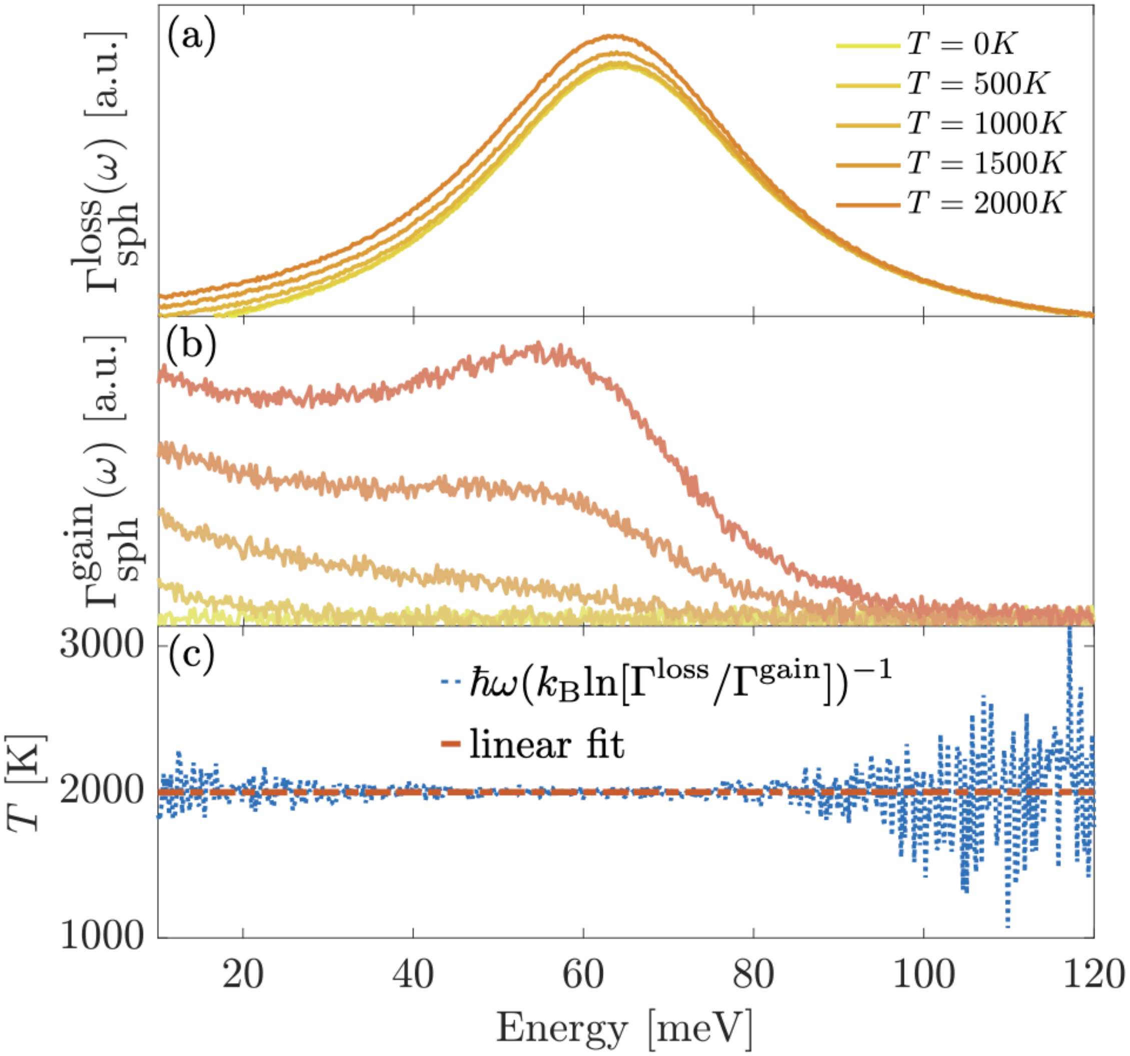

Figure 3.5: (a) The thermally assisted scattered loss probability, and (b) the thermally assisted scattered gain probability for an amorphous carbon sphere at temperatures ranging from T $= 0 - 2000K$. Gaussian white noise has been artificially added to both signals in an attempt to replicate the contribution from typical ambient noise present in an experimental setting. In panel (c) the temperature is evaluated as proportional to the natural logarithm of the ratio of the scattered loss and gain signals, as dictated by the principle of detailed balance. The scatter loss and gain are contributed to by a surface phonon mode supported by the carbon sphere. To model the phononic response of the carbon sphere, we have utilized a Lorentz oscillator dielectric function, with a damping rate of $\gamma = 39.1$ meV, a natural frequency $\omega_0 = 17$ meV, a plasma frequency $\omega_p = 148$ meV, and a static contribution of $\epsilon_\infty = 3.39$.

where we have found that the occupation number is equal to the Bose-Einstein distribution. Therefore, considering the influence of finite system temperature at thermal equilibrium gives rise to two distinct inelastic scattering processes. First, we consider the process by which a quanta of energy is lost by the ion, and inherited by the oscillator as dictated by the Knocker-delta term $\delta_{n'_{\ell m} n_{\ell m}+1}$. In the second process, a quanta of energy is gained by the ion and lost by the oscillator as dictated by $\delta_{n'_{\ell m} n_{\ell m}-1}$. Considering the ratio of the two scattering probability distributions, we find

$$\begin{aligned} \Gamma^{\text{gain}}_{\text{sph}}(\omega)/\Gamma^{\text{loss}}_{\text{sph}}(\omega) &= \frac{n_{\ell m}}{n_{\ell m}+1} \\ &= e^{-\beta\hbar\omega}. \end{aligned} \tag{3.68}$$

This result, in the form a Boltzmann factor, is in agreement with the well known principle of *detailed balance*. It indicates that the rate of absorption and emission of a quanta of energy are equal when the system is in contact with a thermal bath. This relationship between the gain and loss contributions to the inelastic scattering signal has been exploited in nanolocalized temperature measurements in dielectric materials [48, 49].

3.4.1 Inelastic Coulomb Scattering

As an addendum to our section on the quantum treatment of inelastic ion scattering, we also include a few brief remarks on Coulomb scattering. We will see shortly that the result is very similar to that of the sphere. Beginning with the Green's function of the Coulomb potential

$$\begin{aligned} G_{\text{Coul}}(\mathbf{x}, \mathbf{x}') &= \frac{1}{|\mathbf{x}-\mathbf{x}'|} \\ &= \sum_{\ell m} \frac{r'^{\ell}}{r^{\ell+1}} \frac{4\pi}{2\ell+1} Y_{\ell m}(\theta,\phi) Y^*_{\ell m}(\theta',\phi'), \end{aligned} \tag{3.69}$$

The Coulomb potential in the presence of an arbitrary charge distribution $\rho(\mathbf{x},t)$ may be decomposed into a spatial mode function $\lambda_{\ell m}(\mathbf{x})$ and an electric multipole moment $u_{\ell m}(t)$ as

$$\begin{aligned}\Phi_{\text{Coul}}(\mathbf{x},t) &= \int d\mathbf{x}'\ G_{\text{Coul}}(\mathbf{x},\mathbf{x}')\rho(\mathbf{x}',t) \\ &= \sum_{\ell m} \lambda_{\ell m}(\mathbf{x}) u_{\ell m}(t),\end{aligned} \tag{3.70}$$

where we define the mode function and multipole moment as

$$\lambda_{\ell m}(\mathbf{x}) = \sqrt{\frac{4\pi}{2\ell+1}} \frac{Y_{\ell m}(\theta,\phi)}{r^{\ell+1}} \tag{3.71}$$

$$u_{\ell m}(t) = \sqrt{\frac{4\pi}{2\ell+1}} \int d\mathbf{x}'\ r'^{\ell} Y^{*}_{\ell m}(\theta',\phi')\rho(\mathbf{x}',t). \tag{3.72}$$

Critically, we have enforced that the mode functions tend to zero at large distances (i.e. $\lim_{r\to\infty} \lambda_{\ell m}(\mathbf{x}) = 0$) from the target location r'. It is worth noting here that the mode functions we have identified for the Coulomb potential are nearly identical to that of the sphere, save an additional parameter of the sphere's radius in Eqn. (2.74). The multipole moment can be naturally elevated to a quantum mechanical operator defined via the matrix element

$$\langle \mathbf{x} |\, u_{\ell m} \,| \mathbf{x}' \rangle = e \sqrt{\frac{4\pi}{2\ell+1}} r'^{\ell} Y^{*}_{\ell m}(\theta',\phi')\delta(\mathbf{x}-\mathbf{x}'). \tag{3.73}$$

We then define the interaction energy as $V(\mathbf{x},t) = e\Phi_{\textbf{Coul}}(\mathbf{x},t)$, where e is a unit of charge. Following an approach identical to evaluating the inelastic scattering probability for the electromagnetic surface modes on the sphere, we find the inelastic scattering probability per unit energy lost by the traveling charge in the presence of the Coulomb potential, yielding

$$\Gamma(\omega) = \frac{4}{\pi}\left(\frac{e}{\hbar v}\right)^{2} \sum_{\ell m} \left(\frac{\omega}{v}\right)^{2\ell} \frac{K_m^2\left(\frac{|\omega| R_0}{v}\right)}{(\ell-m)!(\ell+m)!} \text{Im}\left\{\alpha_{\ell m}(\omega)\right\}, \tag{3.74}$$

where we have defined the multi-mode electrostatic polarizability for the single electron atom as

$$\alpha_{\ell m}(\omega) = \frac{1}{\hbar} \frac{|\langle n_1\ \ell_1\ m_1|\, u_{\ell m}\, |n_0\ \ell_0\ m_0\rangle\,|^2}{\omega_{fi} - \omega - i\eta}. \tag{3.75}$$

We note here that inelastic scattering is possible only under the condition that the matrix element is non zero. This is determined by selection rules for transitions between final and initial states. As in the case of the surface modes of the sphere, these selection rules will be dictated by the eigenstates of the atom. Using Eqn. (3.73), and inserting the resolution of identity into our matrix element, we find

$$\begin{aligned} \langle n_1\ \ell_1\ m_1|\, u_{\ell m}\, |n_0\ \ell_0\ m_0\rangle &= \int d\mathbf{x}d\mathbf{x}'\, \langle n_1\ \ell_1\ m_1|\mathbf{x}\rangle \,\langle \mathbf{x}|\, u_{\ell m}\, \left|\mathbf{x}'\right\rangle \left\langle \mathbf{x}'\right|n_0\ \ell_0\ m_0\rangle \\ &= e\sqrt{\frac{4\pi}{2\ell+1}} \int d\mathbf{x}\ \Psi^*_{n_1\ell_1 m_1}(\mathbf{x}) r^\ell Y_{\ell m}(\theta,\phi) \Psi^*_{n_0\ell_0 m_0}(\mathbf{x}) \end{aligned} \tag{3.76}$$

In this case, we are considering the eigenstates of the Hydrogen atom, where the known transition rules are $\ell_1 = \ell_0 \pm \ell$, and $m_1 = m_0, m_0 \pm m$.

Chapter 4

COUPLING BETWEEN ELECTROMAGNETIC SURFACE MODES

In this chapter we explore coupling between electromagnetic surface modes of dielectric objects, mediated by their induced electric fields. We begin with a simple example of two coupled radiating dipolar oscillators, and again derive the time averaged power associated with and absorption, scattering and extinction. We then explore the effects of this coupling on the inelastic scattering signal and examine the spectral image of the dipole system at the spectral peaks of the scattering probability.

4.1 The Absorption, Scattering and Extinction Cross Sections of Two Electromagnetically Coupled Dipolar Surface Modes

Expanding from the single oscillator case represented by Eqn. (3.1), we consider the case of two electromagnetically coupled oscillating dipoles, represented by the time dependent coordinates $u_1(t)$ and $u_2(t)$. The coupled equations of motion are

$$m_1\ddot{\mathbf{u}}_1(t) + m_1\gamma_1\dot{\mathbf{u}}_1(t) + m_1\omega_1^2\mathbf{u_1}(t) = e\mathbf{E}_{\text{tot}}(\mathbf{r}_1, t) \tag{4.1}$$

$$m_2\ddot{\mathbf{u}}_2(t) + m_2\gamma_2\dot{\mathbf{u}}_2(t) + m_2\omega_2^2\mathbf{u_2}(t) = e\mathbf{E}_{\text{tot}}(\mathbf{r}_2, t), \tag{4.2}$$

where m_i are the effective masses of the dipolar surface modes, the dissipation rates are the sum of the non-radiative and radiative contributions $\gamma_i = \gamma_{i,\text{abs}} + \gamma_{i,\text{rad}}$, where $\gamma_{i,\text{rad}} = 2e^2\omega^2/3m_ic^3$, and ω_i are the natural frequencies of the coupled dipole oscillators. The external fields $\mathbf{E}_{\text{tot}}(\mathbf{r}_i, t) = \mathbf{E}_{\text{dip}}(\mathbf{r}_i, t) + \mathbf{E}_{\text{pw}}(\mathbf{r}_i, t)$ evaluated at the location of each dipole $\mathbf{r}_i$, include the contribution of the field of an external planewave, and the radiated fields of the neighboring dipoles. Considering the limiting case where the two dipoles are spatially confined to a common confocal point, and therefore experience an identical driving force

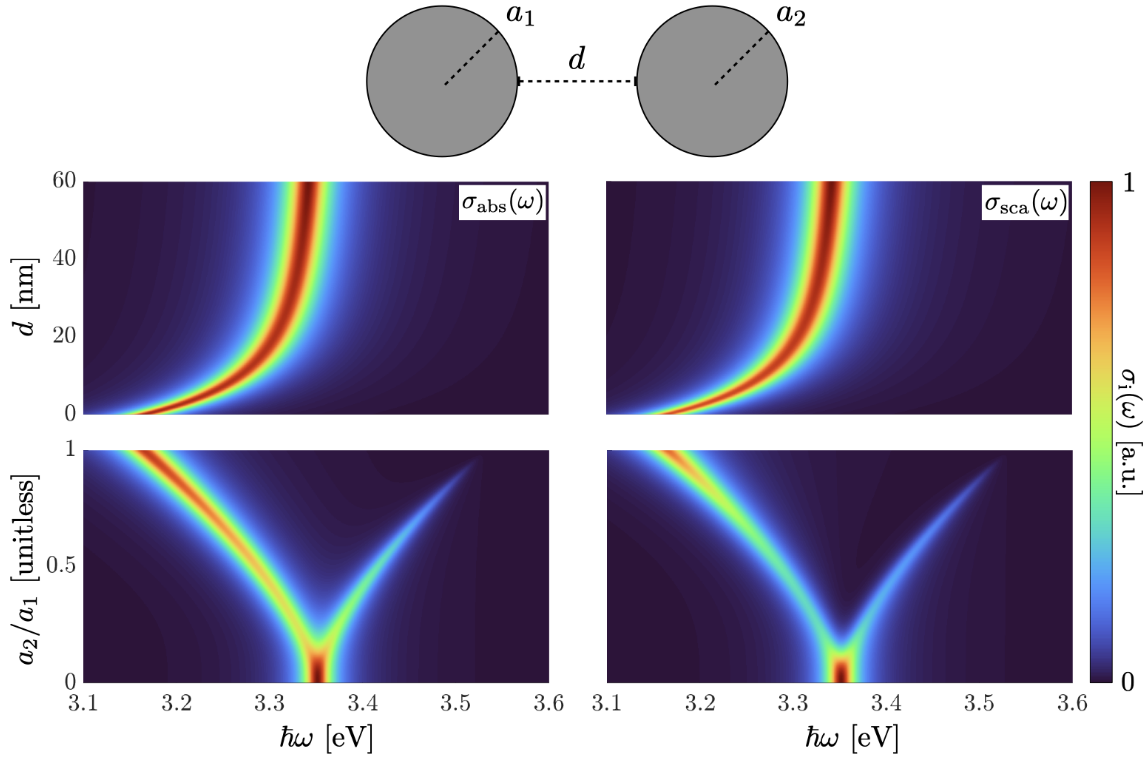

Figure 4.1: Surface plots exploring the evolution of the absorption and scattering cross sections for the dipolar surface modes of two electromagnetically coupled Ag-spheres in a head-to-tail collinear (→→) configuration. In the lower panels, the sphere radius a_1 is fixed at a value of 15 nm, while the radius a_2 is varied from 0 to 15 nm. When $a_2 = 0$, we recover the response of only a single sphere with a peak in both scattering and absorption around $\hbar\omega \approx 3.35$ eV. As the size of the second sphere is increased, we observe a splitting of the cross sections into a low and high energy branch, indicating the formation of two normal mode responses for the dimer system. When the two sphere radii are equal, only the lower energy mode remains. In the upper panels, the interparticle distance is varied from 0 to 60 nm. As the interparticle distance is increased, the dipolar surface modes become decoupled, and the maximum of the cross sections returns to normal mode energy of the single particle.

from the external field. We model the incident field as that of a planewave, and write

$$\mathbf{E}_{\mathrm{pw}}(\mathbf{r}_i, t) = \mathbf{E}_0 e^{-i\omega t} \tag{4.3}$$

The electric dipole radiation field is

$$\mathbf{E}_{i,\mathrm{dip}}(\mathbf{x}, t) = e\mathbf{u}_i(t) \cdot \mathbf{\Lambda}(\mathbf{x} - \mathbf{r}_i), \tag{4.4}$$

where we have introduced the dipole relay tensor

$$\mathbf{\Lambda}(\mathbf{x}) = k^3 \left[\frac{1}{(kr)^3}(3\hat{\mathbf{r}}\hat{\mathbf{r}} - \mathbb{1}) - \frac{i}{(kr)^2}(3\hat{\mathbf{r}}\hat{\mathbf{r}} - \mathbb{1}) - \frac{1}{kr}(\hat{\mathbf{r}}\hat{\mathbf{r}} - \mathbb{1}) \right] e^{ikr}. \tag{4.5}$$

The unit vectors $\hat{\mathbf{r}}$ point in the direction between the dipole and an observation point. Defining a coupling term $g = e^2 \hat{\mathbf{u}}_1 \cdot \mathbf{\Lambda}(\mathbf{r}) \cdot \hat{\mathbf{u}}_2$, where the vector $\mathbf{r} = \mathbf{r}_1 - \mathbf{r}_2$ is the distance between the dipoles, we then write down the following coupled equations of motion

$$m_1 \ddot{\mathbf{u}}_1(t) + m_1 \gamma_1 \dot{\mathbf{u}}_1(t) + m_1 \omega_1^2 \mathbf{u}_1(t) - g\mathbf{u}_2(t) = e\mathbf{E}_0 e^{-i\omega t} \tag{4.6}$$

$$m_2 \ddot{\mathbf{u}}_2(t) + m_2 \gamma_2 \dot{\mathbf{u}}_2(t) + m_2 \omega_2^2 \mathbf{u}_2(t) - g\mathbf{u}_1(t) = e\mathbf{E}_0 e^{-i\omega t}. \tag{4.7}$$

Evaluated in the steady-state limit where $\mathbf{u}_i(t) = \mathbf{u}_i(\omega) e^{-i\omega t}$, we find

$$(\omega_1^2 - \omega^2 - i\gamma_1 \omega)\mathbf{u}_1(\omega) - \frac{g}{m_1}\mathbf{u}_2(\omega) = \frac{e}{m_1}\mathbf{E}_0 \tag{4.8}$$

$$(\omega_2^2 - \omega^2 - i\gamma_2 \omega)\mathbf{u}_2(\omega) - \frac{g}{m_2}\mathbf{u}_1(\omega) = \frac{e}{m_2}\mathbf{E}_0. \tag{4.9}$$

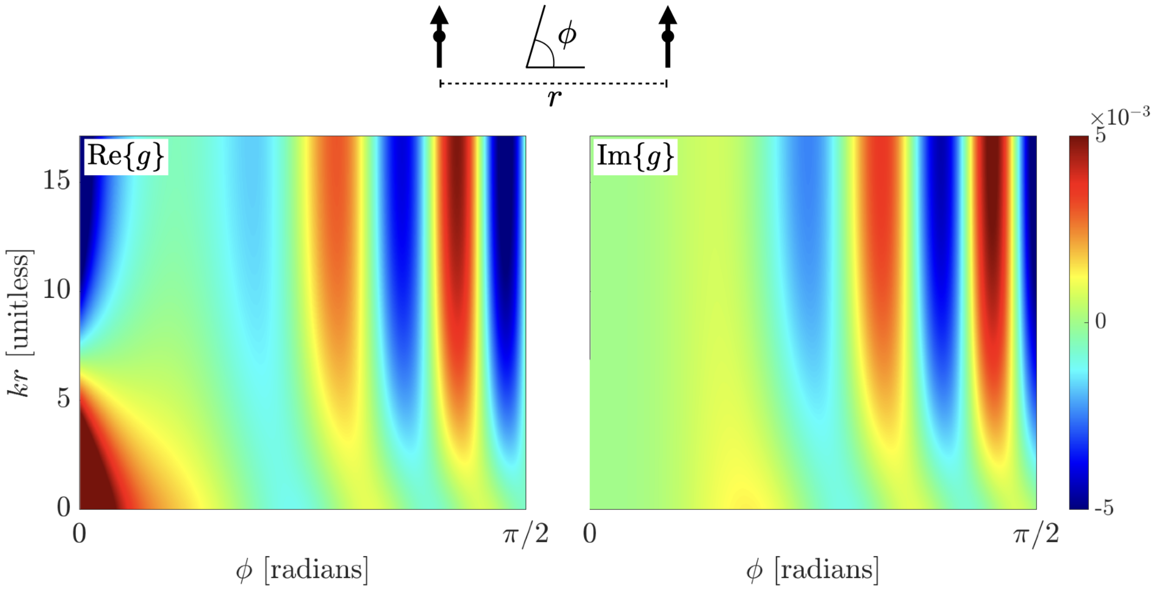

Figure 4.2: Examination of the coupling term $g = e^2\hat{\mathbf{u}}_1 \cdot \mathbf{\Lambda}(\mathbf{r}) \cdot \hat{\mathbf{u}}_2$ as a function of unitless kr and the common angle ϕ which evolves from a collinear orientation $\rightarrow\rightarrow$, to a parallel orientation $\uparrow\uparrow$, between two dipoles interacting via their induced fields. We have plotted both the real and imaginary parts of g, where in particular $\mathrm{Im}\{g\}$ contributes to constructive ($\mathrm{Im}\{g\} > 0$) and destructive ($\mathrm{Im}\{g\} < 0$) interference in far field scattering between the two coupled dipoles. At small distances (i.e. $kr \rightarrow 0$) between the coupled dipoles, $\mathrm{Im}\{g\} \rightarrow 0$, and the coupling parameter is almost entirely real valued and near-field interactions dominate. In the near-field limit, we observe that for a collinear orientation, $\mathrm{Re}\{g\} > 0$, indicating an energetically favorable configuration of the dipoles. In a parallel orientation $\mathrm{Re}\{g\} < 0$, indicating an energetically unfavorable configuration of the dipoles.

Solving the linear system of equations, we find solutions for the Fourier amplitudes of the oscillator coordinates, which are

$$\mathbf{u}_1(\omega) = \frac{e\mathbf{E}_0}{m_1} \frac{Z_2(\omega) + \frac{g}{m_2}}{Z_1(\omega)Z_2(\omega) - \frac{g^2}{m_1 m_2}} \tag{4.10}$$

$$\mathbf{u}_2(\omega) = \frac{e\mathbf{E}_0}{m_2} \frac{Z_1(\omega) + \frac{g}{m_1}}{Z_1(\omega)Z_2(\omega) - \frac{g^2}{m_1 m_2}}, \tag{4.11}$$

We have used the abbreviated notation $Z_i(\omega) = \omega_i^2 - \omega^2 - i\gamma_i\omega$ for each individual dipole's spectral response. We notice in the limit that $|\mathbf{r}_1 - \mathbf{r}_2| \rightarrow \infty$, $g \rightarrow 0$, the oscillators are completely decoupled, and we recover the solution for the Fourier amplitude of a single oscillator found in Eqn. (3.1). Now, writing our solutions in the time domain, we find

$$
\begin{aligned}
\mathbf{u}_1(t) &= \mathbf{u}_1(\omega)e^{-i\omega t} \\
&= \frac{e\mathbf{E}_0}{m_1}\left|\frac{Z_2(\omega)+\frac{g}{m_2}}{Z_1(\omega)Z_2(\omega)-\frac{g^2}{m_1 m_2}}\right| e^{-i(\omega t-\varphi_1)} \qquad (4.12) \\
&= \frac{e\mathbf{E}_0}{m_1}\left|A_1(\omega)\right| e^{-i(\omega t-\varphi_1)} \\
\mathbf{u}_2(t) &= \mathbf{u}_2(\omega)e^{-i\omega t} \\
&= \frac{e\mathbf{E}_0}{m_2}\left|\frac{Z_1(\omega)+\frac{g}{m_1}}{Z_1(\omega)Z_2(\omega)-\frac{g^2}{m_1 m_2}}\right| e^{-i(\omega t-\varphi_2)} \qquad (4.13) \\
&= \frac{e\mathbf{E}_0}{m_2}\left|A_2(\omega)\right| e^{-i(\omega t-\varphi_2)}.
\end{aligned}
$$

The relative phase terms $\varphi_i = \tan^{-1}\left(\mathrm{Im}\{A_i\}/\mathrm{Re}\{A_i\}\right)$. Having solved the equations of motion for each oscillator, we can now evaluate the means by which power is dissipated by the system. As in the previous case of the single oscillator, we computed the total power extinction via $\langle P\rangle_{\mathrm{ext}} = \frac{1}{\tau}\int_0^\tau dt\ \mathrm{Re}\{\mathbf{F}_{\mathrm{damp}}(t)\}\cdot\mathrm{Re}\{\dot{\mathbf{u}}(t)\}$, where $\mathbf{F}_{\mathrm{damp}}$ represented the sum of dissapative forces acting on an oscillator. Unlike the single oscillator, we have an additional coupling force included in our equations of motion which will contribute to the dissipated power over an optical cycle, along with the already familiar absorption and scattering processes. From Eqns. (4.7), the time averaged power contribution from each oscillator due to coupling is

$$\begin{aligned}\langle P\rangle^1_{\text{coup}} &= \frac{1}{\tau}\int_0^\tau dt\ \text{Re}\{-g\mathbf{u}_2(t)\}\cdot\text{Re}\{\dot{\mathbf{u}}_1(t)\} \\ &= \frac{\omega}{2}\frac{e^2E_0^2}{m_1m_2}|A_1(\omega)||A_2(\omega)|\text{Im}\{g\}\end{aligned} \tag{4.14}$$

$$\begin{aligned}\langle P\rangle^2_{\text{coup}} &= \frac{1}{\tau}\int_0^\tau dt\ \text{Re}\{-g\mathbf{u}_1(t)\}\cdot\text{Re}\{\dot{\mathbf{u}}_2(t)\} \\ &= \frac{\omega}{2}\frac{e^2E_0^2}{m_1m_2}|A_1(\omega)||A_2(\omega)|\text{Im}\{g\},\end{aligned} \tag{4.15}$$

and the total contribution to the power from coupling is

$$\begin{aligned}\langle P\rangle^{\text{tot}}_{\text{coup}} &= \langle P\rangle^1_{\text{coup}} + \langle P\rangle^2_{\text{coup}} \\ &= \omega\frac{e^2E_0^2}{m_1m_2}|A_1(\omega)||A_2(\omega)|\text{Im}\{g\} \\ &= \omega|\mathbf{u}_1(\omega)||\mathbf{u}_2(\omega)|\text{Im}\{g\}.\end{aligned} \tag{4.16}$$

Evidently, the power dissipated due to coupling introduces an interference term to the total scattered power between the coupled dipoles

$$\begin{aligned}\langle P\rangle^{\text{tot}}_{\text{sca}} &= \langle P\rangle^1_{\text{sca}} + \langle P\rangle^2_{\text{sca}} + \langle P\rangle^{\text{tot}}_{\text{coup}} \\ &= \frac{\omega^2}{2}\left[m_1\gamma_{1,\text{rad}}|\mathbf{u}_1(\omega)|^2 + m_2\gamma_{2,\text{rad}}|\mathbf{u}_2(\omega)|^2\right] + \omega|\mathbf{u}_1(\omega)||\mathbf{u}_2(\omega)|\text{Im}\{g\}\end{aligned} \tag{4.17}$$

The individual scattering terms are calculated in the usual way $\langle P\rangle^{i}_{\mathrm{sca}} = m\gamma_{i,\mathrm{rad}}\tau^{-1}\int_0^\tau dt\,\mathrm{Re}\{\dot{\mathbf{u}}_i(t)\}\cdot \mathrm{Re}\{\dot{\mathbf{u}}_i(t)\}$. For the absorbed power we find

$$\begin{aligned}\langle P\rangle^{\mathrm{tot}}_{\mathrm{abs}} &= \langle P\rangle^{1}_{\mathrm{abs}} + \langle P\rangle^{2}_{\mathrm{abs}} \\ &= \frac{\omega^2}{2}\left[m_1\gamma_{1,\mathrm{abs}}|\mathbf{u}_1(\omega)|^2 + m_2\gamma_{2,\mathrm{abs}}|\mathbf{u}_2(\omega)|^2\right].\end{aligned} \tag{4.18}$$

Before taking a final step in deriving the optical cross sections, we'll now define the effective or dressed polarizability for each of the coupled dipoles as $\mathbf{p}_i(\omega) = e\mathbf{u}_i(\omega) = \tilde{\alpha}_i(\omega)\mathbf{E}_0$. After some algebra we find

$$\tilde{\alpha}_1(\omega) = \frac{\alpha_1(\omega) + \frac{g}{e^2}\alpha_1(\omega)\alpha_2(\omega)}{1 - \frac{g^2}{e^4}\alpha_1(\omega)\alpha_2(\omega)} \tag{4.19}$$

$$\tilde{\alpha}_2(\omega) = \frac{\alpha_2(\omega) + \frac{g}{e^2}\alpha_1(\omega)\alpha_2(\omega)}{1 - \frac{g^2}{e^4}\alpha_1(\omega)\alpha_2(\omega)}, \tag{4.20}$$

Where $\alpha_i(\omega) = e^2 Z_i(\omega)^{-1}/m_i$ are the uncoupled, radiative corrected polarizabilities of each dipole defined in Eqn. (3.13). Implementing these terms into our expressions for the absorbed and scattered power and dividing by the magnitude of the time averaged Poynting vector for planewave light, we find

$$\sigma_{\mathrm{abs}}(\omega) = \frac{4\pi\omega^2}{c}\left[(m_1/e^2)\gamma_{1,\mathrm{abs}}|\tilde{\alpha}_1(\omega)|^2 + (m_2/e^2)\gamma_{2,\mathrm{abs}}|\tilde{\alpha}_2(\omega)|^2\right] \tag{4.21}$$

$$\sigma_{\mathrm{sca}}(\omega) = \frac{8\pi}{3}k^4\left[|\tilde{\alpha}_1(\omega)|^2 + |\tilde{\alpha}_2(\omega)|^2\right] + 8\pi k|\tilde{\alpha}_1(\omega)||\tilde{\alpha}_2(\omega)|\mathrm{Im}\{g\} \tag{4.22}$$

$$\sigma_{\mathrm{ext}}(\omega) = \sigma_{\mathrm{abs}}(\omega) + \sigma_{\mathrm{sca}}(\omega). \tag{4.23}$$

Importantly, we see the emergence of an interference term in the scattering cross section of the two coupled dipolar surface modes, which can constructively or destructively interfere. The nature of this interference is be dictated by the imaginary part of the coupling term g, which has a complicated dependence on the oscillation frequency, the particle separation, and the relative orientation of the the two coupled dipoles, as illustrated in Fig. 4.2.

4.2 *The Inelastic Scattering Probability for Two Electromagnetically Coupled Dipoles*

4.2.1 *A Classical Approach*

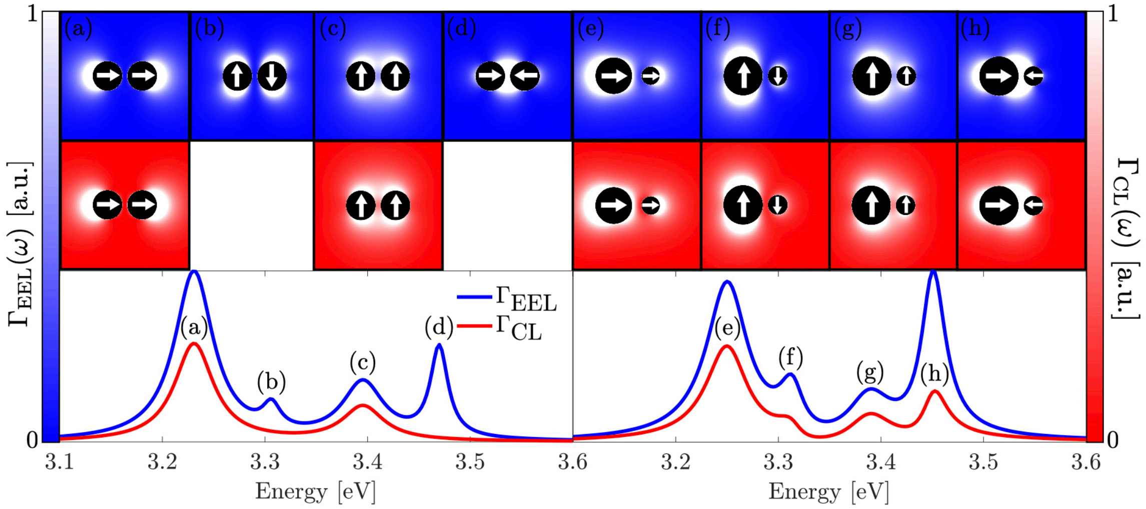

Figure 4.3: Inelastic scattering spectra, and spectrum images of the total loss probability $\Gamma_{\rm EEL}$ (blue) and and the radiative contribution $\Gamma_{\rm CL}$ (red) for a pair of Ag spheres. We examine the case of a homodimer (left) with sphere radii $a_1 = a_2 = 15$ nm, and a inter-surface separation of 5 nm, and a heterodimer (right), where $a_1 = 20$ nm, $a_2 = 10$ nm. In the case of the homodimer, we see that there are no peaks in $\Gamma_{\rm CL}$ for the out-of-phase oscillations of the surface modes due to total destructive interference in far field radiation. At normal mode energies (a) and (e), we observe a colinear in-phase oscillation →→, and a resulting nodal region between the surface modes. At energies (b) and (f) we observe an anti-parallel out-of-phase oscillation ↑↓ at a slightly lower energy than the more intensely radiant parallel in-phase oscillation ↑↑ at energies (c) and (g). Finally, the anti-colinear out-of-phase oscillations →← (d) and (h) reside at the highest energy. With a combination of spectroscopic measurement and spectrum imaging, the inelastic scattering signal is capable of determining the energy and spatial profile for the eigenmodes modes of a simple dimer system or more complicated electromagnetically coupled nanostructures.

From Eqns. 4.7, instead of considering the influence of a planewave, we replace the source of the external field with that of a point charge from an electron, and we write

$$m_1\ddot{\mathbf{u}}_1(t) + m_1\gamma_1\dot{\mathbf{u}}_1(t) + m_1\omega_1^2\mathbf{u_1}(t) - g\mathbf{u}_2(t) = e\mathbf{E}_{\text{el}}(\mathbf{r}_1, t) \tag{4.24}$$

$$m_2\ddot{\mathbf{u}}_2(t) + m_2\gamma_2\dot{\mathbf{u}}_2(t) + m_2\omega_2^2\mathbf{u_2}(t) - g\mathbf{u}_1(t) = e\mathbf{E}_{\text{el}}(\mathbf{r}_2, t). \tag{4.25}$$

After Fourier transforming each of the coupled equations, we immediately produce solutions to the coupled equations of motion in the frequency domain.

$$\mathbf{u}_1(\omega) = \frac{\frac{\mathbf{E}_{\text{el}}(\mathbf{r}_1,\omega)}{e}\alpha_1(\omega) + \frac{g\mathbf{E}_{\text{el}}(\mathbf{r}_2,\omega)}{e^3}\alpha_1(\omega)\alpha_2(\omega)}{1 - \frac{g^2}{e^4}\alpha_1(\omega)\alpha_2(\omega)} \tag{4.26}$$

$$\mathbf{u}_2(\omega) = \frac{\frac{\mathbf{E}_{\text{el}}(\mathbf{r}_2,\omega)}{e}\alpha_2(\omega) + \frac{g\mathbf{E}_{\text{el}}(\mathbf{r}_1,\omega)}{e^3}\alpha_1(\omega)\alpha_2(\omega)}{1 - \frac{g^2}{e^4}\alpha_1(\omega)\alpha_2(\omega)} \tag{4.27}$$

The uncoupled, radiative corrected polarizability terms above are again defined by Eqn. (3.13). Then from Eqn. (3.28), we solve for the inelastic scattering probability of the coupled dipole system. We find

$$\Gamma_{\text{dip-dip}}(\omega) = \frac{1}{\pi\hbar^2}\left[\text{Im}\left\{\mathbf{F}_{\text{el}}(\mathbf{r}_1,\omega)^* \cdot \mathbf{u}_1(\omega)\right\} + \text{Im}\left\{\mathbf{F}_{\text{el}}(\mathbf{r}_2,\omega)^* \cdot \mathbf{u}_2(\omega)\right\}\right], \tag{4.28}$$

where the spectral representation of the force of the electron on the dipoles $\mathbf{F}_{\text{el}}(\mathbf{r}_i,\omega) = e\mathbf{E}_{\text{el}}(\mathbf{r}_i,\omega)$, is defined by Eqn. (3.23).

4.2.2 Cathodoluminescence of Coupled-Radiating Dipoles

To isolate the radiative contribution to the inelastic scattering, we consider the energy radiated across a spherical boundary, over an arbitrary time period τ, for which we write

$$\begin{aligned} \langle \Delta E \rangle &= \frac{1}{\tau}\int_0^\tau dt \int d\Omega \; r^2 \mathbf{S}(\mathbf{x},t)\cdot\hat{\mathbf{r}} \\ &= \int d\Omega \; r^2 \langle \mathbf{S}(\mathbf{x},t)\rangle \cdot \hat{\mathbf{r}} \qquad (4.29) \\ &= \int_0^\infty d(\hbar\omega) \; \hbar\omega \Gamma_{\mathrm{CL}}(\omega). \end{aligned}$$

Above, $\langle \mathbf{S}(\mathbf{x},t)\rangle = c[\mathbf{E}_1(\mathbf{x},t) + \mathbf{E}_2(\mathbf{x}_2,t)] \times [\mathbf{B}_1(\mathbf{x},t) + \mathbf{B}_2(\mathbf{x},t)]^*/8\pi$ is the time averaged Poynting vector for two radiating sources, and $\mathbf{E}_i$, $\mathbf{B}_i$ are their associated electric and magnetic far-fields. In turn, these fields can be expressed in terms of the coupled dipolar coordinates in the frequency domain as

$$r\mathbf{E}_i(\mathbf{r}_i,\omega) = ek^2[(\hat{\mathbf{r}} \times \mathbf{u}_i(\omega)) \times \hat{\mathbf{r}}]e^{ikr_i} \qquad (4.30)$$

$$r\mathbf{B}_i^*(\mathbf{r}_i,\omega) = ek^2[(\hat{\mathbf{r}} \times \mathbf{u}_i^*(\omega)) \times \hat{\mathbf{r}}]e^{-ikr_i}. \qquad (4.31)$$

With Eqn. (4.29), we then solve for the contribution to the inelastic scattering signal due to radiative losses

$$\Gamma_{\mathrm{CL}}(\omega) = \frac{2e^2}{3\pi\hbar^2}k^3 \left|\mathbf{u}_1(\omega) + \mathbf{u}_2(\omega)\right|^2, \qquad (4.32)$$

where the effects due to coupling are embedded in the definition of the dipolar coordinates in Eqns. (4.26) and (4.27). The modulus square of the sum of the two coupled oscillator coordinates introduces an interference term in the far-field scattering measurement inherent to CL. In Fig. 4.3 we see that the out-of-phase oscillation between the coupled surface modes leads to total destructive interference in far field scattering in the case of the homodimer.

4.2.3 Normal Mode Analysis, and a Quantum Mechanical Approach

Moving to a cartesian coordinate system, and constructing a system Hamiltonian for our two electromagnetically coupled dipoles from Eqns. (2.86) and (2.91), we find

$$H = \frac{\mathbf{p}_1^2}{2m_1} + \frac{\mathbf{p}_2^2}{2m_2} + \frac{1}{2}m_1\omega_1^2\mathbf{u}_1^2 + \frac{1}{2}m_2\omega_2^2\mathbf{u}_2^2 - \mathbf{u}_1 \cdot \mathbf{\Lambda}(\mathbf{r}) \cdot \mathbf{u}_2, \tag{4.33}$$

where $\mathbf{\Lambda}(\mathbf{r}) = e^2(3\hat{\mathbf{r}}\hat{\mathbf{r}} - 1)/r^3$ in the quasistatic limit, and only the near field term of the dipole relay tensor contributes to the inter-dipole coupling, where $r = |\mathbf{r}_1 - \mathbf{r}_2|$. We begin by a re-scaling of operators x_i and p_i defining the dimensionless parameters $M_+ = (m1/m2)^{1/4}$, and $M_- = (m2/m1)^{1/4}$

$$\begin{aligned}
\begin{pmatrix} p_1 \\ p_2 \end{pmatrix} &= \begin{pmatrix} M_+ & 0 \\ 0 & M_- \end{pmatrix} \begin{pmatrix} p_1' \\ p_2' \end{pmatrix} \\
\begin{pmatrix} u_1 \\ u_2 \end{pmatrix} &= \begin{pmatrix} M_- & 0 \\ 0 & M_+ \end{pmatrix} \begin{pmatrix} u_1' \\ u_2' \end{pmatrix},
\end{aligned} \tag{4.34}$$

which yields an expression for the Hamiltonian with a common geometric mass $m = \sqrt{m_1 m_2}$, for oscillator 1 and 2, as

$$H = \frac{\mathbf{p}_1'^2}{2m} + \frac{\mathbf{p}_2'^2}{2m} + \frac{1}{2}m\omega_1^2\mathbf{u}_1'^2 + \frac{1}{2}m\omega_2^2\mathbf{u}_2'^2 - \mathbf{u}_1' \cdot \mathbf{\Lambda}(\mathbf{r}) \cdot \mathbf{u}_2' \tag{4.35}$$

The ladder operators are related to the position and momentum operators by

$$\begin{aligned}
a_{12} &= \sqrt{\frac{m\omega_{12}}{2\hbar}} \left(\hat{u}_{12}' + i\frac{\hat{p}_{12}'}{m\omega_{12}} \right) \\
a_{12}^\dagger &= \sqrt{\frac{m\omega_{12}}{2\hbar}} \left(\hat{u}_{12}' - i\frac{\hat{p}_{12}'}{m\omega_{12}} \right),
\end{aligned} \tag{4.36}$$

and the position and momentum operators may then be defined in terms of $a_{12}, a_{12}^\dagger$ as:

$$\begin{aligned}\hat{u}'_{12} &= \sqrt{\frac{\hbar}{2m\omega_{12}}}\left(a_{12}^\dagger + a_{12}\right)\\ \hat{p}'_{12} &= i\sqrt{\frac{\hbar m\omega_{12}}{2}}\left(a_{12}^\dagger - a_{12}\right).\end{aligned} \tag{4.37}$$

We now diagonalize our Hamiltonian via a unitary transformation. Utilizing the Baker-Campbell-Haussdorff formula

$$\begin{aligned}e^{-S}H_0e^{S} &= \sum_{n=0}^{\infty}\frac{[H,(S)^n]}{n!}\\ &= \tilde{H}_0\end{aligned} \tag{4.38}$$

and defining the generating function $S = i\phi(x'_1p'_2 - x'_2p'_1)/\hbar$, we transform our Hamiltonian into a normal mode basis, writing

$$\tilde{H}_0 = \frac{\mathbf{p}_+^2}{2m} + \frac{\mathbf{p}_-^2}{2m} + \frac{1}{2}m\omega_+^2\mathbf{u}_+^2 + \frac{1}{2}m\omega_-^2\mathbf{u}_-^2, \tag{4.39}$$

where the operators in the ±-basis are related to the operators in the $1,2$-basis via the rotation matrix in terms of the coupling angle ϕ

$$\begin{aligned}\begin{pmatrix}p'_1\\ p'_2\end{pmatrix} &= \begin{pmatrix}\cos\phi_\lambda & -\sin\phi_\lambda\\ \sin\phi_\lambda & \cos\phi_\lambda\end{pmatrix}\begin{pmatrix}p_+\\ p_-\end{pmatrix}\\ \begin{pmatrix}u'_1\\ u'_2\end{pmatrix} &= \begin{pmatrix}\cos\phi_\lambda & -\sin\phi_\lambda\\ \sin\phi_\lambda & \cos\phi_\lambda\end{pmatrix}\begin{pmatrix}u_+\\ u_-\end{pmatrix}\end{aligned}\quad. \tag{4.40}$$

Explicitly, the normal mode momentum and position operators are defined as

$$\mathbf{u}_{\pm} = \sum_{\lambda} \hat{\mathbf{n}}_{\pm}^{\lambda} u_{\pm}^{\lambda} \tag{4.41}$$

$$\mathbf{p}_{\pm} = \sum_{\lambda} \hat{\mathbf{n}}_{\pm}^{\lambda} p_{\pm}^{\lambda}, \tag{4.42}$$

where the scalar terms of the normal mode operators are defined by

$$u_{+}^{\lambda} = u'_{1,\lambda} \cos\phi_{\lambda} + u'_{2,\lambda} \sin\phi_{\lambda} \tag{4.43}$$

$$u_{-}^{\lambda} = -u'_{1,\lambda} \sin\phi_{\lambda} + u'_{2,\lambda} \cos\phi_{\lambda} \tag{4.44}$$

$$p_{+}^{\lambda} = p'_{1,\lambda} \cos\phi_{\lambda} + p'_{2,\lambda} \sin\phi_{\lambda} \tag{4.45}$$

$$p_{-}^{\lambda} = -p'_{1,\lambda} \sin\phi_{\lambda} + p'_{2,\lambda} \cos\phi_{\lambda} \tag{4.46}$$

We define the coupling angle and the normal mode frequencies as

$$\begin{aligned}
\phi_{\lambda} &= \frac{1}{2}\tan^{-1}\left(\frac{2g_{\lambda}}{m[\omega_2^2 - \omega_1^2]}\right) \\
\omega_{+}^{\lambda} &= \left[\omega_1^2 \cos^2\phi_{\lambda} + \omega_2^2 \sin^2\phi_{\lambda} - \frac{g_{\lambda}}{m} \sin\phi_{\lambda}\cos\phi_{\lambda}\right]^{\frac{1}{2}} \qquad (4.47) \\
\omega_{-}^{\lambda} &= \left[\omega_1^2 \sin^2\phi_{\lambda} + \omega_2^2 \cos^2\phi_{\lambda} + \frac{g_{\lambda}}{m} \sin\phi_{\lambda}\cos\phi_{\lambda}\right]^{\frac{1}{2}},
\end{aligned}$$

where $\lambda = x, y, z$ indicates components of the dipole's orientation in Cartesian coordinates. If we choose a dipole separation along the x-axis, we define the components of the coupling parameter g^λ as

$$g^x = \frac{2e^2}{r^3} \tag{4.48}$$

$$g^{yz} = -\frac{e^2}{r^3}. \tag{4.49}$$

As in the previous case of a single particle, we introduce a time dependent perturbative term to our Hamiltonian.

$$\tilde{H} = \tilde{H}_0 + V, \tag{4.50}$$

where $V = -\mathbf{u}_1 \cdot \mathbf{F}(\mathbf{r}_1, t) - \mathbf{u}_2 \cdot \mathbf{F}(\mathbf{r}_2, t)$. From Eqn. (2.80) considering only the generalized force acting on the $\ell = 1$ surface modes due to a traveling point charge with charge distribution $\rho(\mathbf{x}, t) = e\delta(\mathbf{R} - \mathbf{R}_0)\delta(z - vt)$, we find

$$\mathbf{F}(\mathbf{r}_1, t) = -e\frac{a_1\hat{\mathbf{x}} + b_1\hat{\mathbf{y}} + (vt)\hat{\mathbf{z}}}{[a_1^2 + b_1^2 + (vt)^2]^{\frac{3}{2}}} \tag{4.51}$$

$$\mathbf{F}(\mathbf{r}_2, t) = -e\frac{a_2\hat{\mathbf{x}} + b_2\hat{\mathbf{y}} + (vt)\hat{\mathbf{z}}}{[a_2^2 + b_2^2 + (vt)^2]^{\frac{3}{2}}}. \tag{4.52}$$

In the normal mode basis, the perturbative term becomes

$$V = -\mathbf{u}_+ \cdot \mathbf{F}_+(t) - \mathbf{u}_- \cdot \mathbf{F}_-(t), \tag{4.53}$$

where we define the normal mode forces as

$$\mathbf{F}_+(t) = \mathbf{F}(\mathbf{r}_1, t)M_- \cos\phi_\lambda + \mathbf{F}(\mathbf{r}_2, t)M_+ \sin\phi_\lambda \tag{4.54}$$

$$\mathbf{F}_-(t) = -\mathbf{F}(\mathbf{r}_1, t)M_- \sin\phi_\lambda + \mathbf{F}(\mathbf{r}_2, t)M_+ \cos\phi_\lambda. \tag{4.55}$$

Again, moving into the interaction picture, and expanding the Dyson series to first order, we evaluate the probability amplitude to find the system in an excited state in the normal mode basis

$$\left\langle n'_+ n'_- \middle| \tilde{\psi}(t) \right\rangle = \frac{1}{i\hbar} \int_{-\infty}^{t} dt' \left\langle n'_+ n'_- \right| - \mathbf{u}_+(t) \cdot \mathbf{F}_+(t) - \mathbf{u}_-(t) \cdot \mathbf{F}_-(t) \left| n_+ n_- \right\rangle . \tag{4.56}$$

In a manner analogous to the single particle case, we find the scattering probability in the normal mode basis to be

$$\begin{aligned} \Gamma_{\text{dip-dip}}(\omega) = {} & \frac{1}{e^2 \pi \hbar^2} \sum_{\lambda} \left[|F_+^{\lambda}(\omega)|^2 \mathrm{Im}\{\alpha_+^{\lambda}(\omega)\} \right] \left([n_+^{\lambda} + 1] \delta_{n_+^{\lambda}, n_+^{\lambda}+1} + n_+^{\lambda} \delta_{n_+^{\lambda}, n_+^{\lambda}-1} \right) \\ & + \frac{1}{e^2 \pi \hbar^2} \sum_{\lambda} \left[|F_-^{\lambda}(\omega)|^2 \mathrm{Im}\{\alpha_-^{\lambda}(\omega)\} \right] \left([n_-^{\lambda} + 1] \delta_{n_-^{\lambda}, n_-^{\lambda}+1} + n_-^{\lambda} \delta_{n_-^{\lambda}, n_-^{\lambda}-1} \right) , \end{aligned} \tag{4.57}$$

where the normal mode polarizabilities are defined as

$$\alpha_+^{\lambda}(\omega) = \frac{e^2}{m} \frac{1}{(\omega_+^{\lambda})^2 - \omega^2 - i\gamma\omega} \tag{4.58}$$

$$\alpha_-^{\lambda}(\omega) = \frac{e^2}{m} \frac{1}{(\omega_-^{\lambda})^2 - \omega^2 - i\gamma\omega} . \tag{4.59}$$

The terms $n_\pm^{\lambda}$ are the occupation numbers of the symmetric (+) and antisymmetric (−) modes of the coupled oscillators, the value of which, at finite system temperature, is determined by the Bose-Einstein distribution, where $n_+^{\lambda} = n_-^{\lambda}$ when the system is at a uniform temperature.

4.3 Coupling Between the Surface Modes of a Slab and a Dipole Mode on a Sphere

Reproduced with permission from:

- Beutler, Elliot K., Maureen J. Lagos, and David J. Masiello. ”Infrared surface phonon nanospectroscopy of an interacting dielectric-particle–dielectric-substrate dimer using fast electrons.” Physical Review B 103, no. 16 (2021): 165418 [2].

Recent advances in electron microscopy have led to dramtic improvements in atomic scale spatial imaging and spectroscopic resolution of inelastic scattering processes. This is due to improvements in monochromation and aberration correction of the incident electron beam [46, 50, 45, 51, 52, 53]. These developements have layed ground for a detailed examination of progessively lower energy nanoscale excitations, such as the molecular vibrations of organic and biological compounds [54, 55], as well as surface and bulk phonons hosted by macroscopic samples, thin films, individual nanoparticles, and nanoparticle assemblies of varying morphology, none of which had been previously characterized by electron energy loss spectroscopy (EELS) [56, 57, 58, 59, 60, 48, 61]. Unlike a plane wave light source, a uniformly moving electron carries an evanescent field akin to the broad spectrum white light source produced by synchrotron radiation. When utilized as a spectroscopic probe, it is capable of characterizing target excitations across a broad spectral range, from low energy collective surface and bulk resonances to valence electronic transitions to core-loss events at high energy. As the available spectroscopic window of the electron microscope has extended ever lower in energy, now down to thermal energies ($\sim$ 25 meV), the vibrational modes probed by the electron beam on individual nanoparticles become apparent [50, 62, 63, 57]. In this regime, dielectric nanoparticles and their planar dielectric substrates may be co-resonant. When placed in proximity, independent nanoparticle and substrate excitations are able to appreciably couple in the near-field, and it is the composite nanoparticle-substrate assembly that is ultimately interrogated by the electron beam. The consequences of such phonon mode hybridization may be perceptible through inelastic electron scattering, producing a

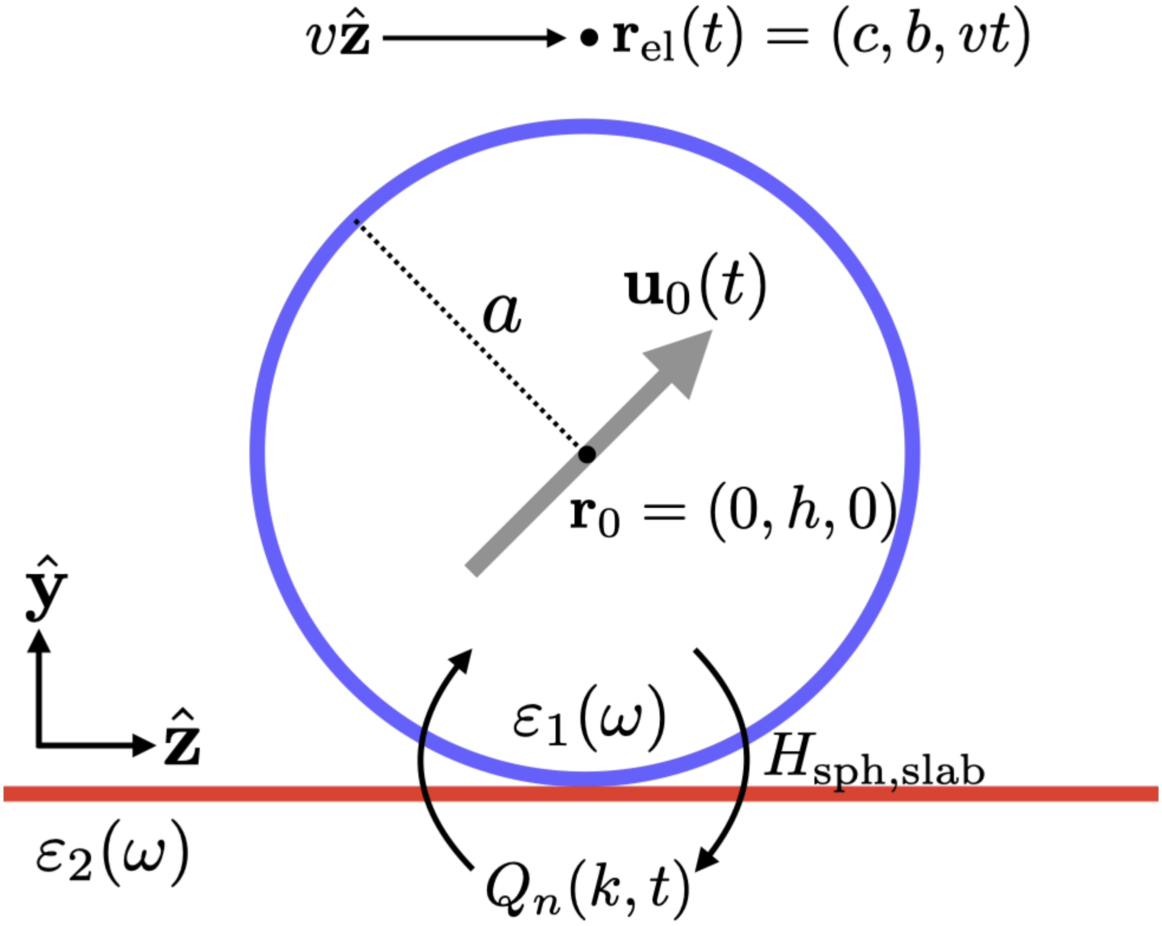

Figure 4.4: Schematic of the composite sphere-slab dielectric system in the presence of a uniformly moving electron. Relevant parameters including the sphere radius a, the position of the electron $\mathbf{r}_{\rm el}(t)$, and the time-dependent LSPh coordinate of the sphere $\mathbf{u}_0$ at a fixed position $\mathbf{r}_0$ are defined, along with the generalized coordinate of the substrate surface response $Q_n(k, t)$ and the energy of interaction $H_{\rm sph,slab}$. When the sphere rests directly on top of the slab, the height $h = a$.

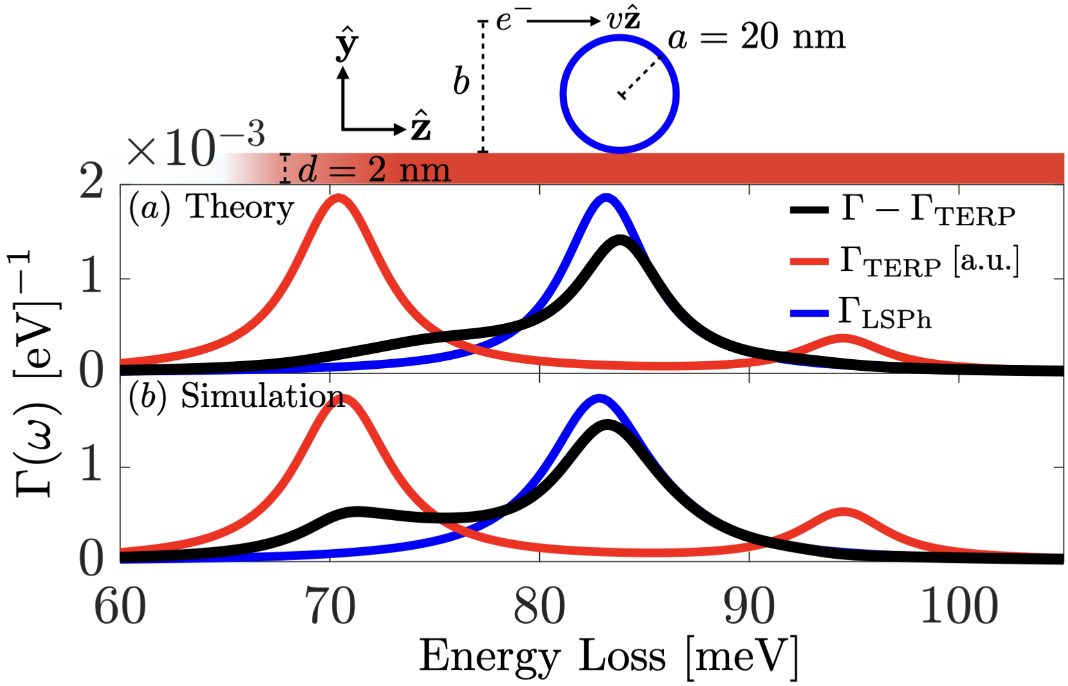

Figure 4.5: Comparison of (a) Eq. (4.73) to (b) simulation for the monomers (free space sphere and slab), and the dimer (composite sphere-slab system) after background subtraction. For the simulated composite system, the numerical scattering probability for a $d = 2$ nm dielectric slab is subtracted from the result for a composite $a = 20$ nm sphere positioned on top of a slab of identical dimensions. A Lorentz oscillator dielectric function parametrized to the bulk response of MgO is used to describe the material responses of the sphere and slab. The electron beam height is $b = 3a$, traveling uniformly with 10 keV of kinetic energy, and the location of the charge distributions are defined by $\mathbf{r}_0 = (0, a, 0)$ and $\mathbf{r}_{\mathrm{el}} = (0, b, vt)$ for the sphere and probe, respectively. In both simulation and theory Γ_{TERP} is normalized to Γ_{LSPh}.

rich and nuanced spectrum deserving of an in-depth analysis. Previous work [64, 65] has explored substrate effects in electron scattering measurements of nanoparticle targets, particularly how their presence can renormalize the eigenfrequencies of the target's excited surface modes. Others have investigated the potential for energy transfer facilitated by the spectral overlap of a nanoparticle's surface mode resonances with the band gap energies of its supporting semiconductor substrate, an adsorbate molecule, or an adjacent nanoparticle [66, 67, 68, 69, 70, 71, 72].

In this section, we present a theoretical model-based approach to interpreting the measured scattering probability of a composite dielectric nanoparticle-substrate “dimer” system for a ’grazing’ electron beam geometry, showcasing that a consideration of only the nanoparticle’s renormalized eigenmodes is insufficient in interpreting the resulting scattering signal when both the sample and substrate materials are dispersive in the same spectral region. For simplicity, we will consider a spherical nanoparticle target positioned directly adjacent to the surface of a dielectric slab, where both the particle and slab host nearly co-resonant surface mode responses in the infrared. We then investigate the resulting interaction between the electron probe, nanoparticle, and slab encoded in the spectrum of the scattered electron beam.

We begin by working within a classical dielectric formalism, and construct a system Hamiltonian after defining time-dependent coordinates for the oscillatory surface modes of both the sphere and substrate. This allows for a characterization of the energies of interaction and associated forces between the electron probe, nanoparticle, and substrate at the level of the equations of motion. We then examine the linear response of the dielectric sphere, deriving its effective polarizability in the presence of a substrate of varying depth, by solving the coupled equations of motion in Fourier space. Correspondingly, we also derive the linear response of the semi-infinite dielectric slab in the presence of the sphere. This permits an exploration of how the system evolves in response to an external perturbing field when the distance between the sphere and substrate surface is altered, and when the thickness of the supporting substrate is varied. The near-field interactions between the surface modes on the sphere and substrate are visualized with the aid of induced electric near-field profiles, simulated using plane-wave excitation with specific polarization. Finally, we derive an expression of the sphere-substrate dimer’s corresponding scattering probability for a dielectric slab of varying thickness, and compare the results to a simulated electron scattering experiment based on numerical solution of Maxwell’s equations. In both cases, we consider an aloof ‘grazing’ trajectory, with the path of the electron beam oriented parallel to the thin film surface and traveling entirely in vacuum, avoiding the excitation of bulk phonon mode resonances [61]. Excellent agreement between simulations and the developed model highlights the importance of the substrate (which we henceforth refer to more generally as a dielectric slab) as a separate dynamical component that can strongly modify the infrared responses of the nanoparticle target.

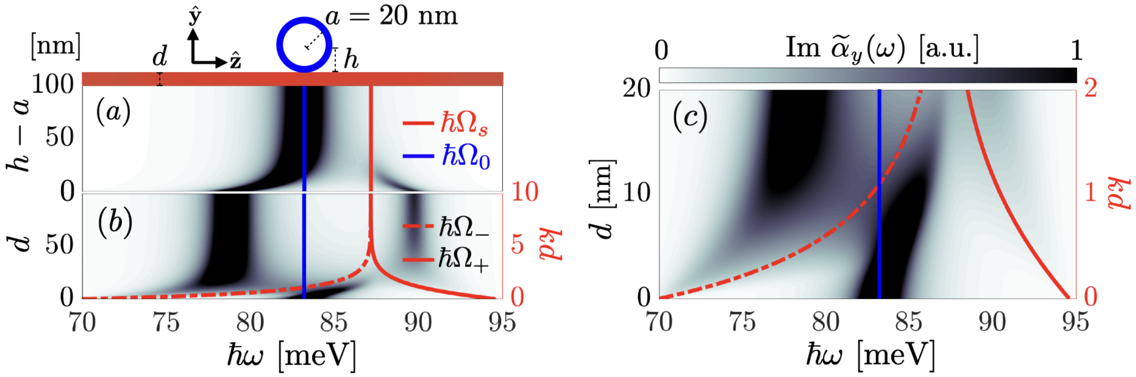

Figure 4.6: Evolution of Im $\widetilde{\alpha}_y(\omega)$ for an $a = 20$ nm sphere when the sphere height (h) and the slab depth (d) are varied. The dielectric response of the sphere and slab are defined by a common Lorentz oscillator dielectric function (i.e., $\widetilde{\varepsilon}_1(\omega) = \widetilde{\varepsilon}_2(\omega)$), parametrized to the bulk response of MgO. In panel (a), the sphere is 'moon-landed' onto a 100 nm thick slab from an initial distance of 100 nm between the sphere and the slab surfaces. In panel (b), the depth of the slab is decreased from $d = 100$ nm to 0 nm, and the FK$_\pm$ ($\hbar\Omega_\pm$) modes are allowed to evolve as kd is varied. Ω_0 is the $\ell = 1$ eigenfrequency of the free-space sphere (blue line) and Ω_s is the eigenfrequency of the free-space semi-infinite slab (red curves). Panel (c) provides a closer examination of the mixed surface mode responses in the region of $0 \leq d \leq a$. We observe that as the slab depth becomes increasingly small, the normal mode responses resolve to the free-space eigenfrequencies.

From Eqns. (2.86) and (2.87) the Hamiltonian for the sphere and the slab respectively, we can define the total system Hamiltonian in the presence of an electron as

$$H = H^0_{\text{el}} + H^0_{\text{sph}} + H^0_{\text{slab}} + H_{\text{el,sph}} + H_{\text{el,slab}} + H_{\text{sph,slab}}. \tag{4.60}$$

The term H^0_{el} is the kinetic energy of the electron probe with charge density $\rho_{\text{el}}(\mathbf{x}, t) = -e\delta(\mathbf{x} - \mathbf{r}_{\text{el}}(t))$, while the terms H^0_{sph} and H^0_{slab} account for the internal energies of the sphere and dielectric slab. $H_{\text{el,sph}}$ and $H_{\text{el,slab}}$ represent the energies of interaction between the electron and the dielectrics, while $H_{\text{sph,slab}}$ represents the energy of interaction between the dielectric bodies. For simplicity, we restrict the response of the sphere to the lowest order $\ell = 1$ dipole mode and move from the spherical-multipole basis to Cartesian coordinates.

The vector $\mathbf{u}_0(t)$ defines the LSPh coordinate with natural frequency ω_0, effective mass m_0, and charge distribution $\rho_0(\mathbf{x}, t) = -e\mathbf{u}_0(t) \cdot \nabla\delta(\mathbf{x} - \mathbf{r}_0)$. Hamiltonians for the individual dielectrics are defined from Eq. (4.60) as

$$\begin{aligned} H_{\text{sph}} &= H^0_{\text{sph}} + H_{\text{el,sph}} + H_{\text{sph,slab}} \\ &= \frac{\mathbf{p}_0^2}{2m_0} + \frac{1}{2}m_0\omega_0^2\mathbf{u}_0^2 - \mathbf{u}_0 \cdot \mathbf{F}_{\text{el}} + \int d\mathbf{x}\ \rho_0(\mathbf{x}, t)\Phi_{\text{slab}}(\mathbf{x}, t) \end{aligned} \tag{4.61}$$

$$\begin{aligned} H_{\text{slab}} &= H^0_{\text{slab}} + H_{\text{el,slab}} + H_{\text{sph,slab}} \\ &= \sum_{n=-\infty}^{\infty} \int_0^\infty dk \left[\frac{P_n P_n^*}{m_k} + m_k\omega_s^2 Q_n Q_n^* - \left(F^*_{\text{el},n} Q_n + F_{\text{el},n} Q_n^*\right)\right] + \int d\mathbf{x}\ \rho_0(\mathbf{x}, t)\Phi_{\text{slab}}(\mathbf{x}, t), \end{aligned} \tag{4.62}$$

where the energy of interaction between the LSPh and semi-infinite slab is calculated by integration of ρ_0 with Φ_{slab}. In the presence of both a traveling electron and a oscillating dipolar charge distribution the slab potential is calculated from the slab's induced Green's function. For aloof electron trajectories, we consider Eqn. 2.73, where $\rho = \rho_{\text{el}} + \rho_0$. From Hamilton's equations

$$\dot{\mathbf{u}}_0 = \frac{\partial H}{\partial \mathbf{p}_0} \tag{4.63}$$

$$\dot{\mathbf{p}}_0 = -\frac{\partial H}{\partial \mathbf{u}_0}, \tag{4.64}$$

applied to Eqn. (4.61), and followed by a Fourier transform from time to frequency, we find the Fourier amplitudes for the dipolar surface mode response in the presence of the slab of finite depth. For the particular case where the locations of the charge distributions are defined as $\mathbf{r}_{\text{el}}(t) = (0, b, vt)$ and $\mathbf{r}_0 = (0, a, 0)$ and the electron travels directly over of the center of the sphere, we find

$$u_z(\omega) = \frac{\alpha_z(\omega)}{e^2}\left[F_{\mathrm{el},z}(\mathbf{r}_0,\omega) + \int_0^\infty dk\bar{F}_{k,z}(\mathbf{r}_0,\omega)\zeta(k,\omega))\right] \tag{4.65}$$

$$u_y(\omega) = \frac{\alpha_y(\omega)}{e^2}\left[F_{\mathrm{el},y}(\mathbf{r}_0,\omega) + \int_0^\infty dk\bar{F}_{k,y}(\mathbf{r}_0,\omega)\zeta(k,\omega))\right], \tag{4.66}$$

where the terms α_{yz} are the modified polarizabilities of the dipolar modes of the sphere perpendicular and parallel to the slab surface, respectively. These polarizabilities, dressed by the presence of the slab of varying depth are

$$\alpha_{xz}(\omega) = \left[\alpha_{\mathrm{nr}}(\omega)^{-1} - \frac{1}{2}\int_0^\infty dk\ k^2 e^{-2kh}\zeta(k,\omega)\right] \tag{4.67}$$

$$\alpha_y(\omega) = \left[\alpha_{\mathrm{nr}}(\omega)^{-1} - \int_0^\infty dk\ k^2 e^{-2kh}\zeta(k,\omega)\right]. \tag{4.68}$$

Features of the slab dressed polarizability α_y are explored in Fig. 4.6 under both the case of varying slab depth d and sphere height above the slab h. In each of these cases, we see that the imaginary part of α_y returns to the value of the bare eigenfrequencies of the slab's Fuchs-Kliewer modes, and the sphere's dipolar Fröhlich mode [73]. The terms $F_{\mathrm{el},z}$ and $F_{\mathrm{el},y}$ represent yz-components of the force contributed by the fast electron, while the terms $\bar{F}_{\mathrm{k},z}$ and $\bar{F}_{\mathrm{k},y}$ integrated against the surface response function of the slab, represent the force contributed by the electron's wake potential [74] generated by the presence of the dielectric slab, and they are proportional to the Fourier transform of Bessel functions $J_0(kvt)$ and

$J_1(kvt)$. Explicitly, we write

$$F_{\mathrm{el},y}(\mathbf{r}_0,\omega) = \frac{b-h}{R}\frac{2e^2|\omega|}{v^2}K_1\left(\frac{|\omega|R}{v}\right) \tag{4.69}$$

$$F_{\mathrm{el},z}(\mathbf{r}_0,\omega) = \frac{2e^2\omega}{v^2}iK_0\left(\frac{|\omega|R}{v}\right) \tag{4.70}$$

$$\bar{F}_{k,z}(\mathbf{r}_0,\omega) = -i\frac{2e^2\omega}{v^2}\frac{e^{-k(b+h)}}{\sqrt{k^2-\left(\frac{\omega}{v}\right)^2}} \quad \text{for} \quad k \geq \frac{|\omega|}{v} \tag{4.71}$$

$$\bar{F}_{k,y}(\mathbf{r}_0,\omega) = \frac{2e^2}{v}\frac{k\ e^{-k(b+h)}}{\sqrt{k^2-\left(\frac{\omega}{v}\right)^2}} \quad \text{for} \quad k \geq \frac{|\omega|}{v}. \tag{4.72}$$

To calculate the inelastic scattering probability, we refer to Eqn. (3.32), where for the electron charge distribution, we again call upon Eqn. (3.33), and consider the contribution to the induced potential from both the sphere and the slab, yielding

$$\Gamma(\omega) = \lim_{z_0\to\infty}\frac{2z_0}{\pi}\left(\frac{e}{\hbar v}\right)^2\int_{\omega/v}^{\infty}dk\frac{e^{-2kb}}{\sqrt{k^2-\left(\frac{\omega}{v}\right)^2}}\mathrm{Im}\left\{\zeta(k,\omega)\right\}$$
$$(4.73)$$
$$+\frac{1}{\pi\hbar^2}\mathrm{Im}\left\{\mathbf{u}_0(\omega)\cdot\left[\mathbf{F}_{\mathrm{el}}(\mathbf{r}_0,\omega)+\int_0^{\infty}dk\ \zeta^*(k,\omega)\bar{\mathbf{F}}_k(\mathbf{r}_0,\omega)\right]^*\right\}.$$

We observe that the first term of Eqn. (4.73) is trivally related to the inelastic scattering rate of an ion off of a finite slab in Eqn. (3.42). The term z_0 is the path length of the probing electron. This result is expected due to the principle of superposition of the induced electric and scalar fields. The second term includes the effects of mode mixing between the surface modes of the sphere and the finite slab. Therefore, the first term can be interpreted as "background", and subtracted to produce Fig. 4.5, where we make a comparison between our theory and a fully retarded numerical electrodynamic simulation using the electron driven discrete dipole approximation, with an electron source (e-DDA) [75, 76].

4.4 Nanometer-Scale Spatial and Spectral Mapping of Exciton Polaritons in Structured Plasmonic Cavities

Reproduced with permission from:

- Bourgeois, Marc R., Elliot K. Beutler, Siamak Khorasani, Nicole Panek, and David J. Masiello. "Nanometer-Scale Spatial and Spectral Mapping of Exciton Polaritons in Structured Plasmonic Cavities." Physical Review Letters 128, no. 19 (2022): 197401. [1]

Exciton polaritons (EPs) are a type of hybrid light-matter coupled quasiparticles which form as a consequence of strong coupling between an optical cavity mode with a system of quantum emitters, which have garnered interest due to their potential application in modifying chemical reaction dynamics and also due to their long-range transport properties. Advancing research in the areas of material science, chemistry, and nanophotonics have explored an expansive catalogue of cavity architectures, including the LSP modes inherent to metallic nanoparticles in the optical regime. The induced electric fields of LSPs exhibit strong spatial variation, leading to position-dependent exciton-cavity coupling strengths between a localized surface resonance and a surrounding excitonic medium. When extended into a periodic array, plasmonic nanoparticles host tunable lattice plasmon polaritons (LLPs), which arise due to hybridization of LSPs within the array, resulting diffractive photonic modes. In contrast to the singular LSP excitations of an isolated metallic nanoparticle, LLPs exhibit strong energy-momentum dispersion characteristics due to the diffractive light-like component of the hybrid lattice modes. In either case, the resulting nanoscale spatial variation of the cavity-emitter coupling strength has led to difficulties in spatially mapping the resulting plasmon-exciton excitation. Recent advances in energy monochromation and aberration correction in scanning transmission microscopes (STEMs) have paved the way for performing a spatial mapping of plasmon mediated EPs on their natural energy and length scales using inelastic scattering spectroscopy techniques (EELS).

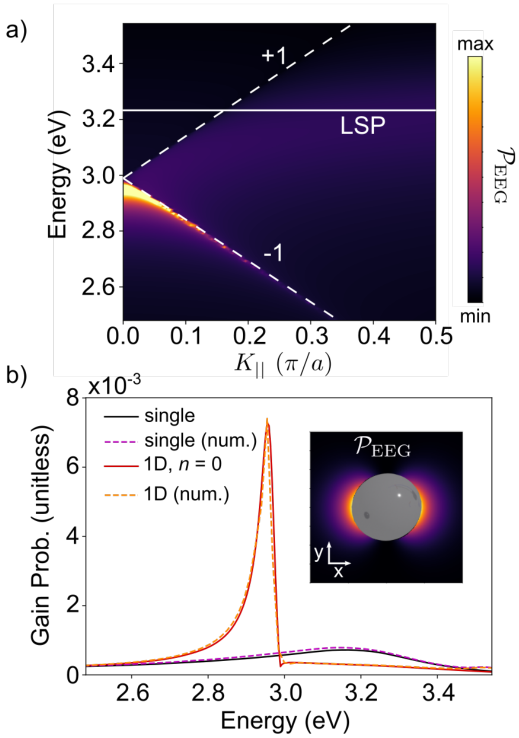

Figure 4.7: (a) Analytic LEEG probability spectra and dispersion diagram for a Ag NP array, as a function of the parallel wavevector component $q_{||}$, with a comparison to the dispersionless single particle LEEG probability. b Comparison of the analytical and numerical evaluation of the LEEG spectrum for a single particle and the one dimensional array. The figure inset shows a spatial map of the probability at the LPP energy around a particle contained within a single unit cell. The incident electron speed is $v = 0.7c$ with an impact parameter of 5 nm from the particle surface. The incident field intensity is $I_0 = 10^9$ W/cm^2

In this section we will demonstrate that laser-stimulated lattice electron energy gain spectroscopy (LEEGS) is well suited to the task of spatially mapping EP in the case of an array of metallic nanoparticles supporting LPPs embedded in an excitonic medium with numerical calculations. Additionally, we establish, based on an analytic analysis of the relativistic LEEG probability, that a laser stimulated inelastic scattering measurement can probe LPP modes with high momentum, energy and spatial resolution in the absence of coupling to a excitonic medium. We accomplish working with the dipole approximation. This limitation is suitable for modeling the resulting plasmon assisted LPP, due to the size of the unit cell of the periodic array which we will consider, in a region where dipole-dipole coupling dominates. Within the dipole approximation in a vacuum environment, the induced electric dipole moment $\mathbf{p}_j$ at position $\mathbf{r}_j$ with the lattice is determined by solving the system of equations

$$\boldsymbol{\alpha}^{-1}(\omega) \cdot \mathbf{p}_j = \mathbf{E}_0(\mathbf{r}_j, \omega) + \sum_{\ell \neq j} \boldsymbol{\Lambda}(\mathbf{r}_j, \mathbf{r}_\ell) \cdot \mathbf{p}_\ell. \tag{4.74}$$

Above, $\mathbf{E}_0(\mathbf{r}_j, \omega)$ is a driving electric field evaluated at the position of jth dipole, while the second term accounts for the scattered electric fields from the adjacent $\ell \neq j$ dipoles in the array. $\boldsymbol{\Lambda}(\mathbf{x})$ is the familiar dipole relay tensor, introduced in Eqn. (4.5). The fully relativistic electric dipole polarizability tensor is evaluated from the $\ell = 1$ electric Mie coefficient from Eqn. (C.11), as $\boldsymbol{\alpha}(\omega) = \mathbb{1}(3/2k^3)a_1(\omega)$. Eqn. (4.74) can be solved using the Bloch wave ansatz $\mathbf{p}_j(\mathbf{r}_j, \omega) = \mathbf{p}_j(\omega)e^{iq_\| y_j}$ considering an infinite 1D lattice array, with the array periodicity distributed along direction $\hat{\mathbf{y}}$, and where $q_\|$ is the reciprocal space momentum directed along the array periodicity, and limited to the first Brillouin zone. The ansatz readily supplies the Fourier amplitude solution for the jth positioned dipole as

$$\mathbf{p}_j(q_\|, \omega) = \left[\boldsymbol{\alpha}^{-1}(\omega) - \sum_{\ell \neq j} \Lambda(\mathbf{r}_j, \mathbf{r}_\ell) e^{iq_\| a\ell}\right]^{-1} \cdot \mathbf{E}_0([\mathbf{R}, q_\|], \omega) \tag{4.75}$$

$$= \boldsymbol{\Pi}(q_\|, \omega) \cdot \mathbf{E}_0([\mathbf{R}, q_\|], \omega)$$

where $\mathbf{R} = x\hat{\mathbf{x}} + z\hat{\mathbf{z}}$ are the transverse directional components perpendicular to the lattice, and $\boldsymbol{\Pi}$ is the lattice dressed polarizability of the dipole at site n. Then, the nth dipole moment, is found using the inverse Fourier transform as

$$\mathbf{p}_n(\mathbf{r}_n, \omega) = \int \frac{dq_\|}{2\pi} e^{iq_\| y_n} \boldsymbol{\Pi}(q_\|, \omega) \cdot \mathbf{E}_0(\mathbf{R}, q_\|, \omega). \tag{4.76}$$

Considering the electric field of a planewave, its Fourier representation is

$$\mathbf{E}_0(\mathbf{R}, q_\|, \omega) = \hat{\mathbf{e}}_0 (2\pi)^2 \frac{E_0}{2} \left[\delta(q_\| - K_\|)\delta(\omega - \omega_0) + \delta(q_\| + K_\|)\delta(\omega + \omega_0)\right], \tag{4.77}$$

which when inserted into the expression for the dipole moment above yields

$$\mathbf{p}_n(\mathbf{r}_n,\omega) = e^{iK_\parallel y_n}\mathbf{\Pi}(K_\parallel,\omega)\cdot\hat{e}_0\pi E_0\delta(\omega-\omega_0) + e^{-iK_\parallel y_n}\mathbf{\Pi}(-K_\parallel,\omega)\cdot\hat{e}_0\pi E_0\delta(\omega+\omega_0). \quad (4.78)$$

Transforming into the time domain, we find

$$\begin{aligned}\mathbf{p}_n(\mathbf{r}_n,t) &= \mathbf{\Pi}(K_\parallel,\omega_0)\cdot\hat{e}_0\frac{E_0}{2}e^{i(K_\parallel y_n-\omega_0 t)} + c.c. \\ &= \mathbf{p}^+(\mathbf{r},t) + \mathbf{p}^-(\mathbf{r},t).\end{aligned} \quad (4.79)$$

As derived by Garcia de Abajo [77, 38], the EEGS probability is expressed in terms of the target's induced field is

$$\mathcal{P}_{\text{EEG}}(\omega) = \left(\frac{e}{\hbar\omega}\right)^2\left|\int dz' E_z(\mathbf{R}_e,z')e^{-i\omega z'/v}\right|^2, \quad (4.80)$$

where the coordinates $(\mathbf{R}_e, z')$ indicate the electron trajectory propagating along direction $\hat{\mathbf{z}}$. In terms of the induced dipole at lattice site n, the induced electric field may be expressed in terms of the dyadic Green's tensor as

$$E_z(\mathbf{R}_e,z')e^{-i\omega t} = \hat{\mathbf{z}}\cdot\sum_n\left\{\left[\mathbb{1}k^2+\nabla_e\nabla_e\right]\frac{e^{ik|\mathbf{r}_e-\mathbf{r}_n|}}{|\mathbf{r}_e-\mathbf{r}_n|}\right\}\cdot\mathbf{\Pi}(K_\parallel,\omega)\cdot\mathbf{E}_0e^{iK_\parallel R_n}e^{-i\omega z'/v} \quad (4.81)$$

. From the integral identity for the modified Bessel functions of the second kind [31], we may now evaluate the integral over the electron coordinate z', as

$$\int dz' e^{-i\omega z'/v}\frac{e^{ik|\mathbf{r}-(\mathbf{R}_e,z')|}}{|\mathbf{r}-(\mathbf{R}_e,z')|} = 2K_0\left(\frac{\omega R_e}{\gamma_{\text{L}}v}\right)e^{-i\omega z'/v}. \quad (4.82)$$

Then substituting the gradient operators $\nabla_e \to -\nabla_n$, and choosing a polarization direction of $\hat{\mathbf{x}}$, we find for the integrand of $\mathcal{P}_{\text{EEG}}(\omega)$

$$\sum_n\hat{\mathbf{z}}\cdot\left[\mathbb{1}k^2+\nabla_n\nabla_n\right]\left\{2K_0\left(\frac{\omega R_{en}}{\gamma_{\text{L}}v}\right)e^{-i\omega z_n/v}\right\}\cdot\hat{\mathbf{x}}\;\Pi_{xx}(K_\parallel,\omega)E_0e^{iK_\parallel na}, \quad (4.83)$$

which yields the following result for the gain probability of the lattice under planewave excitation

$$\mathcal{P}_{\mathrm{EEG}}(\omega) = \left(\frac{2e\omega}{\hbar\gamma_{\mathrm{L}}v^2}\right)^2 |\Pi_{xx}(K_\parallel,\omega)|^2 \frac{2\pi}{c} I_0 \left|\sum_n \frac{b_x}{R_{en}} K_1\left(\frac{\omega R_{en}}{\gamma_{\mathrm{L}} v}\right) e^{iK_\parallel na}\right|^2, \tag{4.84}$$

where I_0 is the intensity of the x-polarized planewave, and R_{en} is the distance from the electron to the nth lattice site along the electron impact plane. To examine the validity of the analytic model, fully relativistic scattering calculations were performed using discrete volume element Maxwell solvers [78] for periodic dielectric targets under far-field planewave excitation. A comparison between model and simulation is examined in Fig. 4.7 Having demonstrated the unique advantages of LEEGS for spatially mapping LPP excitations in isolated periodic NP arrays, we now consider LPP-EPs that can emerge for a 1D Ag NP array embedded in an excitonic slab medium. The exciton medium is modeled using a Lorentz oscillator dielectric function $\epsilon(\omega) = 1 + f\omega_0^2/(\omega_0^2 - \omega^2 - i\gamma\omega)$, where ω_0 is the exciton transition frequency, γ is the exciton damping rate, and f is an effective oscillator strength. Note that while this is a standard approach for accounting for the exciton response in strong coupling systems with macroscopic numbers of emitters [79, 80, 81, 82, 83], this form of the exciton medium response is equivalent to replacing the discrete two-level system emitters by classical oscillators, which is a good approximation in the low excitation limit [84]. To avoid the possibility of Fabry-Pérot modes polluting the spectral features of interest, a slab thickness of 120 nm is employed in our calculations. In experiments, the Rabi splitting observable in the strong coupling regime can be varied by either increasing the emitter's transition dipole moment, or the concentration of emitters within the mode volume. Within the context of the Lorentz oscillator model, both are equivalent to increasing the value of the effective oscillator strength f. Fig. 4.8a shows the relative $\mathcal{P}_{\mathrm{EEG}}(\omega)$ and $\sigma_{\mathrm{abs}}(\omega)$ spectra at points P1 and P2 for the combined array-slab ($f = 0.0445$) system, i.e., the spectra at points P1 and P2 each normalized by the maximum value at P1. The point absorption spectrum is determined numerically using the relation $\sigma_{\mathrm{abs}}(\omega) = \omega|\mathbf{E}(\mathbf{R}, z)|^2\mathrm{Im}\{\varepsilon(\omega)\}$. While the spectra at P2 have the same shape as those observed at P1, the UP and LP amplitudes are considerably reduced. Although the demonstration of Rabi splitting in absorption spectra

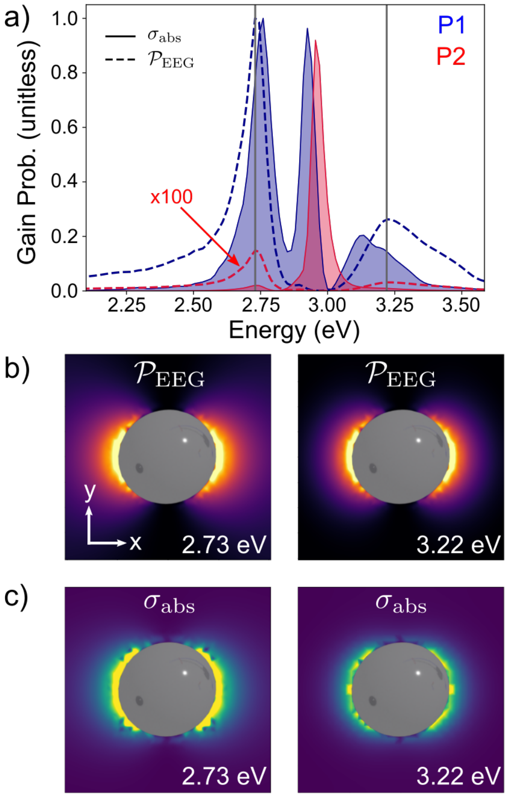

Figure 4.8: Spatially and spectrally resolving variations in LPP-EPs using STEM LEEG spectroscopy. Panel (a) examines normalized relative energy gain and absorption spectra at two different positions in the impact plane. Both positions P1 and P2 are located 5 nm from the sphere surface, however P1 is positioned in a 'hot spot' of high gain probability, indicated in the spectral gain maps of panel (b), while P2 is near a dark nodal region of the LPP-EP spatial mode map, resulting in a weaker lattice-gain signal.

is a more appropriate indication of strong coupling [80, 85, 86], local absorption measurements on the nanoscale remain experimentally challenging [87, 88, 89, 90] and dark-field scattering measurements are often easier to obtain for LSP-based systems. Despite ultimately measuring a scattering response, the variation in the $\mathcal{P}_{\text{EEG}}(\omega)$ amplitudes at the UP and LP energies can be used to create spatial maps of the optically excited LPP-EPs as the STEM electron beam is raster scanned throughout the unit cell. Similar to what has been observed for LSP-EPs [86], both sets of spectrum images presented in Figs. 4.8b,c exhibit a characteristic dipole distribution indicating the role played by the electric dipole

LSPs comprising the delocalized LPP mode at $K_{||} = 0$. Interestingly, absorption and LEEG observables each capture the contracted spatial extent of the UP relative to that of the LP. We attribute this difference to the in-phase (out-of-phase) coupling between the LSP and slab modes at the LP (UP) energy as indicated by the electric field distributions in the insets in Fig. 4.8a. By fitting the decay profiles of the normalized absorption and LEEG observables in Figs. 4.8b,c along the x-direction to a mono-exponential function, we find that the $1/e$ decay length of the LEEG spectrum image UP and LP are 63.19 nm and 70.79 nm, respectively – both $\sim 14\%$ larger than the decay constants of the absorption spectral images. Therefore, despite measuring a scattering response, LEEG measurements are a reliable reporter of the sub-diffraction-limited spatial variation of upper and lower polaritons at the nanometer-scale.

BIBLIOGRAPHY

[1] Marc R Bourgeois, Elliot K Beutler, Siamak Khorasani, Nicole Panek, and David J Masiello. Nanometer-scale spatial and spectral mapping of exciton polaritons in structured plasmonic cavities. *Physical Review Letters*, 128(19):197401, 2022.

[2] Elliot K Beutler, Maureen J Lagos, and David J Masiello. Infrared surface phonon nanospectroscopy of an interacting dielectric-particle–dielectric-substrate dimer using fast electrons. *Physical Review B*, 103(16):165418, 2021.

[3] Chenze Liu, Yueying Wu, Zhongwei Hu, Jacob A Busche, Elliot K Beutler, Nicholas P Montoni, Thomas M Moore, Gregory A Magel, Jon P Camden, David J Masiello, et al. Continuous wave resonant photon stimulated electron energy-gain and electron energy-loss spectroscopy of individual plasmonic nanoparticles. *ACS Photonics*, 6(10):2499–2508, 2019.

[4] Ujjal Bhattacharjee, Claire A West, Seyyed Ali Hosseini Jebeli, Harrison J Goldwyn, Xiang-Tian Kong, Zhongwei Hu, Elliot K Beutler, Wei-Shun Chang, Katherine A Willets, Stephan Link, et al. Active far-field control of the thermal near-field via plasmon hybridization. *ACS nano*, 13(8):9655–9663, 2019.

[5] James Clerk Maxwell. A dynamical theory of the electromagnetic field. *Philosophical Transactions of the Royal Society of London*, (155):459–512, 1865.

[6] Olivier Darrigol. *Electrodynamics from Ampere to Einstein.* Oxford University Press, 2003.

[7] Paul M. Dirac. The quantum theory of the emission and absorption of radiation. In *Special Relativity and Quantum Theory*, pages 157–179. Springer, 1988.

[8] Enrico Fermi. Quantum theory of radiation. *Reviews of Modern Physics*, 4(1):87, 1932.

[9] Hans Albrecht Bethe. The electromagnetic shift of energy levels. *Physical Review*, 72(4):339, 1947.

[10] Sin-itiro Tomonaga. On a relativistically invariant formulation of the quantum theory of wave fields. *Progress of Theoretical Physics*, 1(2):27–42, 1946.

[11] Julian Schwinger. On quantum-electrodynamics and the magnetic moment of the electron. *Physical Review*, 73(4):416, 1948.

[12] Julian Schwinger. Quantum electrodynamics: A covariant formulation. *Physical Review*, 74(10):1439, 1948.

[13] Richard Phillips Feynman. Space-time approach to quantum electrodynamics. *Physical Review*, 76(6):769, 1949.

[14] Richard P Feynman. The theory of positrons. *Physical Review*, 76(6):749, 1949.

[15] Richard Phillips Feynman. Mathematical formulation of the quantum theory of electromagnetic interaction. *Physical Review*, 80(3):440, 1950.

[16] Freeman J Dyson. The radiation theories of Tomonaga, Schwinger, and Feynman. *Physical Review*, 75(3):486, 1949.

[17] Freeman J Dyson. The s matrix in quantum electrodynamics. *Physical Review*, 75(11):1736, 1949.

[18] Klaus-Peter Lieb. Theodor schmidt and hans kopfermann–pioneers in hyperfine physics. *Hyperfine interactions*, 136(3):783–802, 2001.

[19] Isaac Newton. *Opticks, or, a treatise of the reflections, refractions, inflections & colours of light*. Courier Corporation, 1952.

[20] D Chilton. A source book in physics. by william francis magie. eighth printing. pp. xiv+ 620. harvard university press, cambridge, massachusetts, 1963.£ 4 4s. *The British Journal for the History of Science*, 2(4):362–363, 1965.

[21] Joseph Fraunhofer. Bestimmung des brechungs-und des farbenzerstreungs-vermögens verschiedener glasarten, in bezug auf die vervollkommnung achromatischer fernröhre. *Annalen der Physik*, 56(7):264–313, 1817.

[22] JJ Balmer. A new formula for the wave-lengths of spectral lines. *The Astrophysical Journal*, 5:199, 1897.

[23] Gustav Kirchhoff. Ueber die fraunhofer'schen linien. *Annalen der Physik*, 185(1):148–150, 1860.

[24] Gustav Kirchhoff. Über das verhältnis zwischen dem emissionsvermögen und dem absorptionsvermögen der körper für wärme und licht. In *Von Kirchhoff bis Planck*, pages 131–151. Springer, 1978.

[25] WH Walloston. A method of examining refractive and dispersive powers by prismatic reflection. *Philosophical Transactions of the Royal Society*, (92):365–380, 1802.

[26] JR Rydberg. Xxxiv. on the structure of the line-spectra of the chemical elements. *The London, Edinburgh, and Dublin Philosophical Magazine and Journal of Science*, 29(179):331–337, 1890.

[27] Theodore Lyman. The spectrum of hydrogen in the region of extremely short wavelengths. *The Astrophysical Journal*, 23:181, 1906.

[28] Friedrich Paschen. *Ueber die zum funkenübergang in luft: wasserstoff und kohlensäure bei verschiedenen drucken erforderliche potentialdifferenz...* JA Barth, 1889.

[29] Otfried Madelung. *Introduction to solid-state theory*, volume 2. Springer Science & Business Media, 2012.

[30] Amnon Yariv. *Optical Electronics*. Saunders College Publishing, 1991.

[31] Julian Schwinger, Lester L DeRaad Jr, Kimball Milton, and Wu-yang Tsai. *Classical Electrodynamics*. Westview Press, 1998.

[32] Kevin Cahill. Models of membrane electrostatics. *Physical Review E*, 85(5):051921, 2012.

[33] Frederick W Byron and Robert W Fuller. *Mathematics of Classical and Quantum Physics*. Courier Corporation, 2012.

[34] A Rivacoba, N Zabala, and J Aizpurua. Image potential in scanning transmission electron microscopy. *Progress in Surface Science*, 65(1-2):1–64, 2000.

[35] Charles Cherqui, Niket Thakkar, Guoliang Li, Jon P Camden, and David J Masiello. Characterizing localized surface plasmons using electron energy-loss spectroscopy. *Annual Review of Physical Chemistry*, 67:331–357, 2016.

[36] Edward M Purcell and David J Morin. *Electricity and magnetism*. Cambridge University Press, 2013.

[37] John David Jackson. Classical electrodynamics, 1999.

[38] FJ García De Abajo. Optical excitations in electron microscopy. *Reviews of modern physics*, 82(1):209, 2010.

[39] Rufus H Ritchie. Plasma losses by fast electrons in thin films. *Physical Review*, 106(5):874, 1957.

[40] Milton Abramowitz and Irene A Stegun. *Handbook of Mathematical Functions with Formulas, Graphs, and Mathematical Tables*, volume 55. US Government printing office, 1948.

[41] A Rodríguez Echarri, Enok Johannes Haahr Skjølstrup, Thomas G Pedersen, and F Javier García de Abajo. Theory of electron energy-loss spectroscopy in atomically thin metallic films. *Physical Review Research*, 2(2):023096, 2020.

[42] Jun John Sakurai and Eugene D Commins. Modern quantum mechanics, revised edition, 1995.

[43] Albert Messiah. Chap. xvi and xvii. In *Quantum mechanics*, volume 2. Wiley New York, 1966.

[44] Bernard A Lippmann and Julian Schwinger. Variational principles for scattering processes. i. *Physical Review*, 79(3):469, 1950.

[45] Ondrej L Krivanek, Tracy C Lovejoy, Neil J Bacon, George J Corbin, N Dellby, P Hrncirik, Matthew F Murfitt, Gwyn Skone, Zoltan S Szilagyi, and Philip E Batson. High energy resolution monochromated EELS-STEM system. *Microscopy and Microanalysis*, 19(S2):1124–1125, 2013.

[46] Ondrej L Krivanek, Tracy C Lovejoy, Matthew F Murfitt, Gwyn Skone, Philip E Batson, and Niklas Dellby. Towards sub-10 mev energy resolution STEM-EELS. *Journal of Physics: Conference Series*, 522(1):012023, 2014.

[47] Claude Cohen-Tannoudji, Bernard Diu, and Franck Laloë. *Quantum Mechanics, Volume 1: Basic Concepts, Tools, and Applications.* John Wiley & Sons, 2019.

[48] Maureen J Lagos and Philip E Batson. Thermometry with subnanometer resolution in the electron microscope using the principle of detailed balancing. *Nano Letters*, 18(7):4556–4563, 2018.

[49] Juan Carlos Idrobo, Andrew R Lupini, Tianli Feng, Raymond R Unocic, Franklin S Walden, Daniel S Gardiner, Tracy C Lovejoy, Niklas Dellby, Sokrates T Pantelides, and Ondrej L Krivanek. Temperature measurement by a nanoscale electron probe using energy gain and loss spectroscopy. *Physical review letters*, 120(9):095901, 2018.

[50] Ondrej L Krivanek, Tracy C Lovejoy, Niklas Dellby, Toshihiro Aoki, RW Carpenter, Peter Rez, Emmanuel Soignard, Jiangtao Zhu, Philip E Batson, and Maureen J Lagos. Vibrational spectroscopy in the electron microscope. *Nature*, 514(7521):209–212, 2014.

[51] Jordan A Hachtel, Andrew R Lupini, and Juan Carlos Idrobo. Exploring the capabilities of monochromated electron energy loss spectroscopy in the infrared regime. *Scientific Reports*, 8(1):1–10, 2018.

[52] PC Tiemeijer, M Bischoff, B Freitag, and C Kisielowski. Using a monochromator to improve the resolution in tem to below 0.5 Å. part i: Creating highly coherent monochromated illumination. *Ultramicroscopy*, 114:72–81, 2012.

[53] Philip E Batson, Niklas Dellby, and Ondrej L Krivanek. Sub-Ångstrom resolution using aberration corrected electron optics. *Nature*, 418(6898):617–620, 2002.

[54] Peter Rez, Toshihiro Aoki, Katia March, Dvir Gur, Ondrej L Krivanek, Niklas Dellby, Tracy C Lovejoy, Sharon G Wolf, and Hagai Cohen. Damage-free vibrational spectroscopy of biological materials in the electron microscope. *Nature Communications*, 7(1):1–8, 2016.

[55] Diane M Haiber and Peter A Crozier. Nanoscale probing of local hydrogen heterogeneity in disordered carbon nitrides with vibrational electron energy-loss spectroscopy. *ACS Nano*, 12(6):5463–5472, 2018.

[56] Ulrich Hohenester, Andreas Trügler, Philip E Batson, and Maureen J Lagos. Inelastic vibrational bulk and surface losses of swift electrons in ionic nanostructures. *Physical Review B*, 97(16):165418, 2018.

[57] Kartik Venkatraman, Barnaby DA Levin, Katia March, Peter Rez, and Peter A Crozier. Vibrational spectroscopy at atomic resolution with electron impact scattering. *Nature Physics*, 15(12):1237–1241, 2019.

[58] Hugo Lourenço-Martins and Mathieu Kociak. Vibrational surface electron-energy-loss spectroscopy probes confined surface-phonon modes. *Physical Review X*, 7(4):041059, 2017.

[59] Peter A Crozier. Vibrational and valence aloof beam EELS: A potential tool for nondestructive characterization of nanoparticle surfaces. *Ultramicroscopy*, 180:104–114, 2017.

[60] Christian Dwyer, T Aoki, Peter Rez, SLY Chang, TC Lovejoy, and OL Krivanek. Electron-beam mapping of vibrational modes with nanometer spatial resolution. *Physical Review Letters*, 117(25):256101, 2016.

[61] Maureen J Lagos, Andreas Trügler, Ulrich Hohenester, and Philip E Batson. Mapping vibrational surface and bulk modes in a single nanocube. *Nature*, 543(7646):529–532, 2017.

[62] Maureen J Lagos, Andreas Trügler, Voshadhi Amarasinghe, Leonard C Feldman, Ulrich Hohenester, and Philip E Batson. Excitation of long-wavelength surface optical vibrational modes in films, cubes and film/cube composite system using an atom-sized electron beam. *Microscopy*, 67(suppl_1):3–13, 2018.

[63] Xingxu Yan, Chengyan Liu, Chaitanya A Gadre, Lei Gu, Toshihiro Aoki, Tracy C Lovejoy, Niklas Dellby, Ondrej L Krivanek, Darrell G Schlom, and Ruqian Wu. Single-defect phonons imaged by electron microscopy. *Nature*, 589(7840):65–69, 2021.

[64] Anatoliy Pinchuk, Almuth Hilger, Gero von Plessen, and Uwe Kreibig. Substrate effect on the optical response of silver nanoparticles. *Nanotechnology*, 15(12):1890, 2004.

[65] Charles Cherqui, Guoliang Li, Jacob A Busche, Steven C Quillin, Jon P Camden, and David J Masiello. Multipolar nanocube plasmon mode-mixing in finite substrates. *Journal of Physical Chemistry Letters*, 9(3):504–512, 2018.

[66] Shima Kadkhodazadeh, Thomas Christensen, Marco Beleggia, N Asger Mortensen, and Jakob B Wagner. The substrate effect in electron energy-loss spectroscopy of localized surface plasmons in gold and silver nanoparticles. *ACS Photonics*, 4(2):251–261, 2017.

[67] Guoliang Li, Charles Cherqui, Nicholas W Bigelow, Gerd Duscher, Patrick J Straney, Jill E Millstone, David J Masiello, and Jon P Camden. Spatially mapping energy transfer from single plasmonic particles to semiconductor substrates via STEM/EELS. *Nano Letters*, 15(5):3465–3471, 2015.

[68] Yoshifumi Fujiyoshi, Takashi Nemoto, and Hiroki Kurata. Substrate effects on LSP of a truncated silver nano-sphere observed by EELS. *Microscopy*, 64(suppl_1):99–99, 2015.

[69] Yoshifumi Fujiyoshi, Takashi Nemoto, and Hiroki Kurata. Studying substrate effects on localized surface plasmons in an individual silver nanoparticle using electron energy-loss spectroscopy. *Ultramicroscopy*, 175:116–120, 2017.

[70] David Kordahl and Christian Dwyer. Enhanced vibrational electron energy-loss spectroscopy of adsorbate molecules. *Physical Review B*, 99(10):104110, 2019.

[71] Sarah Griffin, Nicholas P Montoni, Guoliang Li, Patrick J Straney, Jill E Millstone, David J Masiello, and Jon P Camden. Imaging energy transfer in pt-decorated au nanoprisms via electron energy-loss spectroscopy. *The journal of physical chemistry letters*, 7(19):3825–3832, 2016.

[72] Steven C Quillin, Charles Cherqui, Nicholas P Montoni, Guoliang Li, Jon P Camden, and David J Masiello. Imaging plasmon hybridization in metal nanoparticle aggregates with electron energy-loss spectroscopy. *The Journal of Physical Chemistry C*, 120(37):20852–20859, 2016.

[73] Herbert Fröhlich. *Theory of Dielectrics: Dielectric Constant and Dielectric Loss*, volume 190. Oxford University Press, USA, 1958.

[74] FJ García de Abajo and PM Echenique. Wake potential in the vicinity of a surface. *Physical Review B*, 46(5):2663, 1992.

[75] Nicholas W Bigelow, Alex Vaschillo, Vighter Iberi, Jon P Camden, and David J Masiello. Characterization of the electron-and photon-driven plasmonic excitations of metal nanorods. *ACS Nano*, 6(8):7497–7504, 2012.

[76] Nicholas W Bigelow, Alex Vaschillo, Jon P Camden, and David J Masiello. Signatures of Fano interferences in the electron energy loss spectroscopy and cathodoluminescence of symmetry-broken nanorod dimers. *ACS Nano*, 7(5):4511–4519, 2013.

[77] Ana Asenjo-Garcia and FJ García De Abajo. Plasmon electron energy-gain spectroscopy. *New Journal of Physics*, 15(10):103021, 2013.

[78] Bruce T Draine and Piotr J Flatau. Discrete-dipole approximation for scattering calculations. *Journal of the Optical Society of America A*, 11(4):1491–1499, 1994.

[79] AI Väkeväinen, RJ Moerland, HT Rekola, A-P Eskelinen, J-P Martikainen, D-H Kim, and P Törmä. Plasmonic surface lattice resonances at the strong coupling regime. *Nano Lett.*, 14(4):1721–1727, 2013.

[80] Tomasz J Antosiewicz, S Peter Apell, and Timur Shegai. Plasmon–exciton interactions in a core–shell geometry: from enhanced absorption to strong coupling. *ACS Photonics*, 1(5):454–463, 2014.

[81] Wenjing Liu, Bumsu Lee, Carl H Naylor, Ho-Seok Ee, Joohee Park, AT Charlie Johnson, and Ritesh Agarwal. Strong exciton–plasmon coupling in mos$_2$ coupled with plasmonic lattice. *Nano Lett.*, 16(2):1262–1269, 2016.

[82] Andrea Konečná, Tomáš Neuman, Javier Aizpurua, and Rainer Hillenbrand. Surface-enhanced molecular electron energy loss spectroscopy. *ACS Nano*, 12(5):4775–4786, 2018.

[83] Ravindra Kumar Yadav, Marc R Bourgeois, Charles Cherqui, Xitlali G Juarez, Weijia Wang, Teri W Odom, George C Schatz, and Jaydeep Kumar Basu. Room temperature weak-to-strong coupling and the emergence of collective emission from quantum dots coupled to plasmonic arrays. *ACS Nano*, 14(6):7347–7357, 2020.

[84] Sudhakar Prasad and Roy J Glauber. Coherent radiation by a spherical medium of resonant atoms. *Phys. Rev. A*, 82(6):063805, 2010.

[85] Matthew Pelton, S David Storm, and Haixu Leng. Strong coupling of emitters to single plasmonic nanoparticles: exciton-induced transparency and rabi splitting. *Nanoscale*, 11(31):14540–14552, 2019.

[86] Andrew B Yankovich, Battulga Munkhbat, Denis G Baranov, Jorge Cuadra, Erik Olsén, Hugo Lourenço-Martins, Luiz HG Tizei, Mathieu Kociak, Eva Olsson, and Timur Shegai. Visualizing spatial variations of plasmon-exciton polaritons at the nanoscale using electron microscopy. *Nano Lett.*, 19(11):8171–8181, 2019.

[87] Kevin D Heylman, Niket Thakkar, Erik H Horak, Steven C Quillin, Charles Cherqui, Kassandra A Knapper, David J Masiello, and Randall H Goldsmith. Optical microresonators as single-particle absorption spectrometers. *Nat. Photonics*, 10(12):788–795, 2016.

[88] Niket Thakkar, Morgan T Rea, Kevin C Smith, Kevin D Heylman, Steven C Quillin, Kassandra A Knapper, Erik H Horak, David J Masiello, and Randall H Goldsmith. Sculpting fano resonances to control photonic–plasmonic hybridization. *Nano Lett.*, 17(11):6927–6934, 2017.

[89] Feng Pan, Kevin C Smith, Hoang L Nguyen, Kassandra A Knapper, David J Masiello, and Randall H Goldsmith. Elucidating energy pathways through simultaneous measurement of absorption and transmission in a coupled plasmonic-photonic cavity. *Nano Lett.*, 20(1):50–58, 2019.

[90] Kevin C Smith, Agust Olafsson, Xuan Hu, Steven C Quillin, Juan Carlos Idrobo, Robyn Collette, Philip D Rack, Jon P Camden, and David J Masiello. Direct observation of infrared plasmonic fano antiresonances by a nanoscale electron probe. *Phys. Rev. Lett.*, 123(17):177401, 2019.

[91] Edward D Palik. *Handbook of Optical Constants of Solids*, volume 3. Academic press, 1998.

[92] LD Marks. Observation of the image force for fast electrons near an MgO surface. *Solid State Communications*, 43(10):727–729, 1982.

[93] A Rodríguez Echarri, Joel D Cox, and F Javier García de Abajo. Quantum effects in the acoustic plasmons of atomically thin heterostructures. *Optica*, 6(5):630–641, 2019.

[94] Ludvig Lorenz. Ueber die refractionsconstante. *Annalen der Physik*, 247(9):70–103, 1880.

[95] Izrail Solomonovich Gradshteyn and Iosif Moiseevich Ryzhik. *Table of integrals, series, and products*. Academic press, 2014.

[96] Howard S Cohl and Joel E Tohline. A compact cylindrical green's function expansion for the solution of potential problems. *The Astrophysical Journal*, 527(1):86, 1999.

[97] Victor Namias. Application of the dirac delta function to electric charge and multipole distributions. *American Journal of Physics*, 45(7):624–630, 1977.

[98] Noboru Takimoto. Plasmon excitation by charged particles outside a metal film. *Physical Review*, 146(1):366, 1966.

[99] PM Echenique and JB Pendry. Absorption profile at surfaces. *Journal of Physics C: Solid State Physics*, 8(18):2936, 1975.

[100] SS Mandal and DN Tripathy. Equation of motion approach to the plasmon-plasmon interaction in a many-electron system. *Physics Letters A*, 72(6):459–463, 1979.

[101] Ronald Fuchs and KL Kliewer. Optical modes of vibration in an ionic crystal slab. *Physical Review*, 140(6A):A2076, 1965.

[102] AM Hofmeister, E Keppel, and AK Speck. Absorption and reflection infrared spectra of MgO and other diatomic compounds. *Monthly Notices of the Royal Astronomical Society*, 345(1):16–38, 2003.

[103] DL Mills and E Burstein. Polaritons: the electromagnetic modes of media. *Reports on Progress in Physics*, 37(7):817, 1974.

[104] Guoliang Li, Charles Cherqui, Yueying Wu, Nicholas W Bigelow, Philip D Simmons, Philip D Rack, David J Masiello, and Jon P Camden. Examining substrate-induced plasmon mode splitting and localization in truncated silver nanospheres with electron energy loss spectroscopy. *The journal of physical chemistry letters*, 6(13):2569–2576, 2015.

[105] JY Yang, WJ Zhang, LH Liu, J Qiu, K Wang, and JY Tan. Temperature-dependent infrared dielectric functions of mgo crystal: an ellipsometry and first-principles molecular dynamics study. *The Journal of chemical physics*, 141(10):104703, 2014.

[106] P Törmä and William L Barnes. Strong coupling between surface plasmon polaritons and emitters: a review. *Rep. Prog. Phys.*, 78(1):013901, 2014.

Appendix A

THE HARMONIC OSCILLATOR GREEN'S FUNCTION

For a damped, forced harmonic oscillator, the corresponding Newton equation is

$$L\mathbf{x}(t) = \frac{\mathbf{F}(t)}{m} \tag{A.1}$$

Where the linear operator L is defined as

$$L = \frac{d^2}{dt^2} + \gamma\frac{d}{dt} + \omega_0^2 \tag{A.2}$$

The associated Green's function is defined by

$$Lg_{\mathrm{HO}}(t - t') = \delta(t - t') \tag{A.3}$$

Expressing the Green's function and the impulse delta function in terms of a spectral decomposition

$$g_{\mathrm{HO}}(t - t') = \int_{-\infty}^{\infty} \frac{d\omega}{2\pi} g(\omega) e^{-i\omega t} \tag{A.4}$$

$$\delta(t - t') = \int_{-\infty}^{\infty} \frac{d\omega}{2\pi} e^{-i\omega(t-t')}, \tag{A.5}$$

it is then a trivial matter to construct the spectral representation of the harmonic oscillator Green's function

$$g_{\mathrm{HO}}(\omega) = \frac{1}{\omega_0^2 - \omega^2 - i\gamma\omega}. \tag{A.6}$$

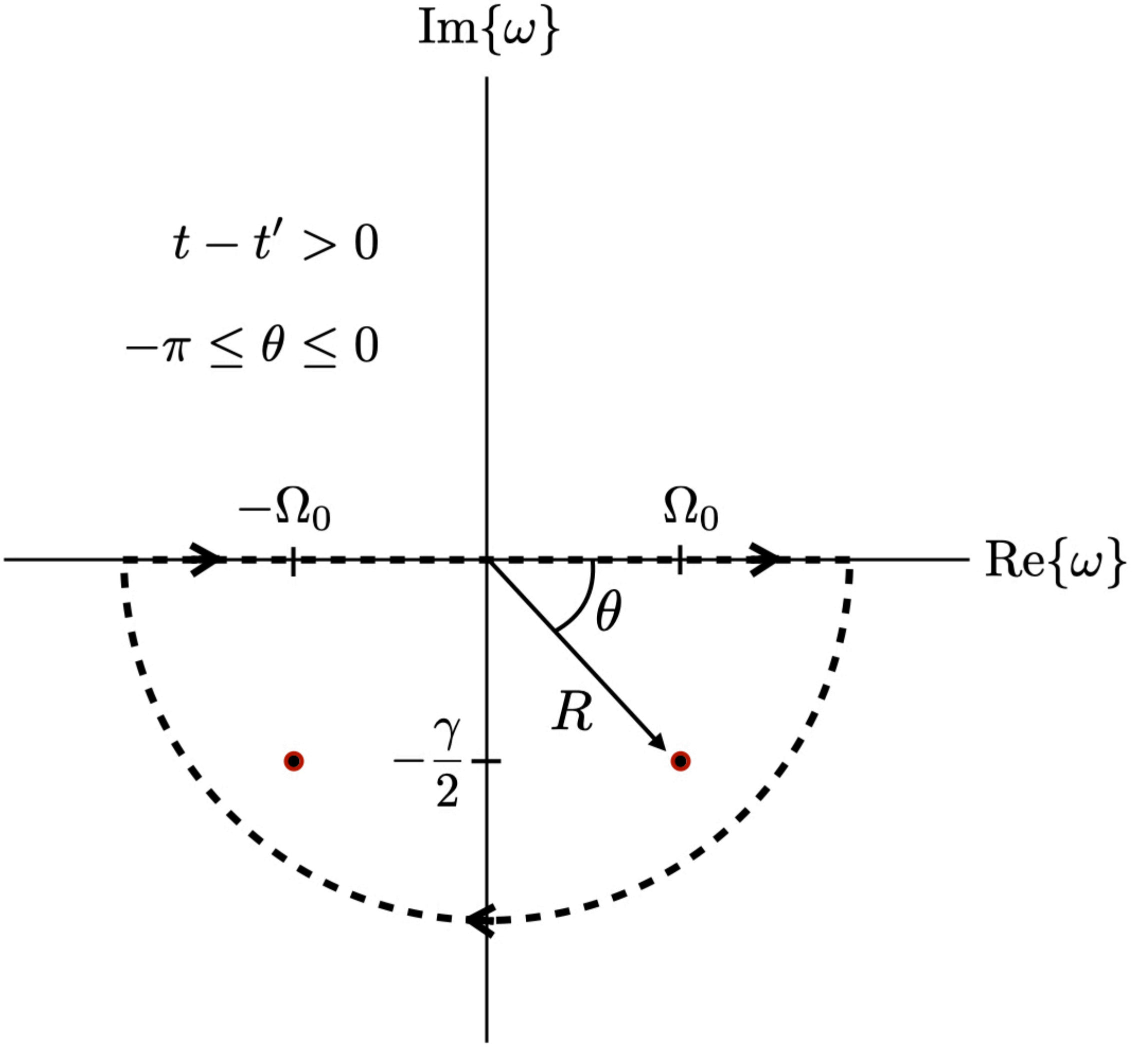

Figure A.1: Plot of the poles of the spectral representation of the harmonic oscillator Green's function, residing in the complex ω-plane. By enforcing causality $t - t' > 0$, the contour is closed in the lower half of the complex plane (i.e. $-\pi \leq \theta \leq 0$).

Therefore, in the time domain, the Green's function is defined as

$$g_{\mathrm{HO}}(t-t') = \int_{-\infty}^{\infty} \frac{d\omega}{2\pi} \frac{e^{-i\omega(t-t')}}{\omega_0^2 - \omega^2 - i\gamma\omega}. \tag{A.7}$$

This integral is simple to evaluate with the aid of contour integration. We begin by identifying the poles of the integrand, $\omega_\pm = -i\gamma/2 \pm \Omega_0$, where $\Omega_0 = \sqrt{\omega_0^2 - \gamma^2/4}$. Then, defining $\omega = Re^{i\theta}$, where R is a purely real quantity measuring the magnitude of ω, and the angle θ determines the projection of ω into the complex plane, we write the contour integral

$$\begin{aligned} g_{\mathrm{HO}}(t-t') &= \oint \frac{d\omega}{2\pi} \frac{e^{-iR\{\cos\theta + i\sin\theta\}(t-t')}}{(\omega-\omega_+)(\omega-\omega_-)} \\ &= 2\pi i \sum_k a_k, \end{aligned} \tag{A.8}$$

where we have utilized Cauchy's residue theorem to evaluate the integral, and a_k are the residues of the integrand. By enforcing causality, where the response at time t must occur after the impulse provided by the delta function at time t' (i.e. $t - t' > 0$, and requiring that the integrand must go to zero as $R \to \infty$, we close the contour integral in the lower half of the complex plane. Observing that we have two simple poles in this region, the two associated residues are evaluated by

$$\begin{aligned} a_+ &= \frac{1}{2\pi} \lim_{\omega\to\omega_+} (\omega-\omega_+) \frac{e^{-i\omega(t-t')}}{(\omega-\omega_+)(\omega-\omega_-)} \\ &= \frac{1}{2\pi} \frac{e^{-\gamma(t-t')/2} e^{i\Omega_0(t-t')}}{2\Omega_0} \\ a_- &= \frac{1}{2\pi} \lim_{\omega\to\omega_-} (\omega-\omega_-) \frac{e^{-i\omega(t-t')}}{(\omega-\omega_+)(\omega-\omega_-)} \\ &= -\frac{1}{2\pi} \frac{e^{-\gamma(t-t')/2} e^{i\Omega_0(t-t')}}{2\Omega_0} \end{aligned} \tag{A.9}$$

All together, the harmonic oscillator Green's function is

$$g_{\mathrm{HO}}(t-t') = \frac{e^{-\gamma(t-t')/2}}{\Omega_0} \sin \Omega_0 (t-t') \tag{A.10}$$

Appendix B

THE HARMONIC OSCILLATOR'S CREATION AND ANNIHILATION OPERATORS

Considering the Hamiltonian of an oscillatory body in the absence of external damping or internal frictional forces,

$$H = \frac{p^2}{2m} + \frac{1}{2}m\omega^2 u^2, \tag{B.1}$$

we can apply Hamilton's equations,

$$\frac{\partial H}{\partial p} = \frac{\partial u}{\partial t}; \quad \frac{\partial H}{\partial u} = -\frac{\partial p}{\partial t}, \tag{B.2}$$

to arrive at the Newton equation for the simple harmonic oscillator

$$m\ddot{u}(t) + m\omega^2 u(t) = 0. \tag{B.3}$$

It is then customary to propose a solution $u = e^{\pm st}$ which produces the auxillary equation

$$s^2 + w^2 = 0, \tag{B.4}$$

, with solutions $s = \pm i\omega$. Therefore, a general solution to the equation of motion and its first derivative on time is

$$\begin{aligned} u(t) &= Ae^{i\omega t} + Be^{-i\omega t} \\ \dot{u}(t) &= i\omega\left(Ae^{i\omega t} - Be^{-i\omega t}\right) \end{aligned} \tag{B.5}$$

The coefficients A, B are determined by the system's initial conditions (i.e. $t = 0$). Defining $u_0 = u(0), v_0 = \dot{u}(0)$, we then construct the matrix

$$\begin{pmatrix} u_0 \\ v_0 \end{pmatrix} = \begin{pmatrix} 1 & 1 \\ i\omega & -i\omega \end{pmatrix} \begin{pmatrix} A \\ B \end{pmatrix} \tag{B.6}$$

. Solving for the coefficient vector via matrix inversion, we find

$$\begin{pmatrix} A \\ B \end{pmatrix} = -\frac{1}{2i\omega} \begin{pmatrix} -i\omega & -1 \\ -i\omega & 1 \end{pmatrix} \begin{pmatrix} u_0 \\ v_0 \end{pmatrix}. \tag{B.7}$$

Defining the initial momentum $p_0 = mv_0$ and using the solutions for the coefficients in terms of the initial position and momentum, we find

$$u(t) = \frac{u_0}{2}\left(e^{i\omega t} + e^{-i\omega t}\right) + \frac{p_0}{2im\omega}\left(e^{i\omega t} - e^{-i\omega t}\right). \tag{B.8}$$

After some rearranging, we find

$$\begin{aligned} u(t) &= \frac{1}{2}\left(u_0 + \frac{p_0}{im\omega}\right) e^{i\omega t} + \frac{1}{2}\left(u_0 - \frac{p_0}{im\omega}\right) e^{-i\omega t} \\ &= A^\dagger e^{i\omega t} + A e^{-i\omega t}, \end{aligned} \tag{B.9}$$

. Imposing the commutation relation $[u_0, p_0] = i\hbar$, we readily find the commutator for our newly defined operators $[A, A^\dagger] = \hbar/2m\omega$. We may then non-dimensionalize our resulting operators, defining $a^\dagger = \sqrt{2m\omega/\hbar}A^\dagger$ and $a = \sqrt{2m\omega/\hbar}A$. Finally, we notice then that

$$\begin{aligned}
a^\dagger &= \sqrt{\frac{m\omega}{2\hbar}}\left(u_0 - i\frac{p_0}{m\omega}\right) \\
a &= \sqrt{\frac{m\omega}{2\hbar}}\left(u_0 + i\frac{p_0}{m\omega}\right) \\
u_0 &= \sqrt{\frac{\hbar}{2m\omega}}\left(a^\dagger + a\right) \\
p_0 &= i\sqrt{\frac{\hbar m\omega}{2}}\left(a^\dagger - a\right)
\end{aligned} \tag{B.10}$$

Appendix C

MIE SCATTERING

An exact solution to the scattering and extinction cross section of a spherical particles (regardless of particle size) by an incident plane wave are found by solving the vector Helmholtz equation in spherical coordinates. The Helmholtz equation for the electric and magnetic fields can be easily derived from Maxwell's equations

$$\nabla^2\mathbf{E} + k^2\mathbf{E} = 0$$
$$\nabla^2\mathbf{H} + k^2\mathbf{H} = 0 \tag{C.1}$$

. In the absence of charges, the electric and magnetic fields must satisfy the conditions

$$\nabla \cdot \mathbf{E} = 0$$
$$\nabla \cdot \mathbf{H} = 0$$
$$\nabla \times \mathbf{E} = i\omega\mu_b\mathbf{H} \tag{C.2}$$
$$\nabla \times \mathbf{H} = -i\omega\varepsilon_b\mathbf{E},$$

where $\mu, \varepsilon = n^2$ are the respective magnetic and electric permeabilities of the surrounding environment. A general solution to these conditions are satsified by the vector spherical harmonic functions

$$\mathbf{M}^{eo}_{mn} = \nabla \times (\mathbf{r}\psi^{eo}_{mn})$$
$$\mathbf{N}^{eo}_{mn} = \frac{\nabla \times \nabla \times (\mathbf{r}\psi^{eo}_{mn})}{k}, \tag{C.3}$$

where **M** and **N** are the respective magnetic and electric vector harmonic functions. They both depend on the general solution to the associated scalar Helmholtz equation, where the even and odd solutions are $\psi^{e}_{mn} = \text{Re}\{e^{im\phi}P_{mn}(\cos\theta)z_n(kr)\}$ and $\psi^{o}_{mn} = \text{Im}\{e^{im\phi}P_{mn}(\cos\theta)z_n(kr)\}$, in terms of the Associated Legendre polynomials, and a to-be-determined form of the spherical Bessel functions. Next, the incident planewave (polarized along direction $\hat{\mathbf{x}}$) is expanded in the vector spherical harmonic basis as:

$$\begin{aligned}\mathbf{E}_{\text{pw}} &= E_0 e^{ik\cos\theta}\hat{\mathbf{x}} \\ &= E_0 \sum_{n=1}^{\infty} i^n \frac{2n+1}{n(n+1)} \left(\text{Im}\{\mathbf{M}^{(1)}_{1n}\} - i\text{Re}\{\mathbf{N}^{(1)}_{1n}\}\right)\end{aligned}$$
$$\mathbf{H}_{\text{pw}} = \frac{k}{\omega\mu_b} E_0 \sum_{n=1}^{\infty} i^n \frac{2n+1}{n(n+1)} \left(\text{Re}\{\mathbf{M}^{(1)}_{1n}\} + i\text{Im}\{\mathbf{N}^{(1)}_{1n}\}\right), \tag{C.4}$$

where the superscript (1) indicates that the radial parts of the scalar solutions ψ are spherical Bessel functions $j_n(x)$ of the first kind. The expansion coefficients for the planewave are obtained by evaluating the integrals over the solid angle $d\Theta = d\theta d\phi \sin\theta$, as

$$\frac{\int d\Theta\ \mathbf{E}_{\text{pw}} \cdot \mathbf{M}^{(1)}}{\int d\Theta\ |\mathbf{M}^{(1)}|^2}, \tag{C.5}$$

where all coefficients for $m \neq 1$ are zero. Then, imposing the boundary conditions allowing us to relate the expansion coefficients of the incident, internal and externally scattering field, along with the conditions of ‘finiteness’ of the fields at the origin and at infinity, we solve for the scattered fields, external to the spherical boundary as

$$\begin{aligned}
\mathbf{E}_{\text{sca}} &= \sum_{n=1}^{\infty} E_n \left(i a_n \mathrm{Re}\{\mathbf{N}_{1n}^{(3)}(k,\mathbf{r})\} - b_n \mathrm{Im}\{\mathbf{N}_{1n}^{(3)}(k,\mathbf{r})\} \right) \\
\mathbf{H}_{\text{sca}} &= \frac{k}{\mu_b \omega} \sum_{n=1}^{\infty} E_n \left(a_n \mathrm{Re}\{\mathbf{M}_{1n}^{(3)}(k,\mathbf{r})\} + i b_n \mathrm{Im}\{\mathbf{N}_{1n}^{(3)}(k,\mathbf{r})\} \right)
\end{aligned} \tag{C.6}$$

and the fields within the spherical dielectric boundary as

$$\begin{aligned}
\mathbf{E}_{\text{int}} &= \sum_{n=1}^{\infty} E_n \left(i d_n \mathrm{Re}\{\mathbf{N}_{1n}^{(3)}(k_1,\mathbf{r})\} + c_n \mathrm{Im}\{\mathbf{N}_{1n}^{(3)}(k_1,\mathbf{r})\} \right) \\
\mathbf{H}_{\text{int}} &= -\frac{k}{\mu_b \omega} \sum_{n=1}^{\infty} E_n \left(d_n \mathrm{Re}\{\mathbf{M}_{1n}^{(3)}(k_1,\mathbf{r})\} + i c_n \mathrm{Im}\{\mathbf{N}_{1n}^{(3)}(k_1,\mathbf{r})\} \right),
\end{aligned} \tag{C.7}$$

where the superscript (3) indicates that the radial part of the generating functions ψ are the spherical Hankel functions $h_n(x)$ of the first kind, and $E_n = i^n E_0(2n+1)/n(n+1)$. Applying the interfacial boundary conditions, we find expressions for the coefficients:

$$a_n(\omega) = \frac{\mu n_1^2 [\rho j_n(\rho)]' j_n(\rho_1) - \mu_1 n^2 [\rho_1 j_n(\rho_1)]' j_n(\rho)}{\mu n_1^2 [\rho h_n(\rho)]' j_n(\rho_1) - \mu_1 n^2 [\rho_1 j_n(\rho_1)]' h_n(\rho)} \tag{C.8}$$

$$b_n(\omega) = \frac{\mu_1 [\rho j_n(\rho)]' j_n(\rho_1) - \mu [\rho_1 j_n(\rho_1)]' j_n(\rho)}{\mu_1 [\rho h_n(\rho)]' j_n(\rho_1) - \mu [\rho_1 j_n(\rho_1)]' h_n(\rho)} \tag{C.9}$$

$$c_n(\omega) = \frac{\mu_1 [\rho h_n(\rho)]' j_n(\rho) - \mu_1 [\rho j_n(\rho)]' h_n(\rho)}{\mu_1 [\rho h_n(\rho)]' j_n(\rho_1) - \mu [\rho_1 j_n(\rho_1)]' h_n(\rho)} \tag{C.10}$$

$$d_n(\omega) = \frac{\mu_1 n_1 n [\rho h_n(\rho)]' j_n(\rho_1) - \mu_1 n_1 n [\rho j_n(\rho)]' h_n(\rho)}{\mu n_1^2 [\rho h_n(\rho)]' j_n(\rho_1) - \mu_1 n^2 [\rho_1 j_n(\rho_1)]' h_n(\rho)}. \tag{C.11}$$

The terms $\rho = kr$, and $\rho_1 = k_1 r$, where $k = \omega/c$, and $k_1 = n_1\omega/c$, and n, n_1 are the indicies of refraction of the background and the target material. Then, from the Poynting vector, the total scattering cross section may be obtained

$$\sigma_{\mathrm{sca}}(\omega) = \frac{2\pi}{k^2} \sum_{n=1}^{\infty} (2n+1) \left(|a_n(\omega)|^2 + |b_n(\omega)|^2 \right) , \tag{C.12}$$

which depend only on the coefficients of the external scattered fields. These coefficients, are often referred to as the 'Mie' scattering coefficients. If the coefficients are expanded in a power series around $kr = 0$ in the small particle limit, for the first non-zero term in the power series we find for coefficient $a_1(\omega) = -i\frac{2}{3}k^3\alpha_{\mathrm{nr}}(\omega)$. Substituted into Eqn. C.12, we see that Eqn. 3.11 is recovered.